

CZECH TECHNICAL UNIVERSITY IN  
PRAGUE

Faculty of Nuclear Sciences and Physical  
Engineering

Department of Physics



# Diploma thesis

**Coherent photoproduction of  $J/\psi$  in Pb–Pb  
collisions with emission of forward neutrons  
with LHC Run 2 data**

**Vendulka Fílová**

**Supervisor: prof. Jesús Guillermo Contreras Nuño, Ph.D.**

**Prague, 2021**

**ČESKÉ VYSOKÉ UČENÍ TECHNICKÉ  
V PRAZE**  
**Fakulta Jaderná a Fyzikálně Inženýrská**  
**Katedra Fyziky**



## **Diplomová práce**

**Koherentní fotoprodukce  $J/\psi$  v Pb–Pb  
srážkách s emisí dopředných neutronů z LHC  
Run 2 dat**

**Vendulka Fílová**

**Vedoucí: prof. Jesús Guillermo Contreras Nuño, Ph.D.**

**Praha, 2021**



**Prohlášení:**

Prohlašuji, že jsem svou diplomovou práci vypracovala samostatně a použila jsem pouze podklady (literaturu, projekty, software, atd.) uvedené v přiloženém seznamu.

Nemám závažný důvod proti užití tohoto školního díla ve smyslu § 60 Zákona č. 121/2000 Sb., o právu autorském, o právech souvisejících s právem autorským a o změně některých zákonů (autorský zákon).

V Praze dne

Vendulka Fílová



## **Acknowledgement**

I would like to express my special appreciation to my supervisor, prof. Jesús Guillermo Contreras Nuño, Ph.D. Without his patience, encouragement, questioning my statements and constant help both with physics and programming this thesis would not have been possible. My thanks also go to Ing. Tomáš Herman who was found time to help and discuss preliminary results and any physics issues since his work took a similar direction as mine.

Special thanks go to my partner Honza and my kids Františka and Alfred for their never-ending love and smiles on their faces when I needed it the most. And finally, I would like to thank my mom for taking these two little angels for a weekend once a while to give me some time to be able to focus and work on this thesis.



*Title:*

**Coherent photoproduction of  $J/\psi$  in Pb–Pb collisions with emission of forward neutrons with LHC Run 2 data**

*Author:* Vendulka Fílová

*Branch of study:* Experimental Nuclear and Particle Physics

*Sort of project:* Diploma thesis

*Supervisor:* prof. Jesús Guillermo Contreras Nuño, Ph.D., Department of Physics,  
Faculty of Nuclear Sciences and Physical Engineering, Czech Technical University in  
Prague

---

*Abstract:*

A photoproduction of  $J/\psi$  mesons may occur in ultra-peripheral Pb–Pb collisions. A cross section of such process is sensitive to gluon distribution function, therefore it gives us a great opportunity to study behavior of gluons inside proton and nucleus in the small Bjorken- $x$  region. The phenomena such gluon saturation and nuclear gluon shadowing can be studied.

In ultra-peripheral collisions, two nuclei collide with the impact parameter larger than the sum of their radii. Nuclei interact via photon-induced processes since hadronic interactions are strongly suppressed. Photoproduction of  $J/\psi$  may occur and also electromagnetic dissociation (EMD) processes with very high probabilities can be observed.

Such processes can be measured with ALICE experiment at the LHC. A measurement of coherent  $J/\psi$  photoproduction cross section with additional EMD is presented in this thesis so it gives us a tool to probe the gluon distribution function down to  $x \sim 10^{-5}$  values.

*Key words:*  $J/\psi$  meson, ultra-peripheral heavy-ion collisions, photoproduction, ALICE detector, **n<sub>0</sub><sup>0</sup>n** generator



*Název práce:*

**Koherentní fotoprodukce  $J/\psi$  v Pb–Pb srážkách s emisí dopředných neutronů z LHC Run 2 dat**

*Autor:* Vendulka Fílová

*Abstrakt:*

V ultra-periferálních srážkách jader olova můžeme pozorovat fotoprodukci mezonu  $J/\psi$ . Účinný průřez takového procesu je citlivý na gluonové distribuční funkce, tím se nám nabízí skvělá možnost, jak studovat chování gluonů uvnitř protonů a jader v regionu malého Bjorkenova  $x$ . Jevy jako gluonová saturace a jaderné gluonové stínění můžou být studovány.

V ultra-periferálních srážkách, jádra interagují s impaktem větším než součet poloměrů jader. Interagují foton-indukovanými procesy a hadronová interakce je vysoce utlumena. Můžeme pozorovat procesy jako  $J/\psi$  fotoprodukce nebo elektromagnetická disociace (EMD).

Takovéto procesy měříme na experimentu ALICE na LHC. V této práci prezentuji výsledký měření účinného průřezu koherentní  $J/\psi$  fotoprodukce následovanou EMD procesem. To je nástrojem, jak zkoumat gluonové distribuční funkce při hodnotách Bjorkenova  $x \sim 10^{-5}$ .

*Klíčová slova:*  $J/\psi$  mezon, ultra- periferální těžko-iontové srážky, fotoprodukce, detektor ALICE,  $n_0^0 n$  generator



# Contents

|          |   |           |
|----------|---|-----------|
| <b>1</b> | <b>Introduction</b>   | <b>1</b>  |
| <b>2</b> | <b>Coherent photoproduction of a <math>J/\psi</math> in ultra-peripheral collisions</b>   | <b>3</b>  |
| 2.1      | Ultra-peripheral collisions . . . . .   | 3         |
| 2.2      | Photoproduction of $J/\psi$ . . . . .   | 3         |
| 2.3      | Electromagnetic dissociation . . . . .  | 6         |
| 2.4      | Cross section of photoproduction of a vector meson . . . . .  | 7         |
| 2.5      | The photon flux . . . . .   | 8         |
| 2.5.1    | Probability of no hadronic interaction . . . . .  | 8         |
| 2.5.2    | Photon flux . . . . .   | 8         |
| 2.5.3    | Nuclear break-up probability . . . . .  | 10        |
| <b>3</b> | <b>ALICE detector</b>   | <b>11</b> |
| 3.1      | The Muon Spectrometer . . . . .   | 11        |
| 3.1.1    | Absorbers . . . . .   | 12        |
| 3.1.2    | The dipole magnet . . . . .   | 13        |
| 3.1.3    | The tracking system . . . . .   | 13        |
| 3.1.4    | Trigger system . . . . .  | 14        |
| 3.2      | The Zero Degree Calorimeters (ZDCs) . . . . .   | 14        |
| 3.3      | The V0 detector . . . . .   | 16        |
| 3.4      | The AD detector . . . . .   | 16        |
| <b>4</b> | <b>A generator of forward neutrons for ultra-peripheral collisions: <math>n_0^0 n</math></b>  | <b>20</b> |
| 4.1      | Probability of neutron emission . . . . .   | 20        |
| 4.1.1    | Probability of the nuclear break-up . . . . .   | 21        |
| 4.2      | Generation of neutron multiplicity . . . . .  | 23        |
| 4.3      | Neutron energy generation . . . . .   | 24        |
| 4.4      | Possible applications and conclusion . . . . .  | 25        |
| <b>5</b> | <b>Measurements of coherent <math>J/\psi</math> production in UPCs</b>  | <b>28</b> |
| 5.1      | Measurements of photoproduction of $J/\psi$ in UPCs with the ALICE and the CMS experiments. . . . .   | 28        |
| 5.1.1    | Coherent $J/\psi$ photoproduction in ultra-peripheral Pb–Pb collisions at $\sqrt{s_{NN}} = 2.76\text{TeV}$ [1] . . . . .                      | 28        |
| 5.1.2    | Coherent $J/\psi$ photoproduction on ultra-peripheral Pb–Pb collisions at $\sqrt{s_{NN}} = 2.76$ with the CMS experiment [2] . . . . .        | 29        |
| 5.2      | Coherent $J/\psi$ photoproduction at forward rapidity in ultra-peripheral Pb–Pb collisions at $\sqrt{s_{NN}} = 5.02\text{ TeV}$ [3] . . . . . | 30        |

|          |  |           |
|----------|--|-----------|
| 5.3      | Summary of results from previous measurements of the coherent $J/\psi$ photoproduction . . . . . | 36        |
| <b>6</b> | <b>Analysis</b>  | <b>40</b> |
| 6.1      | Trigger system, Data acquisition and data processing in ALICE . . . . .                          | 40        |
| 6.1.1    | Trigger system and online data processing . . . . .  | 41        |
| 6.1.2    | Offline computing . . . . .  | 42        |
| 6.2      | Data sample used in the analysis . . . . .   | 42        |
| 6.3      | The triggers . . . . .   | 42        |
| 6.4      | Selection of events . . . . .  | 44        |
| 6.4.1    | Event preselection . . . . .   | 44        |
| 6.4.2    | Track selection . . . . .  | 44        |
| 6.4.3    | Dimuon selection . . . . .   | 44        |
| 6.4.4    | Selection and control plots . . . . .  | 45        |
| 6.5      | ZDC neutron classes . . . . .  | 46        |
| 6.5.1    | Energy deposit in ZNA and ZNC detectors . . . . .  | 48        |
| 6.6      | The invariant mass distribution . . . . .  | 48        |
| 6.6.1    | Feed-down contribution . . . . .   | 50        |
| 6.7      | Transverse momentum distribution . . . . .   | 50        |
| 6.7.1    | Incoherent contribution . . . . .  | 51        |
| <b>7</b> | <b>Corrections</b>   | <b>54</b> |
| 7.1      | Determination of pile-up events . . . . .  | 56        |
| 7.2      | Determination of correction for events lost due to EMD processes . . . . .                       | 57        |
| 7.3      | Procedure of the correction factors calculation . . . . .  | 58        |
| 7.3.1    | Pile-up correction . . . . .   | 58        |
| 7.3.2    | Correction for V0A trigger veto . . . . .  | 59        |
| 7.4      | Results . . . . .  | 60        |
| <b>8</b> | <b>Summary</b>   | <b>65</b> |

# List of Figures

|     |  |    |
|-----|--|----|
| 2.1 | A scheme of single ultra-peripheral collision. Blue pancake-shape Pb nuclei with radii $r_1, r_2$ and charges $Z_1, Z_2$ collide with impact parameter $b$ . The arrows represent electromagnetic field of each Pb nucleus. . . . .  | 4  |
| 2.2 | A Feynman diagram of $J/\psi$ photoproduction with additional EMD causing emission of forward neutron. One incident photon creates the $J/\psi$ vector meson, which decays into dimuon pair in forward rapidities and the target nucleus gains the momentum transfer squared $ t $ . Another photon interact with the same target nucleus and causes the emission of forward neutrons. . . . .               | 5  |
| 2.3 | Different photoabsorption processes in dependence on incident photon energy $E_\gamma$ modeled with RELDIS, taken from [4]. . . . .  | 6  |
| 2.4 | Probability of having no hadronic interaction, according to Eq. 2.9 [5].   | 9  |
| 2.5 | The photon flux according to Eq. 2.10 for a photon energy of $k = 39.94$ GeV, which corresponds for $J/\psi$ production to a rapidity $y = 3.25$ at the LHC energy $\sqrt{s_{NN}} = 5.02$ TeV. The dashed-dot red line corresponds to the point charge form factor and the blue line corresponds to form factor prescription, which accounts for a more realistic description of the Pb nucleus [5]. . . . . | 10 |
| 3.1 | Acceptance of the Muon Spectrometer as a function of $p_T$ for the $J/\psi$ and $\Upsilon(1S)$ in the muon spectrometer rapidity range in their dimuon decay channel with a muon low $p_T$ cut equal to 1 GeV/c [6]. . . . .   | 12 |
| 3.2 | The layout of the Muon Spectrometer [7]. The front absorber filters the background coming from the interaction vertex, the set of tracking chambers are positioned before, inside and after the dipole magnet. After the iron wall, which filters the muons, the trigger system is placed to select heavy quark resonance decays. . . . .  | 13 |
| 3.3 | Layout of the front absorber of the Muon Spectrometer. Different materials which are used for the absorber are presented [7]. . . . .  | 14 |
| 3.4 | The cathode plane layout of Station 1 of the Tracking System of the Muon Spectrometer. Larger pads are used with larger distance from the beam line [7]. . . . .   | 15 |
| 3.5 | Layout of Tracking System Stations 4 and 5 which are located after the dipole magnet of the Muon Spectrometer [7]. . . . .   | 16 |
| 3.6 | A photograph of the Zero Degree Neutron Calorimeter [8]. . . . .   | 17 |
| 3.7 | The energy resolution of Zero Degree Calorimeter measured for hadron and electron beams. It is measured in dependence on $1/\sqrt{E(\text{GeV})}$ [8].   | 18 |
| 3.8 | Schematic drawing of individual segment for V0A (top) and V0C (bottom) detectors with embedded WLS fibres and connected to a PMT [9].  | 19 |

|     |   |    |
|-----|---|----|
| 3.9 | The ALICE Diffractive detector [10]. . . . .  | 19 |
| 4.1 | The cross section $\sigma_{\gamma A \rightarrow A' + X_n}(k)$ for $^{208}\text{Pb}$ . Various experiments and approaches are used to describe different energy ranges. Figure taken from [11]. . . . .  | 21 |
| 4.2 | Mean number of excitations $P_{X_n}^l(b)$ for case of Pb. Figure taken from [11]. . . . .   | 22 |
| 4.3 | Partial cross section for $^{208}\text{Pb}$ and various neutron multiplicities as measured by the experiments quoted on the figure. Figure taken from [11]. . . . .   | 23 |
| 4.4 | Arithmetic average (line) and dispersion (dashed area) of neutron multiplicity as a function of the incident photon energy. The approach used here and the prediction of the RELDIS model [12] are shown in red and with a dash line, respectively. Figure taken from [11]. . . . .   | 24 |
| 4.5 | Branching ratio of the total cross section to different neutron multiplicities as a function of the incident photon energy up to $10^9$ MeV. On the left vertical axes the number of neutrons is shown and the right vertical axes displays its probability estimated by a Gaussian approximation. Figure taken from [11]. . . . .          | 24 |
| 4.6 | Emission spectra of secondary neutrons from photo-neutron reactions on $^{208}\text{Pb}$ from evaluated nuclear data taken from ENDF database for full energy range up to 140 MeV. Figure taken from [11]. . . . .  | 25 |
| 4.7 | The probability of emission of nenutron(s) for coherently produced $\rho^0$ events, generated with the STARlight at mid-rapidity $ y  < 1.0$ . The blue, red and green lines represent events with zero, one and two neutrons in one side and one or more neutrons produced in the other side. Figure taken from [11]. . . . .              | 26 |
| 4.8 | A cross section in rapidity dependence for $J/\psi$ photoproduction predicted with the hot-spot model for different neutron classes generated with the $n_0^0 n$ . Figure taken from [11]. . . . .  | 27 |
| 5.1 | The differential cross section of coherently produced $J/\psi$ at rapidity interval $-3.6 < y < -2.6$ which is shown by the vertical bar of the measurement point. The error is quadratic sum of the statistical and systematic errors. With the colored curves different theoretical predictions are shown. Figure taken from [1]. . . . . | 29 |
| 5.2 | Differential cross section in dependence on rapidity for coherently photoproduced $J/\psi$ measured by CMS and ALICE. The horizontal bars represent the rapidity range of the measurements and the vertical error bars include statistical and systematic uncertainties. Figure taken from [2]. . . . .                                     | 31 |
| 5.3 | Invariant mass distribution for muon pairs. The pink and red lines correspond to Crystall Ball functions representing $J/\psi$ and $\psi'$ signals. The dashed green line corresponds to the background and the solid blue line corresponds to the sum of background and signal functions [3]. . . . .                                      | 32 |
| 5.4 | Transverse momentum distribution for muon pairs in range $2.85 < m_{\mu\mu} < 3.35 \text{ GeV}/c^2$ . Figure taken from [3]. . . . .  | 34 |
| 5.5 | The $p_T$ distributions for different rapidity intervals for dimuons in the range $2.85 < m_{\mu\mu} < 3.35 \text{ GeV}/c^2$ [3]. . . . .   | 38 |

|      |   |    |
|------|---|----|
| 5.6  | Measured coherent differential cross section of photoproduced $J/\psi$ in ultra-peripheral collisions at $\sqrt{s_{NN}} = 5.02$ TeV. The statistical uncertainties are represented by the error bars and the boxes around the points are the systematic errors. The colored lines represent different theoretical calculations and the green band represents the uncertainties of the EPS09 LO model [3]. . . . . | 39 |
| 6.1  | The six layers of online processing of the High Level Trigger (HLT) [13].   | 41 |
| 6.2  | Real data processing and Monte Carlo simulation [13]. . . . .   | 43 |
| 6.3  | The number of tracklets after all cuts applied. . . . .   | 45 |
| 6.4  | Momentum of $\mu_+$ and $\mu_-$ tracks after all cuts applied. . . . .  | 46 |
| 6.5  | Azimuth angle distribution of $\mu_+$ and $\mu_-$ tracks after all tracks applied. . . . .  | 47 |
| 6.6  | ZNA (red line) and ZNC (blue line) time distributions of events after all cuts applied in two different ranges. The left one ranges $-250 < t < 250$ ns to see the other bunch crossings and the right shows the focused time on $-2.0 < t < 2.0$ ns. . . . .   | 48 |
| 6.7  | ZNA energy deposit distribution of selected events. The first two peaks are fitted by the Gaussian function. The extracted mean values are in good agreement with our expectations. . . . .   | 49 |
| 6.8  | ZNC energy deposit distribution of selected events. The first two peaks are fitted by the Gaussian function. The extracted mean values are in good agreement with our expectations. . . . .   | 49 |
| 6.9  | Invariant mass distribution of dimuon pairs in the full rapidity range $-4 < y_{2.5}$ satisfying all cuts described above. The green line represents the background. The red and blue line corresponds to Crystal Ball functions representing $J/\psi$ and $\Psi'$ signals, respectively. . . . .   | 50 |
| 6.10 | Invariant mass distributions fitted with the Crystal Ball function for selected $J/\psi$ events with $p_T < 0.25$ GeV/ $c$ in different ZDC classes. . .  | 51 |
| 6.11 | Transverse momentum distribution of events satisfying all cuts described above and fitted with a model consisting of a sum of the templates based on MC data set described in the text. Each process contributing to the final model is also shown in the figure. . . . .   | 52 |
| 6.12 | Transverse momentum distributions in different ZDC classes fitted with a model consisting of a sum of the templates based on MC data set described in the text. . . . .   | 53 |
| 7.1  | Coherent data sample in ZDC class (Xn0n), blue shows signal in ZNA, green shows signal in the offline V0ADecision and gray ellipse represents vents lost due to V0A veto. . . . .   | 55 |
| 7.2  | Pile-up determination using the CTRUE events for V0A detector. . . .  | 62 |
| 7.3  | EMD events lost due to the V0A veto for (Xn0n) neutron class. . . .   | 63 |
| 7.4  | EMD events lost due to the V0A veto for (XnXn) neutron class. . . .   | 64 |

# Chapter 1

## Introduction

Behavior of gluons bounded inside a nucleus is an interesting topic to be studied. For small values of  $x$  ( $x \lesssim 10^{-2}$ ), gluons are the dominant component of the nucleons [14] and this dominance increases as a power law for decreasing  $x$ . The raise cannot continue infinitely. At some point, when the gluon density is large enough, the radiation of softer and softer gluons is balanced by recombination processes and eventually, the system is saturated [15]. The saturation is characterized by a transverse momentum  $Q_s$ , which is referred as saturation momentum. Typical values for large nuclei are  $Q_s^2 \approx 5 \text{ GeV}^2$  at the LHC.

Well suited experimental observable to study gluon behavior is coherent  $J/\psi$  photoproduction. It is so, because the cross section of such process is proportional to the square of the gluon distribution function [16]. More about theory of parton distribution functions is written in my previous work [17].

Photonuclear interactions can be studied in ultra-peripheral collisions (UPCs) of heavy ions at the LHC. One particular photonuclear interaction which is interesting is the coherent photoproduction of  $J/\psi$  vector meson. The photoproduction of  $J/\psi$  can be accompanied by an additional independent electromagnetic dissociation (EMD). In electromagnetic dissociation, one or both interacting nuclei can emit neutron(s) and charged particle(s) in forward rapidities. The cross section of EMD processes depend on the incident photon energy. We believe that measuring of such events might give us a tool to probe gluon distribution at values of  $x$  scaling down to  $\sim 10^{-5}$ .

In this thesis, the coherent  $J/\psi$  photoproduction in Pb–Pb UPCs measured with ALICE at  $\sqrt{s_{NN}} = 5.02 \text{ TeV}$  is studied. The most recent published paper measuring the cross section of  $J/\psi$  can be found here [3]. However, in the cited paper, the additional electromagnetic dissociation processes has not been studied in the analysis. Even worse, as at the time of data taking (2018) it was still not recognized that important corrections may be needed, there were no control triggers available to determine the correction factors. Determination of the probability of EMD with emission of charged particles accompanying the  $J/\psi$  photoproduction in different neutron classes and determination of the correction factors is the main contribution of this thesis.

The thesis is organized as follows. In the next chapter I briefly describe ultra-peripheral collisions and the process of photoproduction. The Chapter ?? I devote to a description of ALICE detector, particularly to the detectors that are important in this analysis. One of the relevant advances in this area is the new NOON generator that allows us, for the first time, to simulate the production of neutrons at forward

rapidities. This program is not used in the present thesis, but it is an important tool for the next steps toward a cross section. In order to have the most up to date information, Chapter 4 is devoted to the description of the paper introducing NOON. In Chapter 5 I describe the most recent published [3]  $J/\psi$  analysis measured by ALICE and I present the results. Chapter 6 and Chapter 7 are devoted to the data selection and the procedure of determination of corrections due to electromagnetic dissociation processes. The summary and the outlook is in the Chapter 8.

## Chapter 2

# Coherent photoproduction of a $J/\psi$ in ultra-peripheral collisions

In this chapter I briefly describe the ultra-peripheral collisions (UPC) of two interacting lead nuclei. The hadronic interaction is suppressed in UPCs and photon-induced processes take place. Two types of photonuclear interactions, photoproduction of a vector meson and electromagnetic dissociation, are described in sections 2.2 and 2.3. In section 2.4 I present the cross section of coherent  $J/\psi$  photoproduction with additional independent forward neutron emission.

I also mention some ALICE detectors below, such The Muon Spetrometer, The Zero Degree Calorimeter, AD and V0. All these detectors are described in Chapter ??.

### 2.1 Ultra-peripheral collisions

Two nuclei passing along each other, having an impact parameter larger than the sum of their radii, are called ultra-peripheral collisions. Both charged nuclei are surrounded by their electromagnetic field, which can be treated, for fast particles, as a flux of virtual photons [18], and the nuclei can interact via this electromagnetic field. The number of photons scales as the square of the nuclear charge ( $Z^2$ ) and the photon energy scales with the Lorentz contraction of the nuclei [19]. A schematic view of such collision is shown in Fig. 2.1. One of these photons can interact with the passing Pb nucleus and, for instance, create a  $J/\psi$  vector meson or excite the target nucleus which subsequently emits neutrons. At the LHC, photon-induced processes have very large cross sections in Pb–Pb UPCs.

### 2.2 Photoproduction of $J/\psi$

One type of photonuclear interaction is a vector meson photoproduction [19]. This process has a large cross section, which can be understood from several photoproduction models such as the LO pQCD calculation, vector meson dominance or color dipole model [19].

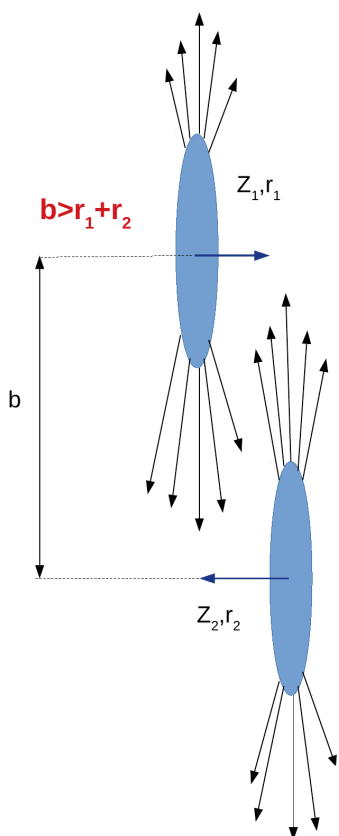


Figure 2.1: A scheme of single ultra-peripheral collision. Blue pancake-shape Pb nuclei with radii  $r_1, r_2$  and charges  $Z_1, Z_2$  collide with impact parameter  $b$ . The arrows represent electromagnetic field of each Pb nucleus.

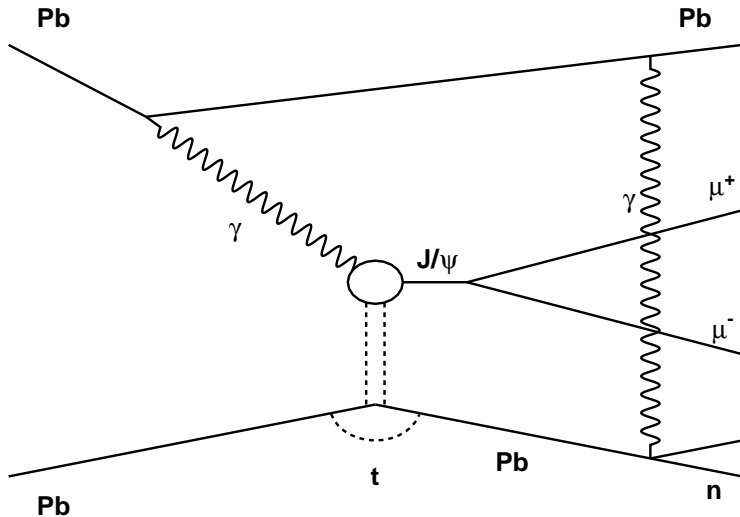


Figure 2.2: A Feynman diagram of  $J/\psi$  photoproduction with additional EMD causing emission of forward neutron. One incident photon creates the  $J/\psi$  vector meson, which decays into dimuon pair in forward rapidities and the target nucleus gains the momentum transfer squared  $|t|$ . Another photon interact with the same target nucleus and causes the emission of forward neutrons.

Vector meson photoproduction in Pb–Pb collisions can occur in different forms. We talk about coherent production, when the photon interacts coherently with the whole nucleus which stays intact after the collision. The coherence condition sets the limit on the transverse momentum of the produced vector meson to be very low  $p_T \sim 60 \text{ MeV}/c$ . In such collision only the vector meson is produced in the final state and nothing else, denoted as exclusive or coherent vector meson photoproduction.

There is also a type of interaction, where the photon does not interact with the whole nucleus, but only with a single nucleon bounded inside the nucleus. In such collision, the target nucleus breaks up and because the radius of the nucleon is smaller than the radius of a nuclei, the transverse momentum of the produced particle is larger,  $p_T \sim 300 \text{ MeV}/c$ . We talk about incoherent production.

Coherent photoproduction of  $J/\psi$  is the process I am interested in, a Feynman diagram of such process is shown in Fig. 2.2. One of the nucleus emits a photon that fluctuates into a quark-antiquark pair (in the color dipole interpretation) or into a  $J/\psi$  vector meson (in the vector-dominance model) which interacts with the nucleus circulating in the opposite direction. As a product of the interaction a  $J/\psi$  is produced and the interacting Pb nucleus receives a momentum transfer squared  $|t|$ . The  $J/\psi$  then decays into a muon-antimuon pair which is detected in the Muon Spectrometer (Chapter 3). In Fig. 2.2, the first photon from the left refers to the incident photon creating the  $J/\psi$ . The second photon corresponds to an independent photonuclear reaction, which leads to emission of neutrons in forward rapidities. These forward neutrons are measured in the Zero Degree Calorimeter. The second process is described in the next section.

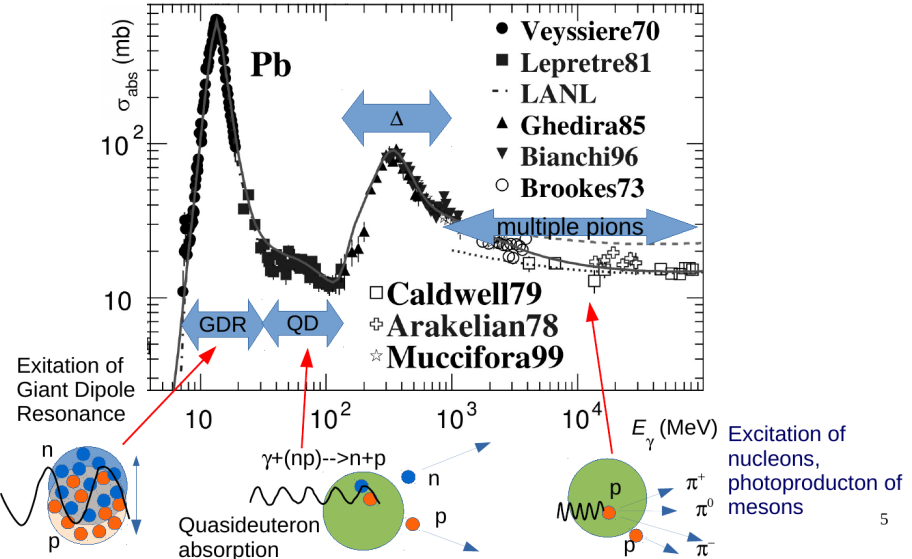


Figure 2.3: Different photoabsorption processes in dependence on incident photon energy  $E_\gamma$  modeled with RELDIS, taken from [4].

### 2.3 Electromagnetic dissociation

The cross section of electromagnetic dissociation of  $^{208}\text{Pb}$  in UPC at the LHC is very large  $\sim 200$  b. The Weizsäcker–Williams method takes the Coulomb field of an accelerated nucleus to be equivalent to a photon flux with the specific spectrum and different processes can occur while a nucleus absorbs a photon with the specific energy. The cross sections of such processes are shown in Fig. 2.3 and described below. The Relativistic Electromagnetic Dissociation (RELDIS) model was developed to describe fragmentation of ultrarelativistic nuclei under the impact of intense electromagnetic fields [12] and is used in the figure to fit the data.

At the photon energy  $E_\gamma \leq 40$  MeV, the wavelength is comparable to the size of a nucleus [12]. In that case, the excitation in the form of Giant Dipole Resonance (GDR) is the most probable process within this energy range. The full photon energy is absorbed by the nucleus and transformed into the excitation energy of nucleus  $E^*$ . The deexcitation proceeds mainly through neutron evaporation, since the neutron separation energy is about 7 MeV. An emission of protons is suppressed in the GDR because of high Coulomb barrier in heavy nuclei.

Within the energy interval of  $40 \leq E_\gamma \leq 140$  MeV the wavelength is similar to the distance between nucleons inside a nucleus, therefore photon absorption by proton-neutron pairs occur. This quasi-deuteron mechanism of photoabsorption becomes important and dominates up to the pion production threshold  $E_\gamma = 140$  MeV. Within this energy interval, only a fraction of the photon energy transforms into the excitation of the residual nucleus  $E^*$ . The rest of the energy is carried away by the fast nucleons that represent the quasi-deuteron pair which absorbed the photon. The two-nucleon mechanism of a photoabsorption reaches up to  $E_\gamma \sim 500$  MeV overlapping hadron production on an individual nucleon.

When the energy of a photon exceeds the pion photoproduction threshold,  $E_\gamma >$

140 MeV, the wavelength becomes less than a nucleon radius and photoproduction on individual constituent nucleons is observed. Above the threshold, excitation of  $\Delta$ -resonances dominates and the cross section of secondary interaction of produced slow pion with the constituent nucleons is small. Due to a high probability of leaving the nucleus without an interaction, such pions carry away a sizable fraction of the photon energy. The multiple pion photoproduction starts to dominate at a photon energy above several GeV.

The energies mentioned in this paragraph refer to the rest system of the nucleus. The produced pions are boosted in the LHC frame to forward rapidities and may impact some of the forward detectors used to veto hadronic collisions, such as V0 or AD. These vetoed events are lost and the cross section should be corrected to account for them. This is the main goal of this thesis and the results are presented in Chapter 7.

In a single EMD event, there is a  $\sim 97\%$  probability that at least one neutron will be produced in either side [20]. Therefore, electromagnetic dissociation events can be defined by the detection of the prompt neutrons in the Zero Degree Calorimeter and events can be classified into different neutron classes in dependence on type (single, mutual) emission and on the side (A,C) of the produced neutrons.

## 2.4 Cross section of photoproduction of a vector meson

The cross section of the  $J/\psi$  photoproduction with the independent EMD can be measured in different neutron classes. Neutron classes are defined by the production of neutrons due to electromagnetic excitation and subsequent deexcitation.

The differential cross section for the coherent photoproduction of a  $J/\psi$  at rapidity  $y$  is given by the product of the photon flux  $N_{\gamma/\text{Pb}}(y)$  and the photon-Pb cross section  $\sigma_{\gamma/\text{Pb}}$ . In the particular collision either the first nucleus serves as a photon emitter and the second nucleus as the target or the other way around. Therefore the process is the sum of two contributions [21][22].

$$\frac{d\sigma_{\text{PbPb} \rightarrow J/\psi \text{PbPb}}(y)}{dy} = N_{\gamma/\text{Pb}}(y)\sigma_{\gamma \text{Pb} \rightarrow J/\psi \text{Pb}}(y) + N_{\gamma/\text{Pb}}(-y)\sigma_{\gamma \text{Pb} \rightarrow J/\psi \text{Pb}}(-y), \quad (2.1)$$

and the rapidity  $y$  is given by

$$y = \ln\left(\frac{2k}{M_{J/\psi}}\right), \quad (2.2)$$

where  $k$  is the energy of interacting quasi real photon, therefore, one contribution describes an interaction involving a low-energy photon ( $k_L$ ) and the second a high-energy photon ( $k_H$ ). In case of the additional electromagnetic excitation it is assumed that the coherence of the photoproduction is not destroyed but the impact parameter is influenced and the photon flux of the photons is given by:

$$N_{\gamma/\text{Pb}}^{(ij)}(k) = \int d^2\vec{b} P_{ij}(\vec{b}) P_{NH}(\vec{b}) n_{\gamma/\text{Pb}}(k, \vec{b}), \quad (2.3)$$

where  $P_{NH}(\vec{b})$  is the probability of having no hadronic interaction between the incoming lead nuclei,  $n_{\gamma/\text{Pb}}(k, \vec{b})$  is the photon flux and  $P_{ij}(\vec{b})$  is the probability of having the electromagnetic excitation taking into account different classes of the nuclear decay by the neutron emission, such  $(i,j)=(0n0n), (Xn0n), (0nXn)$  and  $(XnXn)$ . The meaning of the denoted neutron classes is the following. In  $(0n0n)$  class no neutrons were produced

in either side, ( $XnXn$ ) neutrons were produced in both sides and ( $0nXn$ ) and ( $Xn0n$ ) at least one neutron was produced in C-side or A-side, respectively.

Measuring the cross section of  $J/\psi$  photoproduction in any two neutron classes, for example ( $0nXn$ ) and ( $XnXn$ ), one obtains:

$$\frac{d\sigma_{PbPb \rightarrow J/\psi PbPb}^{(0nXn)}(y)}{dy} = N_{\gamma/Pb}^{(0nXn)}(k_L)\sigma_{\gamma Pb \rightarrow J/\psi Pb}(k_L) + N_{\gamma/Pb}^{(0nXn)}(k_H)\sigma_{\gamma Pb \rightarrow J/\psi Pb}(k_H), \quad (2.4)$$

$$\frac{d\sigma_{PbPb \rightarrow J/\psi PbPb}^{(XnXn)}(y)}{dy} = N_{\gamma/Pb}^{(XnXn)}(k_L)\sigma_{\gamma Pb \rightarrow J/\psi Pb}(k_L) + N_{\gamma/Pb}^{(XnXn)}(k_H)\sigma_{\gamma Pb \rightarrow J/\psi Pb}(k_H). \quad (2.5)$$

We are interested in  $\sigma_{\gamma Pb \rightarrow J/\psi Pb}(k)$ . To solve these equations we need to know the photon flux. It can be calculated for each neutron class and it is described in the section below.

## 2.5 The photon flux

### 2.5.1 Probability of no hadronic interaction

In UPC with photon-induced processes it is required to avoid a hadronic interaction between colliding Pb–Pb nuclei. The probability is computed starting with the nuclear density distribution  $\rho(s)$  of the Pb nucleus at a distance  $s$  from its center. It can be modeled, for example, with a Wood-Saxon distribution:

$$\rho_{Pb}(s) = \frac{\rho_0}{1 + \exp(\frac{s - R_{WS}}{d})}, \quad (2.6)$$

with  $R_{WS}$  and  $d$  are appropriate parameters. Then the nuclear function is defined by

$$T_A(\vec{b}) = \int dz \rho(\sqrt{|\vec{b}|^2 + z^2}), \quad (2.7)$$

where  $z$  is the incoming nucleus direction and  $A$  is the type of a nucleus. After that, the nuclear overlap function is given as

$$T_{AA}(b) = \int d^2\vec{r} T_A(\vec{r}) T_A(\vec{r} - \vec{b}). \quad (2.8)$$

Finally, the probability of having no hadronic interaction at an impact parameter  $b$  can be obtained from

$$P_{NH}(b) = \exp(-T_{AA}\sigma_{NN}), \quad (2.9)$$

where  $\sigma_{NN}$  is the nucleon-nucleon inelastic cross section. The probability of no hadronic interaction is shown in Fig. 2.4, according to Eq. 2.9 and a nucleus distribution described by the Wood-Saxon formula (Eq. 2.6). It can be seen that the probability of having a no hadronic interaction is basically zero when the impact parameter  $b$  is less than 14 fm and one for  $b$  greater than 19 fm.

### 2.5.2 Photon flux

The quasi-real photon is emitted with an energy  $k$  at a distance  $b$  from the center of the charged particle, in our case Pb nucleus. The flux of these photons, in the semi-classical

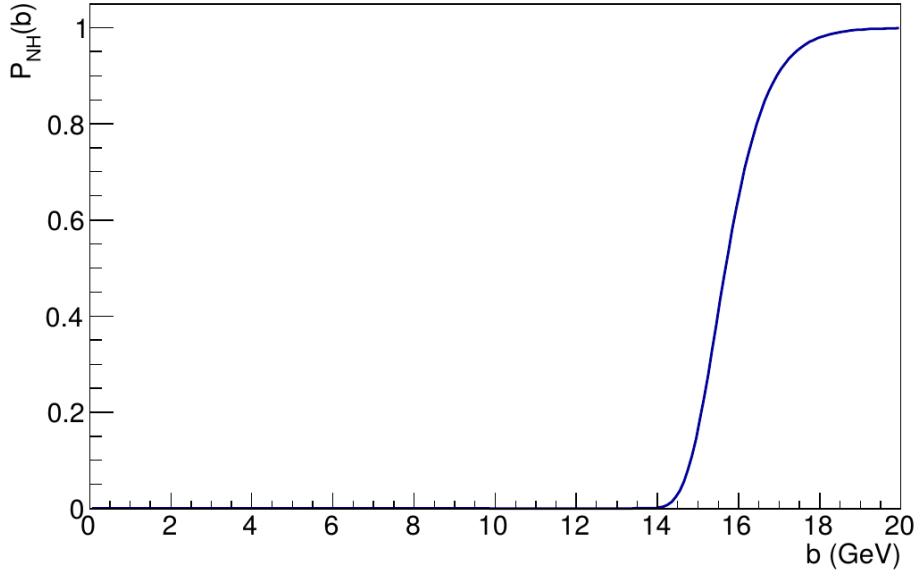


Figure 2.4: Probability of having no hadronic interaction, according to Eq. 2.9 [5].

description [19], is given by:

$$n(k, \vec{b}) = \frac{Z^2 \alpha}{\pi^2 k} \left| \int_0^\infty dk_\perp k_\perp^2 \frac{F(k_\perp^2 + (k/\gamma)^2)}{k_\perp^2 + (k/\gamma)^2} J_1(bk_\perp) \right|^2, \quad (2.10)$$

where  $Z$  is the electric charge,  $\alpha$  is the QED fine structure constant,  $J_1$  a Bessel function and  $F$  is the form factor of the charged particle. The coherent  $J/\psi$  photoproduction in Pb–Pb can be described by several prescriptions of the form factor. The easiest prescription for the form factor is that the charged particle is considered to be a point charge,  $F_{pc}(q) = 1$ . Then after the integration of Eq. 2.10 one gets:

$$n(k, \vec{b}) = \frac{\alpha Z^2}{\pi^2 b^2} x^2 [K_1^2(x) + \frac{1}{\gamma} K_0^2(x)], \quad (2.11)$$

where  $k$  is the energy of the photon,  $\gamma$  is the Lorentz factor,  $Z$  is the electric charge of the emitting Pb nucleus and  $K_0$  and  $K_1$  are Bessel functions,  $x = kb/\gamma$ . The photon flux with two different prescriptions for the form factor is presented in Fig. 2.5 computed from Eq. 2.10 for a photon energy of  $k = 39.94$  GeV. One case is for the point charge and the second form factor considers a more realistic description of a Pb nucleus which starts with the Wood-Saxon nuclear description mentioned earlier. One can see that for an impact parameter larger than 8 fm, the photon fluxes are similar for both cases of the form factors.

For the case  $b > b_{\min} = R_1 + R_2$ , after an integration over  $\vec{b}$ , the photon flux is obtained from:

$$n(k) = \frac{2\alpha Z^2}{\pi} [\xi K_0(\xi) K_1(\xi) - \frac{\xi^2}{2} (K_1^2(\xi) - K_0^2(\xi))], \quad (2.12)$$

where  $\xi = kb_{\min}/\gamma$ .

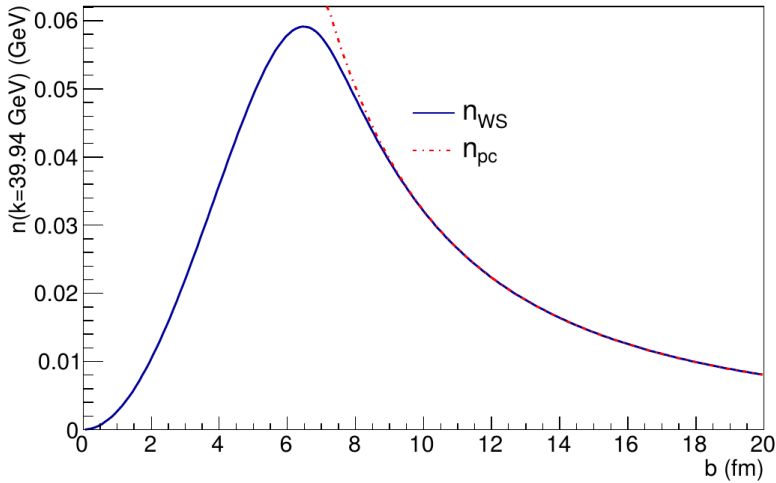


Figure 2.5: The photon flux according to Eq. 2.10 for a photon energy of  $k = 39.94$  GeV, which corresponds for  $J/\psi$  production to a rapidity  $y = 3.25$  at the LHC energy  $\sqrt{s_{NN}} = 5.02$  TeV. The dashed-dot red line corresponds to the point charge form factor and the blue line corresponds to form factor prescription, which accounts for a more realistic description of the Pb nucleus [5].

The photon flux expressed in a relevant variable of rapidity  $y$  instead of photon energy  $k$  is given as:

$$N_{\gamma/\text{Pb}}(y) = k \frac{dn(k)}{dk} |_{\text{Pb}}. \quad (2.13)$$

Taking into account the Wood-Saxon description of the nucleus and the probability of having no hadronic interaction described above, the photon flux is calculated as a convolution of  $P_{NH}$  given by the equation 2.9 and the photon flux  $n(k, \vec{b})$  from the equation 2.10:

$$N(y) = k \int_0^\infty db 2\pi b P_{NH}(b) \int_0^{r_A} \frac{r dr}{\pi r_A^2} \int_0^{2\pi} d\phi n(k, b + r \cos(\phi)). \quad (2.14)$$

### 2.5.3 Nuclear break-up probability

The determination of the probability of nuclear break-up  $P_{ij}$  which is totally independent is described in depth in the published paper [11], which I present in the Chapter 4. The photon flux is obtained as a convolution of the probability of nuclear break-up  $P_{ij}$  and the equation 2.10.

## Chapter 3

# ALICE detector

The ALICE detector is a very complex device with several sub-detectors. According to studied process described in Chapter 2, this chapter is devoted to description of detectors needed to measure the forward  $J/\psi$  vector meson decaying into dimuon pair with neutron emission in forward rapidities. Description of another ALICE subdetectors can be found in my previous work [17, 23].

The muon pair, that is produced from  $J/\psi$  decay, in forward direction are detected in the Muon Spectrometer. The Zero Degree Calorimeter is used to measure neutrons produced in electromagnetic dissociation in forward rapidities. Sub-detectors AD and V0 are detectors sensitive to a charged particle activity and in the measurement of coherent  $J/\psi$  are used to ensure the exclusivity of the event. All these detectors are described in following sections.

### 3.1 The Muon Spectrometer

The main function of the Muon Spectrometer is to measure open flavor and quarkonia production, such as the  $J/\psi$ , via their decay into muons. For nucleus-nucleus collisions the centrality dependence with the reaction plane can be studied. The Muon Spectrometer covers the rapidity range of  $-4.0 < y < -2.5$ . The acceptance for  $J/\psi$  meson is presented in Fig. 3.1 for this rapidity range. It is displayed as a function of the transverse momentum for the  $J/\psi$  and  $\Upsilon(1S)$  up to  $p_T = 30 \text{ GeV}/c$ . The transverse momentum of the coherent  $J/\psi$  is very low  $p_T < 0.25 \text{ GeV}/c$ , therefore the region we are interested in is  $p_T \sim 0 \text{ GeV}/c$  with the acceptance corresponding to the value of  $\sim 0.35$ .

Two experimental requirements for the muon detector are to measure quarkonia production at very low  $p_T$  and to have an invariant mass resolution of the muon spectrometer about  $70 \text{ MeV}/c^2$  in the  $J/\psi$  region and  $100 \text{ MeV}/c^2$  to distinguish different resonances of the  $\Upsilon$  family. To reach these two requirements, the muon spectrometer is located on the C-side of the ALICE experiment and it covers the angular range  $171^\circ < \theta < 178^\circ$ . The layout of the detector is presented in Fig. 3.2 [6]. The detector covers 19 m of the beam pipe length, which passes through the device. It consists of the front absorber to filter the background, placed the closest to the vertex. A set of tracking chambers is located in front, inside and after the muon dipole magnet, which bends muon tracks by providing a magnetic field. To stop electrons and eventual hadrons, a thick iron wall is placed behind the tracking stations and before the trigger chambers.

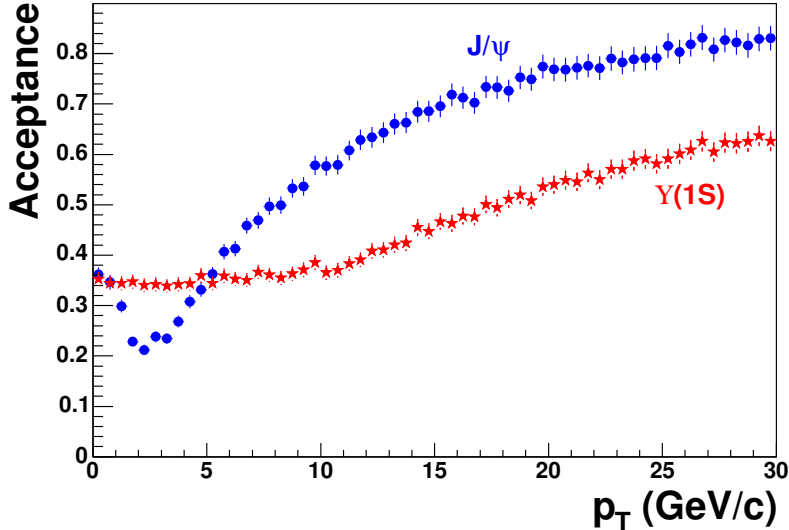


Figure 3.1: Acceptance of the Muon Spectrometer as a function of  $p_T$  for the  $J/\psi$  and  $Y(1S)$  in the muon spectrometer rapidity range in their dimuon decay channel with a muon low  $p_T$  cut equal to  $1 \text{ GeV}/c$  [6].

The trigger system selects heavy quark resonance decays. The selection is made on the  $p_T$  of the two individual muons. In the following text, the individual parts of the muon spectrometer are described [7] in more detail.

### 3.1.1 Absorbers

The muon spectrometer consists of two absorbers - the front absorber with the beam shielding and the iron wall. Absorbers reduce the forward flux of charged particles by at least two orders of magnitude. The front absorber is positioned as close to the interaction point as possible so the physics performance of the ALICE central barrel is not disrupted. It suppresses charged hadrons and decreases the muon background from decays of kaons and pions. It is achieved by minimizing the distance between the interaction point and the absorber to 90 cm. To provide a good shielding and limited multiple scattering low- $Z$  material is used in the layers closer to the interaction point and materials with higher  $Z$  are used to shield further in the movement direction. In Fig. 3.3 the layout of the front absorber with the different materials used is shown. The front absorber is the main contributor to the invariant mass resolution of the spectrometer.

The spectrometer is shielded throughout its length by the inner beam shield with a diameter of about 60 cm. It is crucial to reduce the low energy background in the tracking and trigger chambers from the primary and secondary particles produced at very forward rapidities and from their showers produced in the beam pipe and in the shield itself. It is made of tungsten, lead and stainless steel.

Finally, the iron wall is placed between the tracking chambers and the trigger chambers. It is 120 cm thick and it reduces the low energy background particles and stops hadrons which were not filtered out in the front absorber.

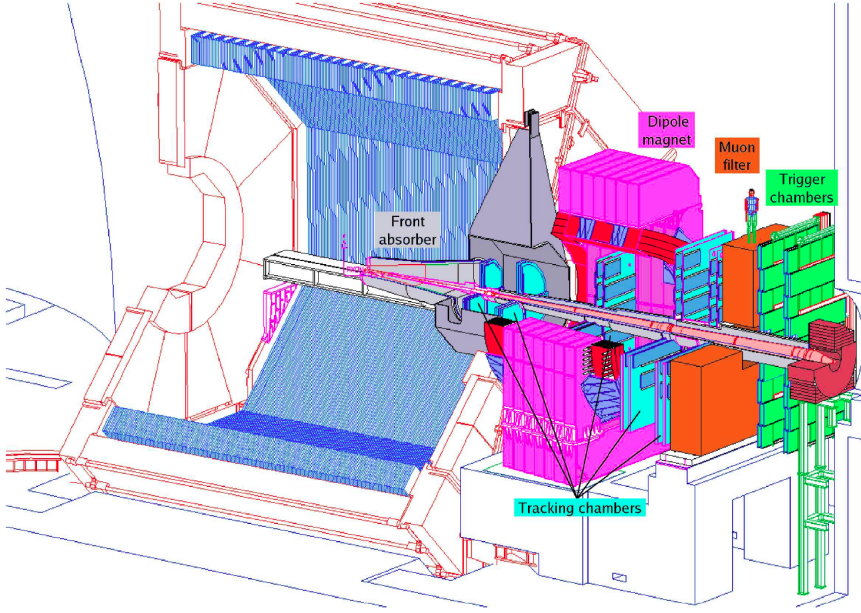


Figure 3.2: The layout of the Muon Spectrometer [7]. The front absorber filters the background coming from the interaction vertex, the set of tracking chambers are positioned before, inside and after the dipole magnet. After the iron wall, which filters the muons, the trigger system is placed to select heavy quark resonance decays.

### 3.1.2 The dipole magnet

The muon spectrometer dipole magnet provides a maximum central field of 0.7 T and an integral field of 3 T. The coils are cooled with water to a temperature about 15 to 25 °C and its overall dimensions are 5 m in length, 7.1 m width and 9 m height. The dipole has the same angular acceptance of the detector and provides a horizontal magnetic field perpendicular to the beam axis. The polarity of the field can be reverted in a very short time.

### 3.1.3 The tracking system

The tracking system has two requirements to fulfill. The first requirement is to achieve spatial resolution of 100  $\mu\text{m}$ . This resolution is necessary to reach the wanted resolution in invariant mass of 100  $\text{MeV}/c^2$ . The second requirement is to operate in a maximum hit density of about  $5 \times 10^{-2} \text{ cm}^{-2}$  expected in Pb–Pb collisions. These constraints are fulfilled by the use of Multi-Wire Proportional Chambers (MWPCs) with cathode pad readout.

The tracking system is segmented into five detector stations; two are placed in front of the dipole magnet, one is inside and the last two are behind the magnet, as can be seen in Fig. 3.2. Each station is made of two chamber planes, with two cathode planes each, therefore two-dimensional information is provided. Since the hit density decreases with the distance from the beam pipe, larger pads are used at larger radii, as can be seen in Fig. 3.4. To minimize the multiple scattering carbon fibres are used as a material and the thickness of the chamber corresponds to 0.03 of radiation length. In

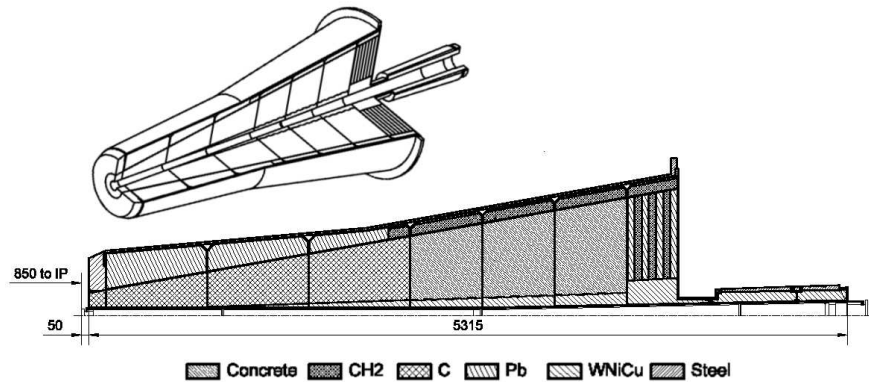


Figure 3.3: Layout of the front absorber of the Muon Spectrometer. Different materials which are used for the absorber are presented [7].

Fig. 3.5 a photo of tracking stations 4 and 5 is shown.

### 3.1.4 Trigger system

Behind the iron filter, the trigger system of the Muon Spectrometer is placed. The system consists of two trigger stations (MT1 and MT2) located 16 m from the interaction point and 1 m apart from each other. Each station is composed of two planes of 18 Resistive Plate Chambers (RPCs). The RPCs are detectors which are made of high resistivity bakelite electrodes separated by 2 mm wide gas gap. From the signal from RPCs the transverse momentum of each muon is provided. The spatial resolution is better than 1 cm and the time resolution is 2 ns to identify the bunch crossing.

The output of the trigger electronics has two different thresholds, the low and high- $p_T$  cuts. It is optimized for the detection of two different resonance families. Cut values of  $p_T \cong 1(2)$  GeV/c are selected for the J/ $\psi$  ( $\Upsilon$ ) detection.

## 3.2 The Zero Degree Calorimeters (ZDCs)

The Zero Degree Calorimeters (ZDCs) measure the energy of non-interacting nucleons (spectators) from the collision [8]. It is used to measure the multiplicity and then also the centrality of the collision. Therefore it can be used for triggering events with different centralities. In our case it is used to detect emitted neutrons. Since the neutron energy is approximately the same as the beam neutron, the ZDC can be used as a multiplicity detector. The ZDCs consist of two identical sets located at opposite sides of the interaction point. Each set of detectors consists of a neutron (ZN) and proton (ZP) Zero Degree Calorimeter. Since for our purpose measuring neutrons is important, only the ZN will be discussed.

The ZDCs are quartz-fibre spaghetti calorimeters with silica optical fibres as the active material which is embedded in a dense passive material, as an absorber. They are located on both sides at 112.5 meters from the interaction point. The ZN is placed at zero degrees with respect to the beam axis. The principle of the operation is based on the detection of Cherenkov light produced by a charged particle in the quartz fibre. A shower of charged particles is produced by the neutron crossing the passive material. The response is very fast due to the intrinsic speed of the emission process.

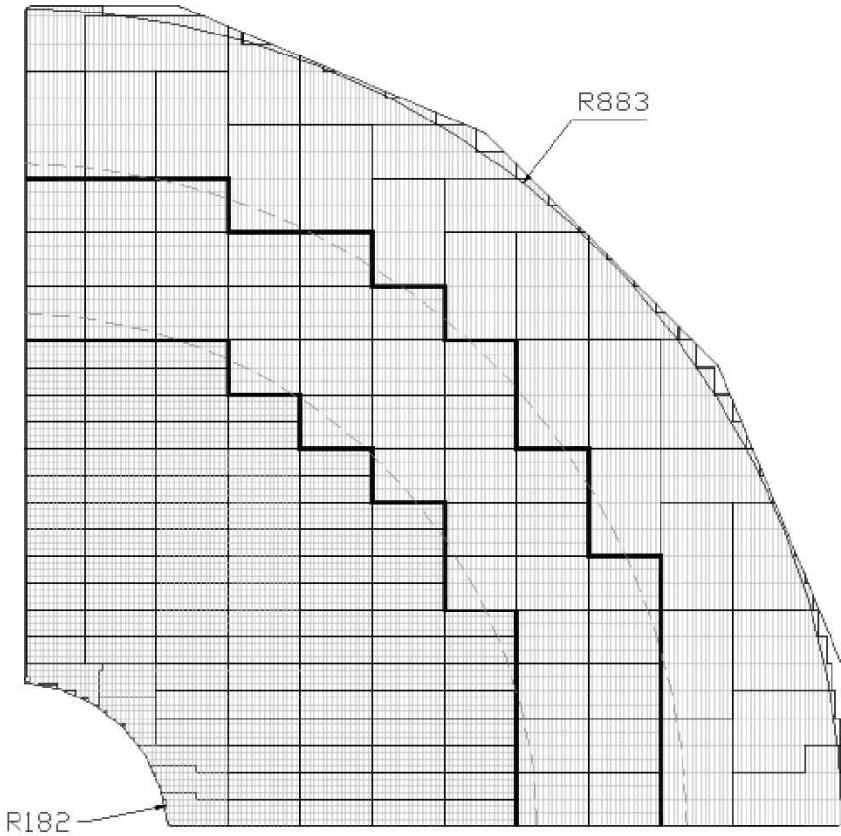


Figure 3.4: The cathode plane layout of Station 1 of the Tracking System of the Muon Spectrometer. Larger pads are used with larger distance from the beam line [7].

The dimensions of the ZN is limited by the space between the two beam pipes which is about 9 cm. Therefore a very dense material, such as the tungsten alloy, is used for the absorber to maximize the shower containment. The quartz fibres are placed 1.6 mm from each other to provide a good uniformity of the response as a function of the impact point and their position is  $0^\circ$  with respect to the incident particle direction of motion. The fibres transport the light right to the photomultipliers (PMTs) and the information from the PMTs provides the corresponding measurement of the shower energy. In Fig. 3.6 the ZN calorimeter can be seen.

The ZN calorimeters have been tested at the CERN SPS with hadron and electron/positron beams. The energy resolution has been measured as a function of  $1/\sqrt{E}$  and the result can be found in Fig. 3.7. Taken data were fitted and extrapolated to the energy per nucleon in Pb-Pb collisions at LHC,  $E = 2.7$  TeV. For the neutrons the energy resolution is about 11.4 %, compatible to the spectator energy fluctuations. Furthermore, since the ZN is divided in a four tower segmentation, it can be used as a rough position sensitive device. The measurements show that the ZN has good localizing properties and that it can be used to monitor the beam crossing angle at the interaction point and to reconstruct the event plane of the nucleus-nucleus collisions.

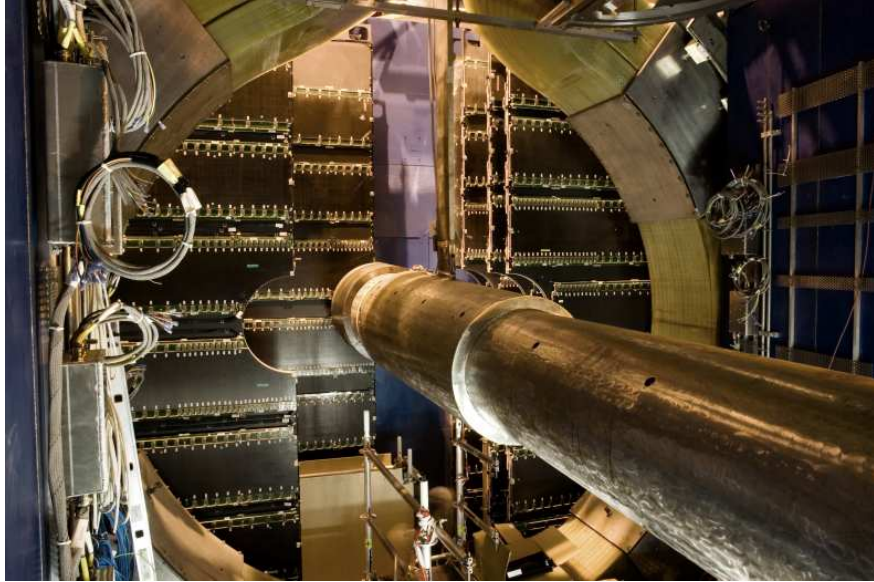


Figure 3.5: Layout of Tracking System Stations 4 and 5 which are located after the dipole magnet of the Muon Spectrometer [7].

### 3.3 The V0 detector

The V0 detector is a small angle detector located on both sides of the ALICE interaction vertex. The system provides minimum-bias or centrality triggers for the experiment and separates beam-beam interactions from beam-gas interactions. It is also used to measure physics quantities, such as beam luminosity, charged particle multiplicity and azimuthal distributions [24].

It consists of two arrays of scintillator counters, named V0A and V0C. The pseudo-rapidity ranges  $2.8 < \eta < 5.1$  and  $-3.7 < \eta < -1.7$  for V0A and V0C, respectively. The V0A is placed at a distance of 239 cm from the interaction point and the V0C is fixed on the front face of the front absorber, 90 cm from the interaction point. Each array is segmented in four rings in the radial direction and each ring is divided into eight sections in the azimuthal direction. Segments of both arrays are made of a plastic scintillator of a thickness  $\sim 2$  cm and wavelength shifting fibres (WLS) are embedded on each segment as is shown in Fig. 3.8. The light from WLS is transferred to the photomultiplier tube (PMT) and then sent to the Front-End Electronics.

### 3.4 The AD detector

The main task carried by the AD is to participate at the level zero of the trigger system of ALICE, but also the AD detector enhances the efficiency to study diffractive physics and photon induced processes. The system is capable of detecting minimum ionizing particles, therefore less background is expected for UPCs.

The system is installed in the forward rapidity region of ALICE [10]. The detectors are made of scintillation plastic pads stations which are located on both sides of the interaction point. One of the two stations is placed on the A side (ADA) at 18 me-

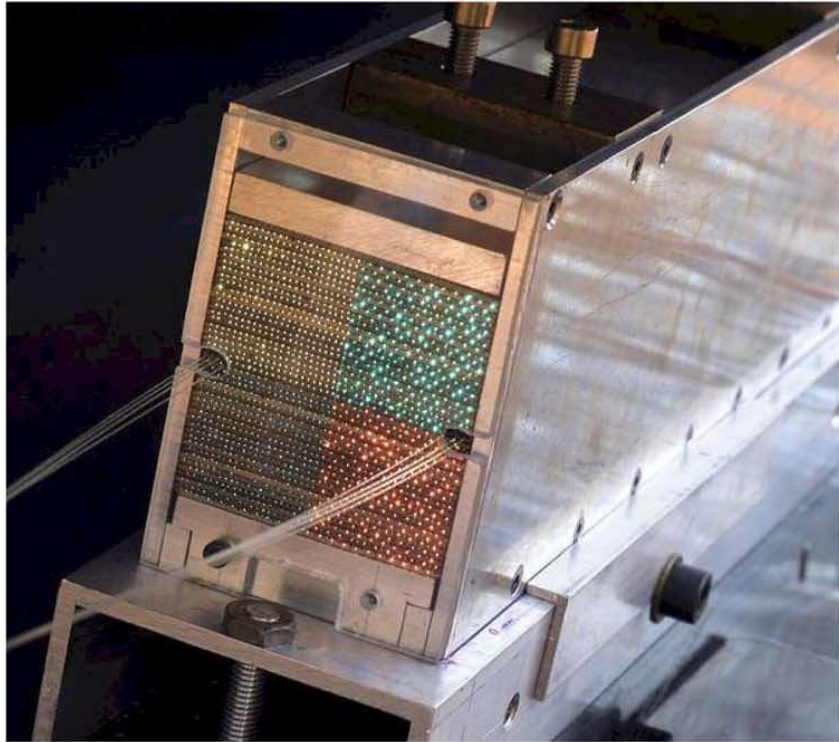


Figure 3.6: A photograph of the Zero Degree Neutron Calorimeter [8].

ters from the interaction point and it covers a pseudorapidity interval  $4.8 < \eta < 6.3$ . The second pad station is located on the opposite side (ADC), at 20 meters from the interaction point and it covers the pseudorapidity region  $-7.0 < \eta < -4.9$ .

Each AD detector consists of 8 cells of scintillation plastic of  $22 \times 22$  cm with thickness of 2.5 cm each. They are arranged around the beam pipe in two layers. The scintillation light is collected by Wave Length Shifters (WLS) which are attached on two sides of each cell. The WLS transfer the collected scintillation light to optical fibres where it is guided to Photomultiplier (PMT) and converted into an electric signal. The AD detector can be seen in Fig. 3.9.

The AD detector is one of detectors that is being upgraded recently because it would not cope with the conditions expected at the LHC in Run 3 and 4 [25]. The new upgraded diffractive detector is called the Forward Diffraction Detector (FDD). The set up of the FDD is the same as in AD, Each module is also made of a plastic scintillator, WLS, optical fibres and the PMTs. The geometry is the same, but the materials of the FDD are faster. the WLS bar re-emission time will be reduced from 8.5 ns to 0.9 ns. The new PMTs have 19 dynodes instead of 16 dynodes of the AD PMTs which will reduce after-pulses and also have a more extensive dynamic range. The AD and FDD have cover the same pseudorapidity regions.

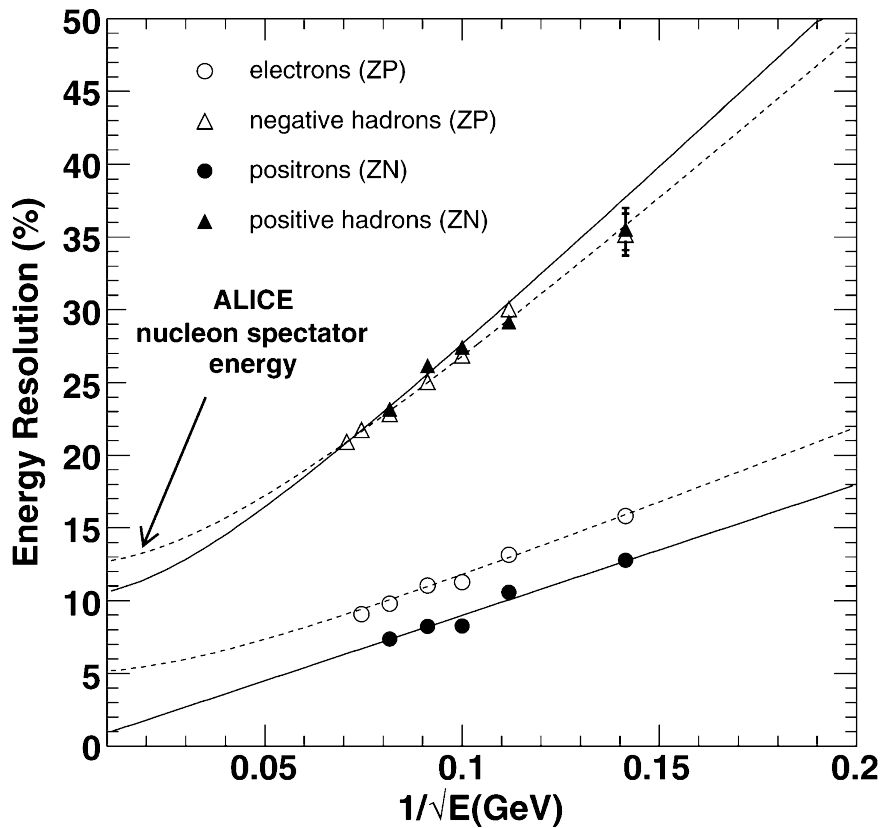


Figure 3.7: The energy resolution of Zero Degree Calorimeter measured for hadron and electron beams. It is measured in dependence on  $1/\sqrt{E(\text{GeV})}$  [8].

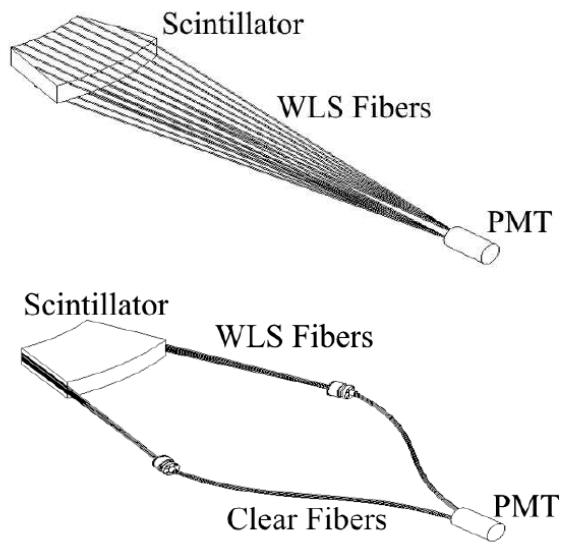


Figure 3.8: Schematic drawing of individual segment for V0A (top) and V0C (bottom) detectors with embedded WLS fibres and connected to a PMT [9].

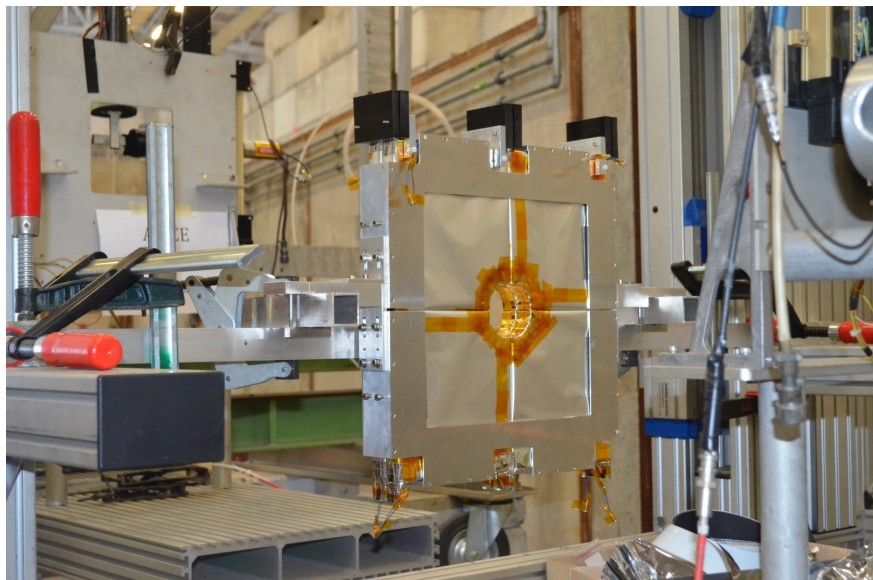


Figure 3.9: The ALICE Diffractive detector [10].

## Chapter 4

# A generator of forward neutrons for ultra-peripheral collisions: $n_0^0 n$

This section is dedicated to a published paper "A generator of forward neutrons for ultra-peripheral collisions:  $n_0^0 n$ " by Michal Broz and collaborators [11] that presents a program for generating forward neutrons. The generator is recently new tool, which we do not use yet. However, it is an important advance and it will be a good tool for next steps, such as determination of the ZN efficiency in different neutron classes, for example.

To generate vector mesons produced in a UPC event a Monte Carlo (MC) generator is used, for example STARlight. The STARlight MC can generate the vector mesons and provide cross section for events with forward neutrons, unfortunately, it does not provide final state neutrons in the event output. The generator  $n_0^0 n$ , apart from generating forward neutrons, takes as input either events produced by STARlight or theoretical predictions of vector meson photoproduction.

### 4.1 Probability of neutron emission

The theoretical formalism for vector meson production in UPCs accompanied by an electromagnetic dissociation (EMD) is summarized in this section. It is assumed that the sub-processes are independent, the cross section to produce a vector meson accompanied by a EMD is

$$\sigma(AA \rightarrow PA'_i A'_j) \propto \int d^2\vec{b} P_P(b) P_{ij}(b) P_{NH}(b), \quad (4.1)$$

where  $P$  denotes the final state, such as the vector meson  $J/\psi$  produced by the hard processes,  $A'_{i,j}$  is the ion after the neutron emission and  $\vec{b}$  is the impact parameter with its magnitude  $b$ . The subscripts  $i, j = 0, 1, 2, \dots$  are the numbers of neutrons emitted by the nucleus on A or C side. In the equation three independent probabilities appear:  $P_P(b)$  is the probability of the hard photoproduction process, which is given by a product of a photon flux and photonuclear cross section,  $P_{NH}(b)$  is the probability of no hadronic interaction and both terms were described in the Chapter 2. The probability

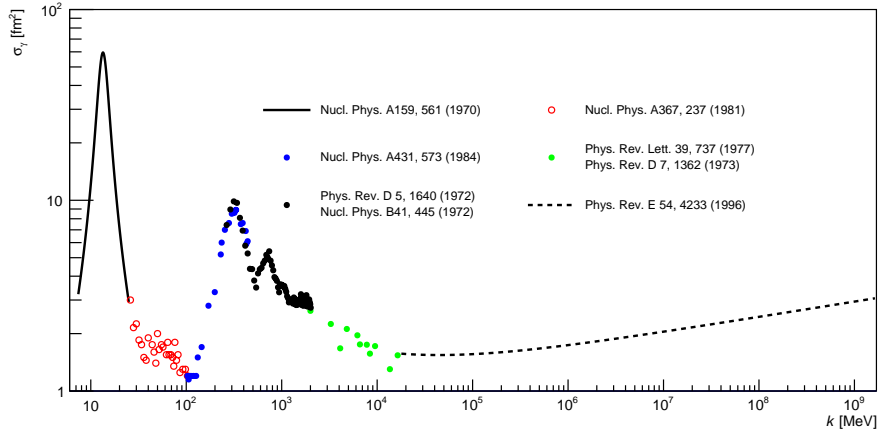


Figure 4.1: The cross section  $\sigma_{\gamma A \rightarrow A' + X_n}(k)$  for  $^{208}\text{Pb}$ . Various experiments and approaches are used to describe different energy ranges. Figure taken from [11].

$P_{ij}(b)$  denotes the probability of the nucleus break-up with emission of  $i, j$  forward neutrons. The neutron can be emitted independently by either nucleus.

#### 4.1.1 Probability of the nuclear break-up

The determination of the nuclear break-up probability is based on an assumption, that the process causing the break-up is totally independent. The probability is given by the product of the break-up probabilities of each nucleus as

$$P_{ij}(b) = P_i(b) \times P_j(b). \quad (4.2)$$

The procedure of  $P_i(b)$  determination is the following: The probability of having at least one excitation of one interacting nucleus is given by:

$$P_{Xn}(b) = 1 - \exp(-P_{Xn}^1(b)), \quad (4.3)$$

where  $P_{Xn}^1$  is the mean number of the Coulomb excitations of the nucleus to any state which emits one or more neutrons. The mean number is computed as a product of the photon flux and a cross section of the Coulomb excitation with emission of one or more neutrons as shown below:

$$P_{Xn}^1(b) = \int dk \frac{d^3 n(b, k)}{dk d^2 b} \sigma_{\gamma A \rightarrow A' + X_n}(k). \quad (4.4)$$

The cross section  $\sigma_{\gamma A \rightarrow A' + X_n}(k)$  for  $^{208}\text{Pb}$  is determined using experimental data from several fixed-target experiments and it is shown in Fig. 4.1. The photon energy reached in the considered experiments covers the interval up to  $k < 16.4$  GeV. One can notice that the values in measured energy range correspond to the one shown in Chapter 2 in Section 2.3 that was discussed in depth. For larger energies the Regge theory parametrization is used. The mean number of Coulomb excitations given by Eq. 4.4 in dependence on the impact parameter is shown in Fig. 4.2.

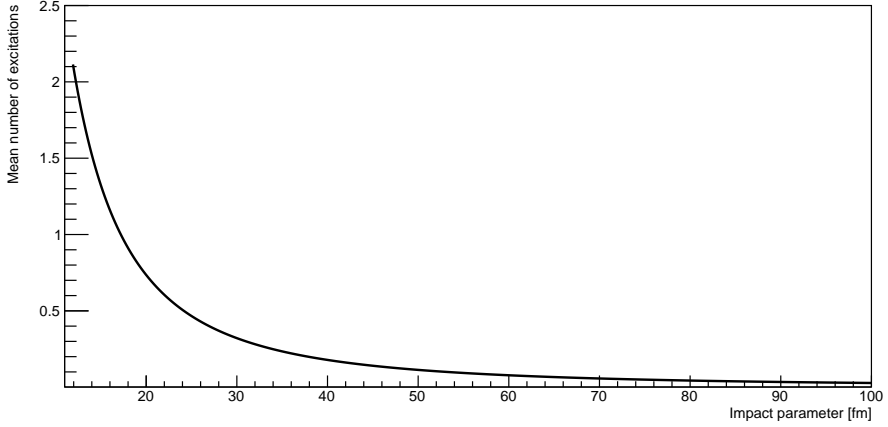


Figure 4.2: Mean number of excitations  $P_{Xn}^1(b)$  for case of Pb. Figure taken from [11].

The probability of a nucleus going to any state with one or more neutrons emitted is a sum of probabilities of a nucleus going into state with  $N$  neutrons:

$$P_{Xn}^1(b) = \sum_{N=1}^{\infty} P_{Nn}^1(b). \quad (4.5)$$

The probability of the Coulomb excitation of the nucleus to a state with  $N$  neutrons follows:

$$P_{Nn}^1(b) = \int dk \frac{d^3 n(b, k)}{dk d^2 b} \sigma_{\gamma A \rightarrow A' + Nn}(k), \quad (4.6)$$

Assuming a Poisson distribution, the probability to have exactly  $L$  neutrons emitted can be calculated from:

$$P_{Ln}(b) = \frac{(P_{Xn}^1(b))^L \times \exp(-P_{Xn}^1(b))}{L!} \quad (4.7)$$

and explicitly for first three terms one gets:

$$P_1(b) = P_{1n}^1(b) \times \exp(-P_{Xn}^1(b)), \quad (4.8)$$

$$P_2(b) = [P_{2n}^1(b) + \frac{(P_{1n}^1(b))^2}{2!}] \times \exp(-P_{Xn}^1(b)), \quad (4.9)$$

$$P_3(b) = [P_{3n}^1(b) + 2P_{2n}^1(b)P_{1n}^1(b) + \frac{(P_{1n}^1(b))^3}{3!}] \times \exp(-P_{Xn}^1(b)), \quad (4.10)$$

meaning for example, that a state with two neutrons can be produced either by direct two neutron emission or by two emissions of one neutron and similarly in cases of three and more neutrons. The generator computes break-up probabilities up to 50 neutrons and 5 excitations, which is enough for applications to RHIC and LHC. In order to use equations like Eq. 4.10, one needs to know the cross sections for the individual neutron multiplicities as seen in Eq. 4.6. Once the neutron multiplicities are known, we need to know the energy to give to each neutron. These two issues will be discussed in the next section.

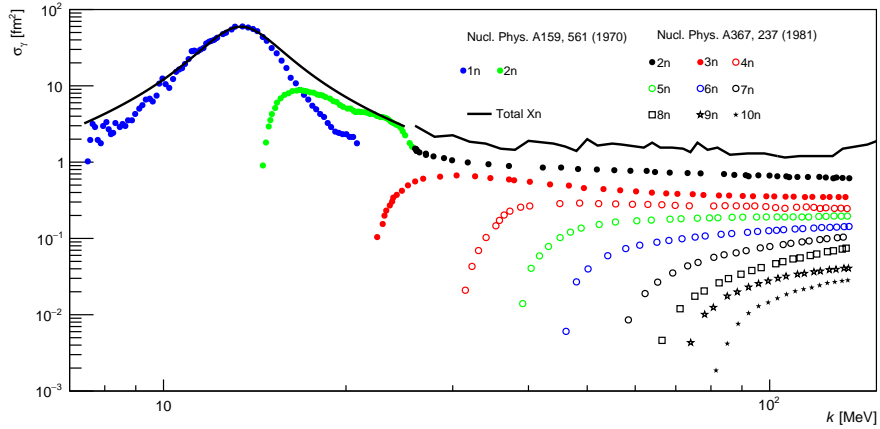


Figure 4.3: Partial cross section for  $^{208}\text{Pb}$  and various neutron multiplicities as measured by the experiments quoted on the figure. Figure taken from [11].

## 4.2 Generation of neutron multiplicity

To compute break-up of the nucleus to particular number of neutrons due to the Coulomb excitation the partial cross sections  $\sigma_{\gamma A \rightarrow A' + N_n}(k)$  are needed for the full photon energy range covered at the LHC.

The low energy region up to 140 MeV was studied in several experiments and these existing measurements of partial cross sections up to 10 neutrons were used. They are shown in Fig. 4.3. It can be seen that the largest cross section corresponds to the emission of one neutron and it decreases very rapidly with increasing number of emitted neutrons. The more neutrons emitted, the higher energy of an incident photon has to be. The total partial cross section is also shown in the figure with peak at the value of a photon energy in which one neutron is emitted. The total partial cross section is more or less flat at higher energies.

The partial cross sections were used to extract the averages and the dispersion of the number of neutrons as a function of the incident photon energy. The average was fitted to a logarithm and extrapolated to energies up to  $10^9$  MeV because no measurements going beyond the energy value of 140 MeV exist. It was found that this approach well describes the neutron multiplicity in dependence on the photon energy and it is shown in Fig. 4.4. Up to the incident photon energy 140 MeV the used data are shown and beyond this energy the logarithmic extrapolation is demonstrated. The line represents the average and the band shows the dispersion. The approach was compared with results of the RELDIS model, displayed with the dashed line, and they are in a good agreement.

The branching ratios to each partial cross section were computed and shown in Fig. 4.5 in dependence on the incident photon energy. The data from Fig. 4.4 were used with a Gaussian approximation for the shape. The largest branching ratio is for the incident photon energies up to 1 GeV and for higher energies the probability of emission of any neutron multiplicity decreases. In energy region from  $10^6$  to  $10^9$  MeV the most probable multiplicities are about 15 to 30 neutrons, for higher and lower multiplicities the branching ratio decreases.

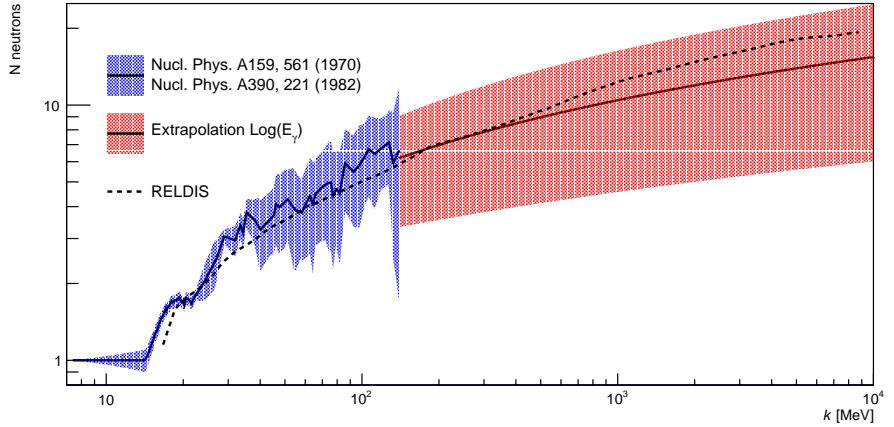


Figure 4.4: Arithmetic average (line) and dispersion (dashed area) of neutron multiplicity as a function of the incident photon energy. The approach used here and the prediction of the RELDIS model [12] are shown in red and with a dash line, respectively. Figure taken from [11].

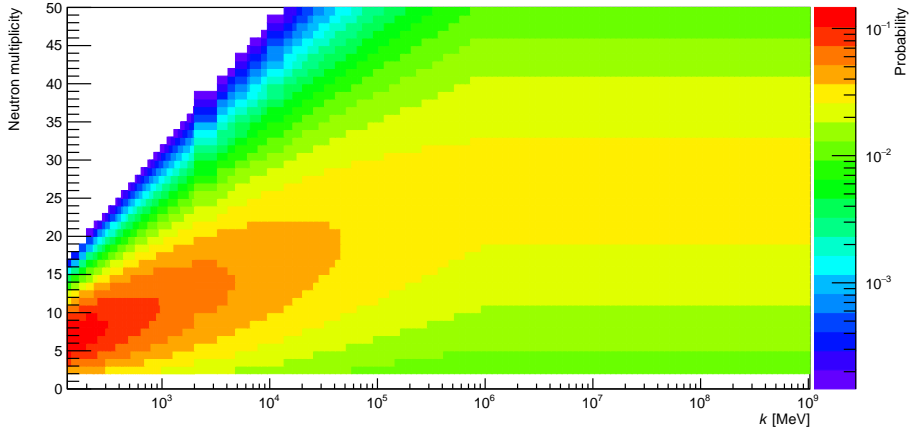


Figure 4.5: Branching ratio of the total cross section to different neutron multiplicities as a function of the incident photon energy up to  $10^9$  MeV. On the left vertical axes the number of neutrons is shown and the right vertical axes displays its probability estimated by a Gaussian approximation. Figure taken from [11].

### 4.3 Neutron energy generation

The emission spectra of the secondary particles are used from the Photonuclear Data for Applications project in the Evaluated Nuclear Data File (ENDF) fromat because there are very few measurements of the secondary particles spectra from a mono-energetic photon source available. The incident energy of photon is distributed according to the partial cross section and the neutrons are produced with an energy generated from the ENDF table. The emission spectra of neutrons are shown in Fig. 4.6. The energy of

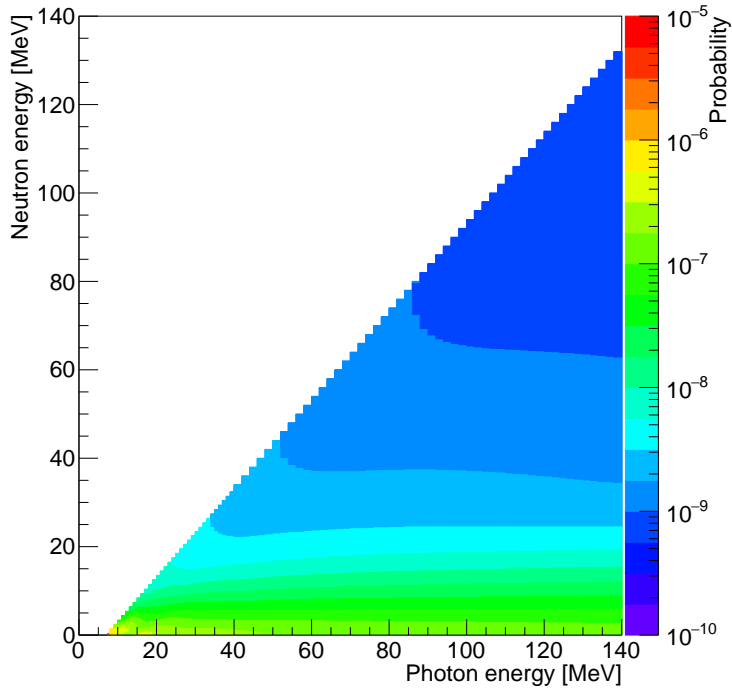


Figure 4.6: Emission spectra of secondary neutrons from photo-neutron reactions on  $^{208}\text{Pb}$  from evaluated nuclear data taken from ENDF database for full energy range up to 140 MeV. Figure taken from [11].

produced neutron is presented with displayed probability in dependence on the incident photon energy. The neutrons are produced in the rest frame of the nucleus with an isotropic angular distribution. Then, they are boosted to one or the other side of the detector, thus the energy that the neutrons are produced with is mostly negligibly low.

#### 4.4 Possible applications and conclusion

The program has several applications. Two examples are presented below.

It can be used, for example, in coupling with the STARlight generator. In Fig. 4.7 is shown the neutron multiplicity distributions for the coherent  $\rho^0$  at mid-rapidity for Run 2 LHC energies for events that were generated by the STARlight and coupled to the  $n_0^0 n$  generator, as an example of possible application. In the figure the probability of different neutron classes is shown. On the horizontal axes the number of neutrons from one beam is displayed and on the vertical axes the probability is shown for different number of neutrons produced by the second beam; the blue, red and green lines represent no, one and two neutrons produced from that beam.

Also theoretical predictions from models for photonuclear processes can be used as an input into  $n_0^0 n$ . As a second example, the predictions of the energy-dependent hot-spot model applied on the coherent photoproduction of a  $\rho^0$  and  $J/\psi$  vector mesons were taken as an input and using the  $n_0^0 n$  the predictions for the cross section were

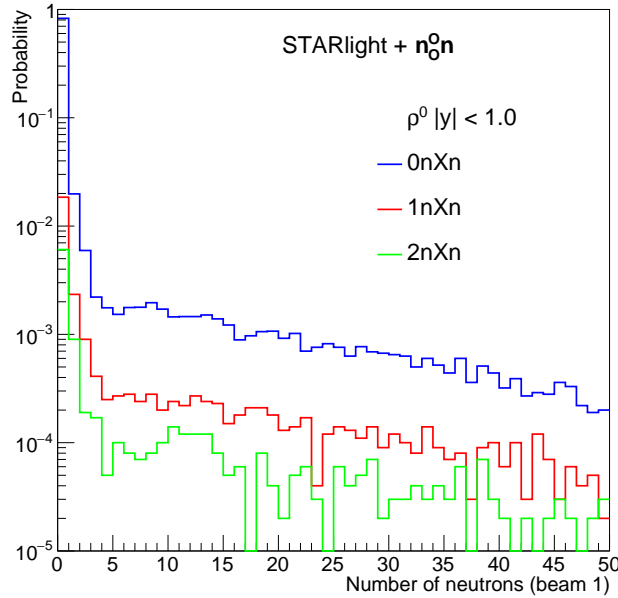


Figure 4.7: The probability of emission of neutron(s) for coherently produced  $\rho^0$  events, generated with the STARlight at mid-rapidity  $|y| < 1.0$ . The blue, red and green lines represent events with zero, one and two neutrons in one side and one or more neutrons produced in the other side. Figure taken from [11].

separated into the contributions of different neutron classes, as shown in Fig. 4.8. The total cross section prediction for coherent photoproduction of  $J/\psi$  in full rapidity range is shown with the black line. Different contributions are demonstrated, such as the case that no neutrons are produced in either side of the detector ( $0n0n$ ) displayed with the red line, neutrons produced in only one side ( $0nXn$ ) and with neutrons in both sides ( $XnXn$ ) shown with green and purple line, respectively.

The  $n_0^0n$  generator presented in this chapter is a new tool for production of neutrons that have the origin in electromagnetic dissociation interactions of heavy nuclei collisions. As an input the STARlight program or theoretical predictions for hard reactions in photonuclear processes can be used. It will help us in the next steps of studying the photo-induced processes.

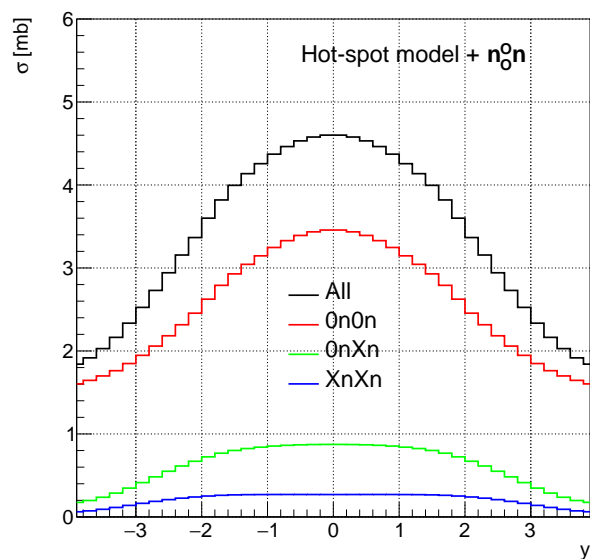


Figure 4.8: A cross section in rapidity dependence for  $J/\psi$  photoproduction predicted with the hot-spot model for different neutron classes generated with the  $n_0^0 n$ . Figure taken from [11].

## Chapter 5

# Measurements of coherent J/ $\psi$ production in UPCs

Photoproduction of coherent J/ $\psi$  in Pb–Pb UPCs was previously studied by the ALICE Collaboration at  $\sqrt{s_{NN}} = 2.76$  TeV. The coherent J/ $\psi$  production cross section was measured at midrapidity  $|y| < 0.9$  [26] and at forward rapidity  $-3.6 < y < -2.6$ . Also the CMS Collaboration studied the coherent J/ $\psi$  photoproduction accompanied by neutron emission at rapidity  $1.8 < |y| < 2.3$  at  $\sqrt{s_{NN}} = 2.76$  TeV. This chapter is dedicated to a summary of results from measurements of coherent J/ $\psi$  photoproduction in UPCs at forward and semi-forward rapidities, mentioned above. The first section reports results from two measurements of ALICE and CMS experiments. Papers reporting presented results are discussed in more detail in my previous work [17]. In the second section I discuss a published paper reporting results of measuring coherent J/ $\psi$  production in forward rapidities  $\sqrt{s_{NN}} = 5.02$  TeV with ALICE.

### 5.1 Measurements of photoproduction of J/ $\psi$ in UPCs with the ALICE and the CMS experiments.

The measurements of J/ $\psi$  photoproduction in forward and semi-forward rapidities [1, 2] at center-of-mass energy  $\sqrt{s_{NN}} = 2.76$  TeV were discussed in my previous work [17]. For completeness I briefly report the results from mentioned measurements in this section.

#### 5.1.1 Coherent J/ $\psi$ photoproduction in ultra-peripheral Pb–Pb collisions at $\sqrt{s_{NN}} = 2.76$ TeV [1]

The ALICE collaboration reported the very first measurement at the LHC of coherent J/ $\psi$  photoproduction in Pb–Pb UPCs at  $\sqrt{s_{NN}} = 2.76$  TeV. The J/ $\psi$  was measured in its dimuon decay channel in the forward rapidity region  $-3.6 < y < -2.6$ . Coherent candidates were obtained by selecting two muons with a transverse momentum  $p_T < 0.3$  GeV/c.

The analysis was based on a sample of events collected during the Pb–Pb run 2011, selected with a special trigger, called FUPC, and the corresponding integrated luminosity was about  $55 \mu\text{b}^{-1}$ . The FUPC trigger selects events containing two low- $p_T$

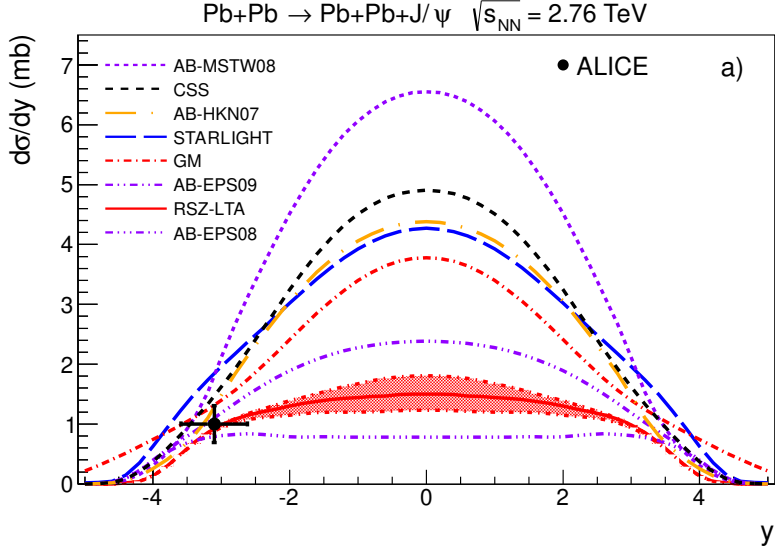


Figure 5.1: The differential cross section of coherently produced  $J/\psi$  at rapidity interval  $-3.6 < y < -2.6$  which is shown by the vertical bar of the measurement point. The error is quadratic sum of the statistical and systematic errors. With the colored curves different theoretical predictions are shown. Figure taken from [1].

muons from two-photon production or from  $J/\psi$  decay. A selection of coherent  $J/\psi$  candidates was applied and the coherent  $J/\psi$  differential cross section was calculated from:

$$\frac{d\sigma_{J/\psi}^{\text{coh}}}{dy} = \frac{N_{J/\psi}^{\text{coh}}}{\mathcal{B}(J/\psi \rightarrow \mu^+\mu^-) \mathcal{L}_{\text{int}} \Delta y (A \times \epsilon)_{J/\psi} \epsilon_{\text{trig}}} \quad (5.1)$$

where  $N_{J/\psi}^{\text{coh}}$  is the number of  $J/\psi$  candidates,  $(A \times \epsilon)_{J/\psi}$  corresponds to the acceptance and efficiency of the muon spectrometer, which is obtained from a sample of  $J/\psi$  events generated by STARlight, and  $\epsilon_{\text{trig}}$  is the V0 trigger efficiency.  $BR(J/\psi \rightarrow \mu^+\mu^-) = 5.93\%$  is the branching ratio for  $J/\psi$  decay into two muons,  $\Delta y = 1$  the rapidity bin size, and  $L_{\text{int}}$  the total integrated luminosity. The final result of a differential cross section for coherent  $J/\psi$  production was computed to be  $d\sigma_{J/\psi}^{\text{coh}}/dy = 1.00 \pm 0.18(\text{stat})^{+0.24}_{-0.26}(\text{syst})$  mb. The cross section is compared with various theoretical model calculations and it is shown in Fig. 5.1. Models which include nuclear gluon shadowing consistent with the EPS09 or EPS08 parameterizations are in the best agreement with the data.

### 5.1.2 Coherent $J/\psi$ photoproduction on ultra-peripheral Pb–Pb collisions at $\sqrt{s_{NN}} = 2.76$ with the CMS experiment [2]

The CMS collaboration measured a cross section of the coherent  $J/\psi$  photoproduction in Pb–Pb UPCs at  $\sqrt{s_{NN}} = 2.76$  TeV. The UPC trigger selected events with at least one neutron in either forward or backward direction from the interaction point using zero degree calorimeters. A sample of triggered events includes coherent, incoherent  $J/\psi$  mesons and  $\gamma + \gamma \rightarrow \mu^+\mu^-$  with at least one neutron produced in either side of the CMS

detector. The  $J/\psi$  candidates are reconstructed through the dimuon decay channel in the rapidity interval  $1.8 < |y| < 2.3$  and the cross section of coherently produced  $J/\psi$  mesons accompanied by at least one neutron from independent electromagnetic processes is measured. For the analysis, only events with dimuon  $p_T < 1.0 \text{ GeV}/c$  threshold were selected in the the rapidity interval.

The trigger designed to record UPC  $J/\psi$  vector mesons and dimuon from two-photon processes event was used. It requires an energy deposit consistent with at least one neutron in either of the ZDCs, no activity in at least one of the Beam Scintillator Counters (BSC+ or BSC-), which is used for triggering purposes, the presence of at least one single muon without a  $p_T$  threshold requirement, and at least one track in the pixel detector.

The invariant mass for a  $J/\psi$  candidates was required to be within an interval  $2.6 < m(\mu^+\mu^-) < 3.5 \text{ GeV}/c^2$ . The coherent  $J/\psi$  yield dominates for low- $p_T$  candidates and were selected by  $p_T < 0.15 \text{ GeV}/c$  cut. For the neutron class ( $Xn0n$ ), corresponding to at least one neutron measured on either one side and no neutrons in the other side, the coherent  $J/\psi$  cross section in the dimuon decay channel is given by:

$$\frac{d\sigma_{(Xn0n)}^{\text{coh}}}{dy}(J/\psi) = \frac{N_{(X_n0_n)}^{\text{coh}}}{\mathcal{B}(J/\psi \rightarrow \mu^+\mu^-) \mathcal{L}_{\text{int}} \Delta y (A \times \epsilon)^{J/\psi}} \quad (5.2)$$

where  $\mathcal{B}(J/\psi \rightarrow \mu^+\mu^-) = 5.96 \pm 0.03(\text{syst.})\%$  is the branching ratio of  $J/\psi$  decay to dimuons,  $N_{(X_n0_n)}^{\text{coh}}$  is the coherent  $J/\psi$  yield of prompt  $J/\psi$  candidates for  $p_T < 0.15 \text{ GeV}/c$  corrected for coherent  $J/\psi$  mesons from decays of  $\Psi'$ .  $\mathcal{L}_{\text{int}} = 159 \pm 8(\text{syst.}) \mu b^{-1}$  is the integrated luminosity,  $\Delta y = 1$  is the rapidity bin width and  $(A \times \epsilon)^{J/\psi} = 5.9 \pm 0.5(\text{stat.})\%$  is the combined acceptance times efficiency correction factor obtained from the STARlight event generator.

The coherent  $J/\psi$  photoproduction cross section for  $J/\psi$  mesons in the ( $Xn0n$ ) break-up mode is  $\frac{d\sigma_{(Xn0n)}^{\text{coh}}}{dy(J/\psi)} = 0.36 \pm 0.04(\text{stat}) \pm 0.04(\text{syst}) \text{ mb}$ . Using the STARlight generator, the scaling factor between the ( $Xn0n$ ) break-up mode and the total cross section was obtained and equaled to  $5.1 \pm 0.5(\text{theo.})$ . After applying this scaling factor the total cross section was calculated:  $\frac{d\sigma^{\text{coh}}}{dy(J/\psi)} = 1.82 \pm 0.22(\text{stat}) \pm 0.20(\text{syst}) \pm 0.19(\text{theo.}) \text{ mb}$ . The result is shown in Fig. 5.2 and it is compared to the theoretical predictions and results from measurements of the ALICE collaboration in different rapidity intervals.

## 5.2 Coherent $J/\psi$ photoproduction at forward rapidity in ultra-peripheral Pb–Pb collisions at $\sqrt{s_{NN}} = 5.02 \text{ TeV}$ [3]

The analysis presented in this paper is based on a data sample from 2015 and 2018 data taking periods at  $\sqrt{s_{NN}} = 5.02 \text{ TeV}$ . These two periods are characterized by similar conditions and detector performance. Two oppositely charged tracks in the muon spectrometer and vetoes on V0A, ADA and ADC beam-beam interactions were required by the trigger. The transverse momentum threshold to trigger single muon was set to  $p_T = 1 \text{ GeV}/c$ . The estimated luminosities for 2015 and 2018 were  $216 \mu b^{-1}$  and  $538 \mu b^{-1}$ , respectively.

The selection of events included: only two tracks with opposite electric charge in the muon spectrometer, the pseudorapidity of each track in the range  $-4.0 < \eta < -2.5$

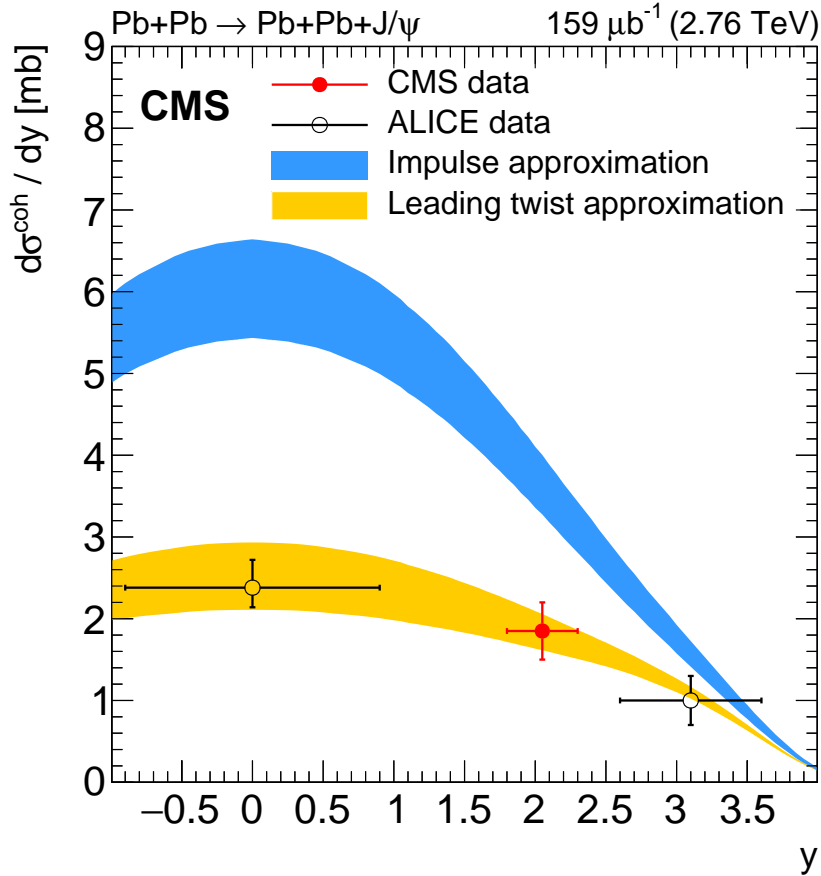


Figure 5.2: Differential cross section in dependence on rapidity for coherently photoproduced  $J/\psi$  measured by CMS and ALICE. The horizontal bars represent the rapidity range of the measurements and the vertical error bars include statistical and systematic uncertainties. Figure taken from [2].

and the tracks fulfill the requirements that were described in antecedent published paper studying the photoproduction of  $J/\psi$  on ALICE [1].

To ensure the exclusivity of only two muons detection, at most two fired cells in V0C were required. Also in addition to online vetoes on V0C, ADA and ADC detectors, offline vetoes were applied. The online veto works with a significant inefficiency which is due to hadronic or electromagnetic pile-up processes. These interactions accompany the coherent  $J/\psi$  photoproduction and were estimated to be less than 0.2% for hadronic pile-up but significantly larger for electromagnetic process  $\gamma\gamma \rightarrow e^+e^-$ . The veto inefficiency from these processes was estimated using unbiased events. Probability of detecting activity in particular detectors was found to scale linearly with the average number of collisions per bunch crossing. The veto inefficiency correction factors were determined by weighting the corresponding probabilities over periods with different pile-up conditions. For each period the luminosity was taken as a weight.

The veto inefficiency of V0A was found to be  $p_{V0A} = 4.6 \pm 0.2\%$  and in ADA and ADC it was found to be about 0.2% because these detectors are located far from the

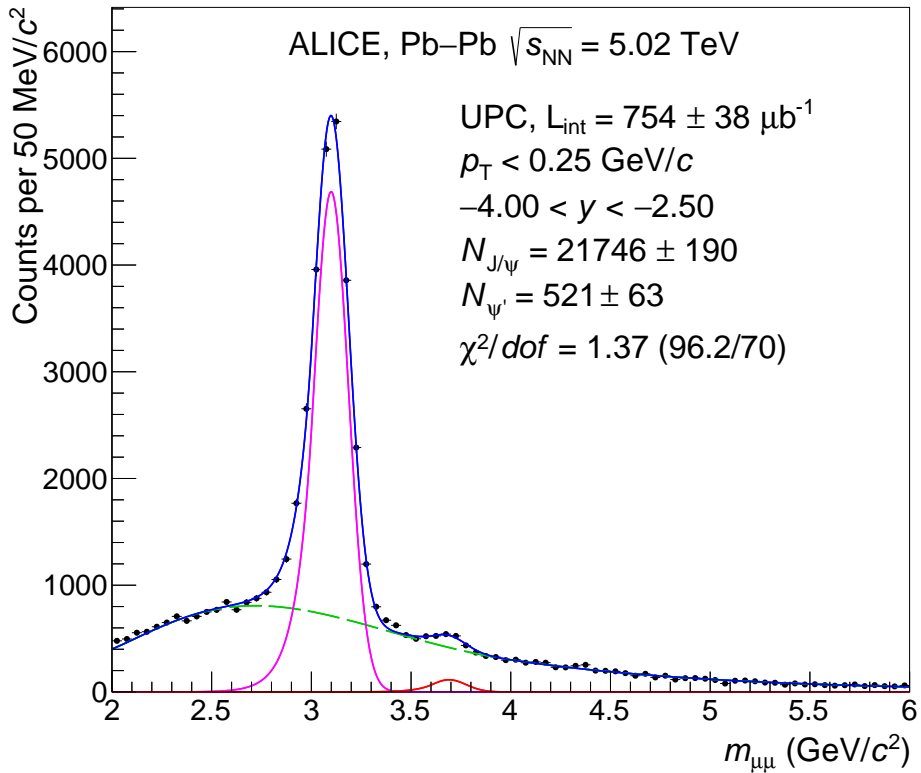


Figure 5.3: Invariant mass distribution for muon pairs. The pink and red lines correspond to Crystall Ball functions representing  $J/\psi$  and  $\Psi'$  signals. The dashed green line corresponds to the background and the solid blue line corresponds to the sum of background and signal functions [3].

interaction point therefore they are not that much affected by soft  $e^+e^-$  pairs. The veto inefficiency in V0C detector was found to be negligible. The average veto efficiency was calculated as  $\epsilon_{veto} = (1 - p_{V0A})(1 - p_{ADA})(1 - p_{ADC})$  and the presented result was  $\epsilon_{veto} = 95.0\%$  and was applied to  $J/\psi$  yields to take into account hadronic and electromagnetic pile-up processes.

The acceptance and efficiency of  $J/\psi$  and  $\Psi'$  was evaluated using a larger data sample generated by STARlight, the acceptance and efficiency of feed-down  $\Psi' \rightarrow J/\psi + \pi\pi$  were obtained from the STARLight generator. It was assumed that the transverse polarization of  $\Psi'$  comes in the feed-down  $J/\psi$ .

To ensure the the coherent  $J/\psi$  candidates in the sample, muon pairs with transverse momentum  $p_T < 0.25$  GeV were selected. The invariant mass distribution for selected unlike-sign muon pairs in the rapidity range  $-4.0 < y < -2.5$  is shown in Fig. 5.3. The invariant masses of coherently photoproduced  $J/\psi$  and  $\Psi'$  are fitted by Crystal Ball functions. The background is fitted by the template of events corresponding to the process  $\gamma\gamma \rightarrow \mu^+\mu^-$  made in STARLight. The forth-order polynomial is used to parameterize the result and it smoothly turns into an exponential tail as from 4  $\text{GeV}/c^2$ . The fitted curve agrees within 2.5 standard deviations with the value received from the generated data set.

The amount of produced  $J/\psi$   $N_{J/\psi}$  was obtained from the Crystal Ball fit of the

dimuon invariant mass spectrum in the range  $2.2 < m_{\mu^+\mu^-} < 6 \text{ GeV}/c^2$ . However, it contains contributions from both coherent and incoherent  $\text{J}/\psi$  candidates. The invariant mass obtained from the fit was  $m_{\text{J}/\psi} = 3.0993 \pm 0.0009 \text{ GeV}/c^2$ , which is in good agreement with the PDG value within 3 standard deviations. The raw inclusive  $\Psi'$  yield  $N_{\Psi'}$  is also obtained from the mass fit, however the mass of  $\Psi'$  is fixed due to the small statistics.

Coherent and incoherent photoproduction are separated studying the transverse momentum spectra. The  $p_T$  distribution of the dimuon pair with  $2.85 < m_{\mu^+\mu^-} < 3.35 \text{ GeV}/c^2$  is shown in Fig. 5.4 in the rapidity interval  $-4.0 < y < 2.5$ , also different rapidity subranges were measured and are collected in Fig. 5.5. These distributions were fitted with templates produced using STARLight generator. The data templates correspond to various production mechanisms, which contribute to the final template, such as: coherent and incoherent  $\text{J}/\psi$  production, feed-down  $\text{J}/\psi$  from coherent and incoherent  $\Psi'$  decays and continuum dimuons from  $\gamma\gamma$  interactions. The incoherent  $\text{J}/\psi$  photoproduction accompanied by nucleon dissociation was considered in the fits for a better description of the tail formed at the high- $p_T$ . The templates provided by the H1 collaboration measurements of the dissociative  $\text{J}/\psi$  photoproduction were used to get the fitting equation:

$$\frac{dN}{dp_T} \sim p_T (1 + \frac{b_{pd}}{n_{pd}} p_T^2)^{-n_{pd}}, \quad (5.3)$$

where the fit parameters are obtained from H1 measurements with different photon-proton center-of-mass energy intervals. The extracted incoherent  $\text{J}/\psi$  fraction  $f_1 = \frac{N_{\text{J}/\psi_{\text{incoherent}}}}{N_{\text{J}/\psi_{\text{coherent}}}}$  for  $p_T < 0.25 \text{ GeV}/c$  was determined to range from 3.2 % to 6.1 %. The value depends on the rapidity interval and is consistent within the uncertainties of the fits, see Tab. 5.1. In this fraction the contribution of incoherent  $\text{J}/\psi$  with nucleon dissociation was taken into account.

From the invariant mass spectra, the fraction of  $\Psi'$  and  $\text{J}/\psi$  yields was extracted with result:

$$R_N = \frac{N_{\Psi'}}{N_{\text{J}/\psi}} = 0.025 \pm 0.003(\text{stat.}) \quad (5.4)$$

Although the yields include both coherent and incoherent events, the  $R_N$  ratio can be considered as a good estimate of the ratio of coherent yields. This is because the fraction of incoherent  $\text{J}/\psi$  in the raw  $\text{J}/\psi$  yields does not exceed 6 % and the fraction of incoherent  $\Psi'$  is expected to be similar in the raw  $\Psi'$  yields. The ratio can also be expressed in terms of the primary coherent photoproduction cross section  $\sigma(\Psi')$  and  $\sigma(\text{J}/\psi)$  integrated over all transverse momenta in the rapidity range  $-4.0 < y < -2.5$ :

$$R_N = \frac{\sigma(\Psi') BR(\Psi' \rightarrow \mu\mu) \varepsilon(\Psi')}{\sigma(\text{J}/\psi) BR(\text{J}/\psi \rightarrow \mu\mu) \varepsilon(\text{J}/\psi) + \sigma(\Psi') BR(\Psi' \rightarrow \text{J}/\psi) \varepsilon(\Psi' \rightarrow \text{J}/\psi) BR(\text{J}/\psi \rightarrow \mu\mu)}, \quad (5.5)$$

where  $\varepsilon(\text{J}/\psi) = 12.0\%$ ,  $\varepsilon(\Psi') = 15.8\%$  and  $\varepsilon(\Psi' \rightarrow \text{J}/\psi) = 7.2\%$  are the efficiency corrections for primary coherent  $\text{J}/\psi$ ,  $\Psi'$  and feed-down  $\text{J}/\psi$  from coherent  $\Psi'$  decays estimated with STARLight, while  $BR(\text{J}/\psi \rightarrow \mu\mu) = (5.961 \pm 0.033)\%$ ,  $BR(\Psi' \rightarrow \mu\mu) = (0.80 \pm 0.06)\%$ ,  $BR(\Psi' \rightarrow \text{J}/\psi + \text{anything}) = (61.4 \pm 0.6)\%$  are the corresponding branching ratios. Equation 5.5 and the measured  $R_N$  value were used to extract the ratio of primary coherent  $\Psi'$  and  $\text{J}/\psi$  photoproduction cross sections:

$$R = \frac{\sigma(\Psi')}{\sigma(\text{J}/\psi)} = 0.150 \pm 0.018(\text{stat.}) \pm 0.021(\text{syst.}) \pm 0.007(\text{BR}). \quad (5.6)$$

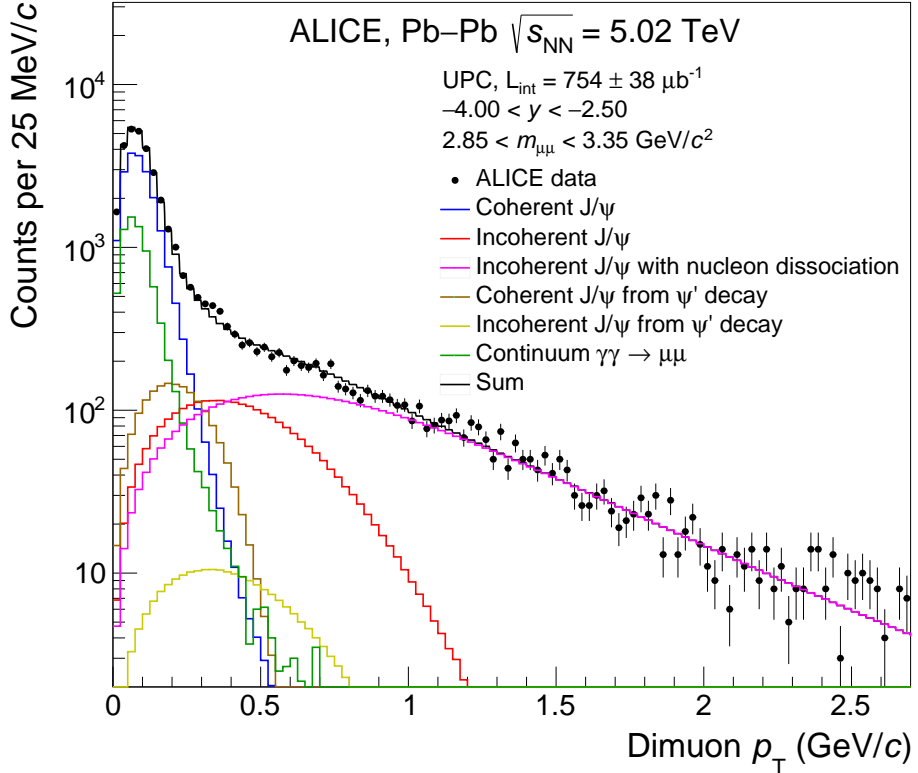


Figure 5.4: Transverse momentum distribution for muon pairs in range  $2.85 < m_{\mu\mu} < 3.35 \text{ GeV}/c^2$ . Figure taken from [3].

The measured ratio of the cross sections is in good agreement with data from H1 ep measurements ( $R \approx 0.166$ ) and with LHCb pp experiments ( $R \approx 0.19$ ). The value of  $R$  also satisfies the Leading Twist Approximation predictions, which spreads from 0.13 to 0.18. The measured coherent  $\Psi'$  to  $J/\psi$  cross section ratio was compared to the ration measured by ALICE at central rapidity in Pb–Pb UPCs at  $\sqrt{s_{\text{NN}}} = 2.76 \text{ TeV}$ . They obtained the result  $R = 0.34^{+0.08}_{-0.07}$ . The value is more than doubled, but it is still within 2.5 standard deviations.

From the measured cross section ratio  $F$  the fraction of feed-down  $J/\psi$  from  $\Psi'$  and primary  $J/\psi$  yield was extracted:

$$f_D = \frac{N(\text{feed-down } J/\psi)}{N(\text{primary } J/\psi)} = R \frac{\epsilon(\Psi' \rightarrow J/\psi)}{\epsilon(J/\psi)} BR(\Psi' \rightarrow J/\psi) \quad (5.7)$$

The obtained values were  $f_D = 8.5\% \pm 1.5\%$  for full rapidity range without any  $p_T$  cut. For transverse momentum cut  $p_T < 0.25 \text{ GeV}/c$  the result was  $f_D = 5.5\% \pm 1.0\%$  because the feed-down  $J/\psi$  are characterized by larger  $p_T$  distribution than primary  $J/\psi$ .

Finally, the coherent  $J/\psi$  differential cross section is given by:

$$\frac{d\sigma_{J/\psi}^{\text{coh}}}{dy} = \frac{N(J/\psi)}{(1 + f_I + f_D)\epsilon(J/\psi)BR(J/\psi \rightarrow \mu\mu)\epsilon_{\text{veto}}L_{\text{int}}\Delta y}, \quad (5.8)$$

| rapidity range | $N_{J/\psi}$    | $\epsilon$ | $f_D$ | $f_I$ | $d\sigma_{J/\psi}^{\text{coh}}/dy$ (mb)                |
|----------------|-----------------|------------|-------|-------|--|
| (−4.00, −2.50) | $21747 \pm 190$ | 0.120      | 0.055 | 0.055 | $2.549 \pm 0.022$ (stat.) $^{+0.209}_{-0.237}$ (syst.) |
| (−4.00, −3.75) | $974 \pm 36$    | 0.051      | 0.055 | 0.060 | $1.621 \pm 0.061$ (stat.) $^{+0.135}_{-0.148}$ (syst.) |
| (−3.75, −3.50) | $3217 \pm 70$   | 0.140      | 0.055 | 0.059 | $1.936 \pm 0.042$ (stat.) $^{+0.166}_{-0.190}$ (syst.) |
| (−3.50, −3.25) | $5769 \pm 98$   | 0.204      | 0.055 | 0.061 | $2.376 \pm 0.040$ (stat.) $^{+0.212}_{-0.229}$ (syst.) |
| (−3.25, −3.00) | $6387 \pm 105$  | 0.191      | 0.055 | 0.052 | $2.830 \pm 0.047$ (stat.) $^{+0.253}_{-0.280}$ (syst.) |
| (−3.00, −2.75) | $4229 \pm 85$   | 0.119      | 0.055 | 0.051 | $3.014 \pm 0.061$ (stat.) $^{+0.259}_{-0.294}$ (syst.) |
| (−2.75, −2.50) | $1190 \pm 47$   | 0.029      | 0.054 | 0.032 | $3.585 \pm 0.141$ (stat.) $^{+0.298}_{-0.368}$ (syst.) |

Table 5.1:  $J/\psi$  yields, efficiencies,  $f_I$  and  $f_D$  fractions and coherent  $J/\psi$  cross sections [3].

| Source                            | Value  |
|-----------------------------------|--|
| Lumi. normalization               | $\pm 5.0\%$  |
| Branching ratio                   | $\pm 0.6\%$  |
| SPD, V0 and AD veto               | from $-3.6\%$ to $-6.0\%$                          |
| MC rapidity shape                 | from $\pm 0.1\%$ to $\pm 0.8\%$                    |
| Tracking                          | $\pm 3.0\%$  |
| Trigger                           | from $\pm 5.2\%$ to $\pm 6.2\%$                    |
| Matching                          | $\pm 1.0\%$  |
| Signal extraction                 | $\pm 2.0\%$  |
| $f_D$ fraction                    | $\pm 0.7\%$  |
| $\gamma\gamma$ yield              | $\pm 1.2\%$  |
| $p_T$ shape for coherent $J/\psi$ | $\pm 0.1\%$  |
| $b_{pd}$ parameter                | $\pm 0.1\%$  |
| Total                             | from $^{+8.3\%}_{-9.2\%}$ to $^{+8.9\%}_{-10.3\%}$ |

Table 5.2: Summary of systematic uncertainties. The ranges of values correspond to different rapidity bins [3].

where  $N(J/\psi)$  is the  $J/\psi$  yield extracted from the invariant mass fit,  $(1 + f_I + f_D)$  correspond to the incoherent and feed-down fractions,  $\epsilon_{veto}$  is the veto efficiency,  $L_{\text{int}}$  is the integrated luminosity and  $\Delta y$  is the rapidity bin. All calculated values of the  $J/\psi$  yields, fractions  $f_I$ ,  $f_D$ , the efficiency and cross sections are summarized in Tab. 5.1 for different rapidity intervals. The systematic uncertainties are determined from the composition of several different sources which are briefly described next. The first source of systematic uncertainty is related to the separation of peripheral and ultra-peripheral collisions with results from 12.6 % to 15.0 % lower  $J/\psi$  yields which differs the cross sections 3.6 % to 6.0 % lower with dependence on rapidity range. The systematic uncertainties on efficiencies were obtained by variation of the generated rapidity, the tracking efficiency, dimuon trigger efficiency and uncertainty of matching track segments reconstructed in the tracking and trigger chambers were taken into account. Also the uncertainty of the raw  $J/\psi$  signal extraction was included. And finally, systematic uncertainties associated with different contributions to the  $p_T$  spectrum also contributed to the total systematic uncertainty on the coherent cross section. All systematic uncertainties are summarized in the Tab. 5.2. The total systematic uncertainty is the quadratic sum of all sources.

The measured differential cross section of coherently photoproduced  $J/\psi$  is shown

in Fig. 5.6. It is plotted in dependence of the rapidity range  $-4.0 < y < -2.5$  and it is compared with several models which are briefly described below. The covered rapidity ranges correspond to a Bjorken- $x$  of  $x \in (1.1 \cdot 10^{-5}; 5.1 \cdot 10^{-5})$  or  $x \in (0.7 \cdot 10^{-2}; 3.3 \cdot 10^{-2})$  in dependence on which nucleus is the emitter of the photon and which one is the target. According to models, the fraction of high Bjorken- $x$  gluons dominates at forward rapidities. The fraction was estimated to range from  $\approx 60\%$  at  $y = -2.5$  to  $\approx 95\%$  at  $y = -4.0$ .

The Impulse Approximation cross section overestimates the experimental points. The model is based on data from exclusive  $J/\psi$  photoproduction off protons and it neglects all nuclear effects except the coherence. The overestimation of the model reflects the magnitude of the nuclear shadowing factor of 0.8 at Bjorken- $x$  values around  $10^{-2}$  with assumption of neglecting the contribution from low  $Bjorken-x \sim 10^{-5}$  gluons.

The STARlight model is based on Vector Meson Dominance model and a parametrization of the existing data on  $J/\psi$  photoproduction off protons. Multiple nuclear interactions are taken into account in the model but gluon shadowing corrections. This model also overpredicts the data, indicating the importance of gluon shadowing effects.

Two models provided by Guzey, Kryshen and Zhalov are compared to the data. Models EPS09 LO and the Leading Twist Approximation take into account the nuclear gluon shadowing effects, both models underestimate the data. However, the data are within the EPS09 LO uncertainties and follow the upper limit which corresponds to the upper bound of uncertainties on the gluon shadowing factor in the EPS09 LO framework.

Several models based on the color dipole approach coupled to the Color Glass Condensate formalism were provided by theoretical groups with different assumptions on the dipole-proton scattering amplitude. None of the models are in a good agreement with the experimental points in the full rapidity range. Cepila, Contreras and Krelina provided predictions based on the extension of the energy dependent hot-spot model to the nuclear case. The GG-HS model follows the data at most forward rapidities but underestimates it at semi-forward rapidities.

To conclude the published paper: the first measurement of the coherent photoproduction of  $J/\psi$  in different rapidity bins within the range  $-4.0 < y < -2.5$  was presented for ultra-peripheral Pb–Pb collisions at  $\sqrt{s_{NN}} = 5.02$  TeV. The result of the cross section was compared to several theoretical models and the gluon shadowing effects were shown to be important contribution.

### 5.3 Summary of results from previous measurements of the coherent $J/\psi$ photoproduction

The measurements of coherent  $J/\psi$  photoproduction cross section in forward and semi-forward rapidity region published up to now were briefly described in this chapter. The results compared with various theoretical predictions were shown and a summary of results from discussed measurements is listed in Tab. 5.3.

Comparing the results with several theoretical models, parametrization provided by Guzey, Kryshen and Zhalov EPS09 LO describes the data within its uncertainty. This model takes into account nuclear gluon shadowing, neglecting the low Bjorken- $x$  contribution.

A data sample taken in 2018 is the data sample that I use in the analyses presented in next two chapters.

Table 5.3: Tabel of summarized results of measured differential cross section of coherent J/ $\psi$  photoproduction in forward rapidities published in [1, 2, 3]. First two measurements were at center-of-mass energy  $\sqrt{s_{NN}} = 2.76$  TeV and the latest measurement of ALICE collaboration at  $\sqrt{s_{NN}} = 5.02$  TeV.

| Collaboration | Luminosity [ $\mu b^{-1}$ ] | Rapidity interval y | Differential cross section [mb]                                 |
|---------------|-----------------------------|---------------------|---|
| ALICE         | 23                          | (−3.6; −2.6)        | $1.00 \pm 0.18(\text{stat.})^{+0.24}_{-0.26}(\text{syst.})$     |
| CMS           | 159                         | (−1.8; −2.3)        | $1.82 \pm 0.22(\text{stat.}) \pm 0.20(\text{syst.})$            |
| ALICE         | 750                         | (−4.0; −2.5)        | $2.549 \pm 0.022(\text{stat.})^{+0.209}_{-0.237}(\text{syst.})$ |

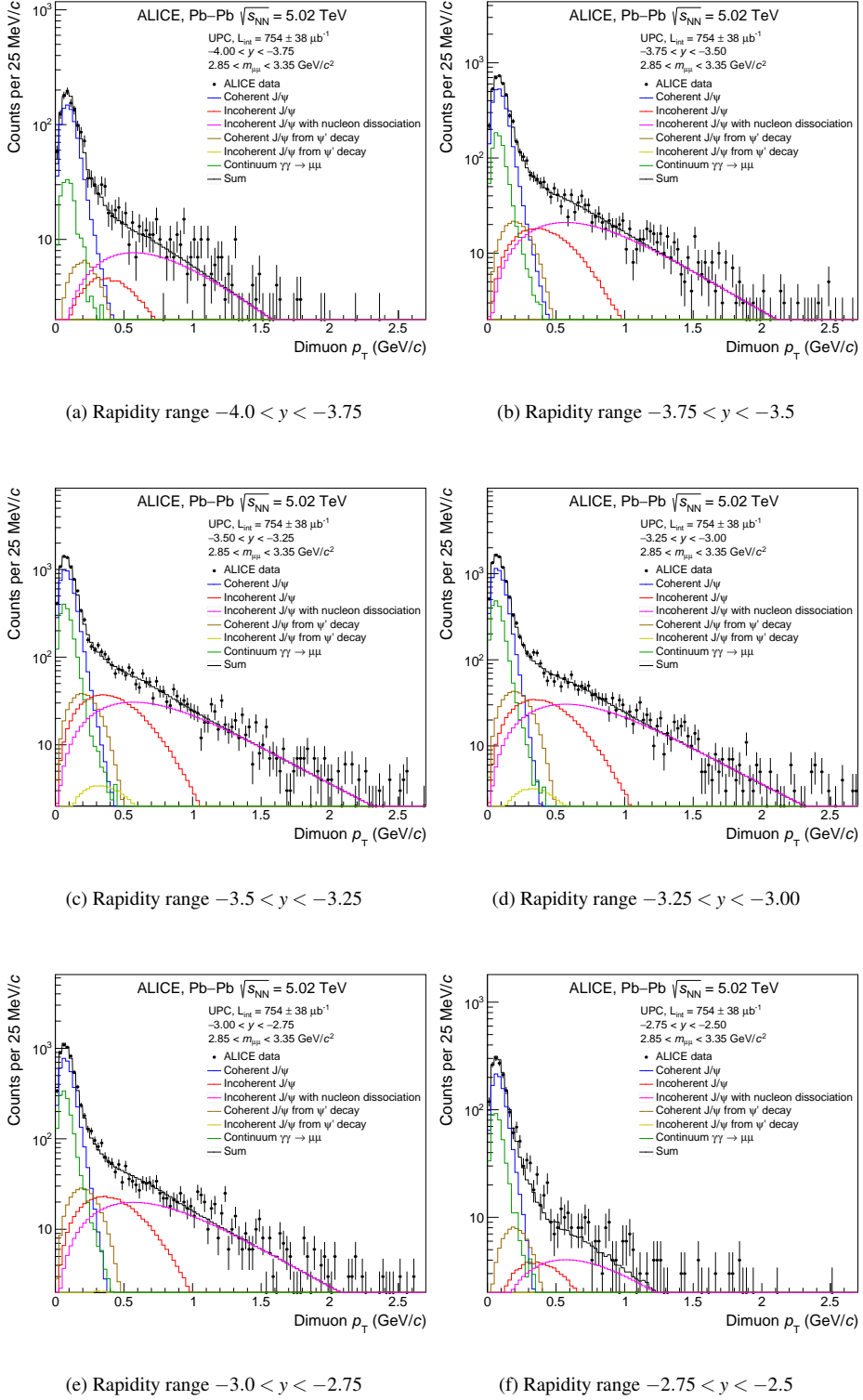


Figure 5.5: The  $p_T$  distributions for different rapidity intervals for dimuons in the range  $2.85 < m_{\mu\mu} < 3.35 \text{ GeV}/c^2$  [3].

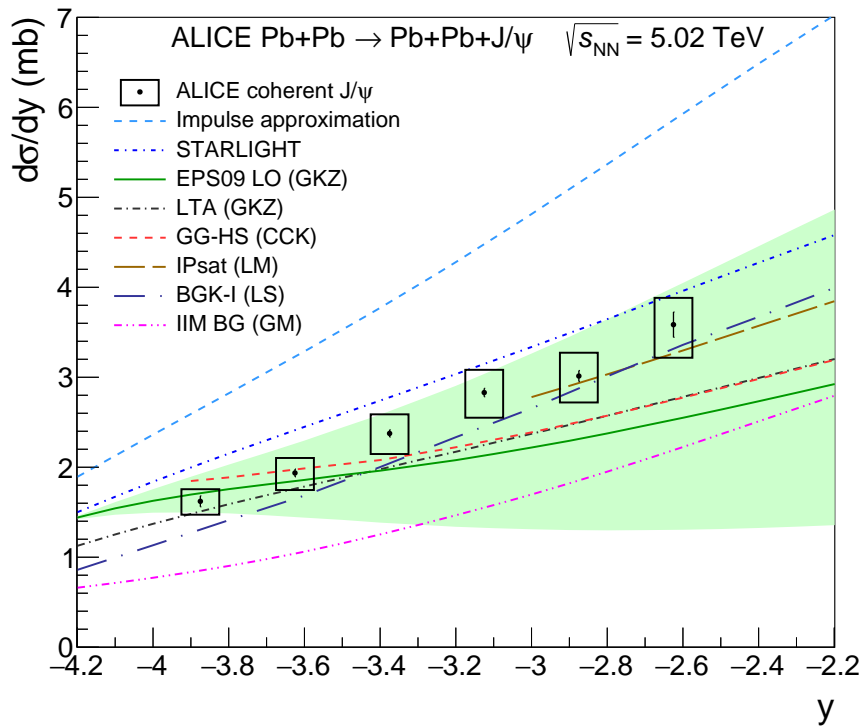


Figure 5.6: Measured coherent differential cross section of photoproduced  $J/\psi$  in ultra-peripheral collisions at  $\sqrt{s_{NN}} = 5.02$  TeV. The statistical uncertainties are represented by the error bars and the boxes around the points are the systematic errors. The colored lines represent different theoretical calculations and the green band represents the uncertainties of the EPS09 LO model [3].

# **Chapter 6**

## **Analysis**

In this chapter I present an analysis of coherently photoproduced  $J/\psi$  in UPCs with emission of forward neutrons, using data collected in 2018 during Run2 at  $\sqrt{s_{NN}} = 5.02$  TeV.

As it was mentioned before, the two ions that produced the vector meson  $J/\psi$  can undergo additional electromagnetic dissociation (EMD). During this process, one or both nuclei are excited and simultaneously with a deexcitation the nucleus (or nuclei) emits one or more neutrons in a rest frame and are boosted among the beam rapidity region. However, not only neutrons, but also pions or other charged particles can be produced. Forward neutrons are detected in ZNA and ZNC detectors and charged particles could be measured by detectors V0 or AD, however these detectors were vetoed by used trigger in the original analysis. Therefore, a correction for these lost events is needed.

My analysis is the next step of measuring  $J/\psi$  mesons in UPCs, therefore a reproduction of some of the results of the previous analysis is necessary. In this analysis I use data triggered with trigger which includes less vetoes than the one used in the original analysis. In my analysis, I go beyond the published analysis and I present the classification of the events of forward neutrons.

The first section of this chapter is dedicated to a brief description of the ALICE trigger system, data acquisition and data processing in ALICE. In next sections, I report how a vector meson  $J/\psi$  is selected from a data set, I describe the used trigger. I show the mass and  $p_T$  distributions of  $J/\psi$  for different rapidity ranges. I also describe how neutron classes are classified and I study  $p_T$  distribution for different neutron classes.

In the next chapter I discuss the correction method for the events lost due to the veto implemented in the used trigger. I present the correction factors that I have computed.

### **6.1 Trigger system, Data acquisition and data processing in ALICE**

In this section I briefly describe how the data that are used for an analysis are triggered and processed at ALICE.

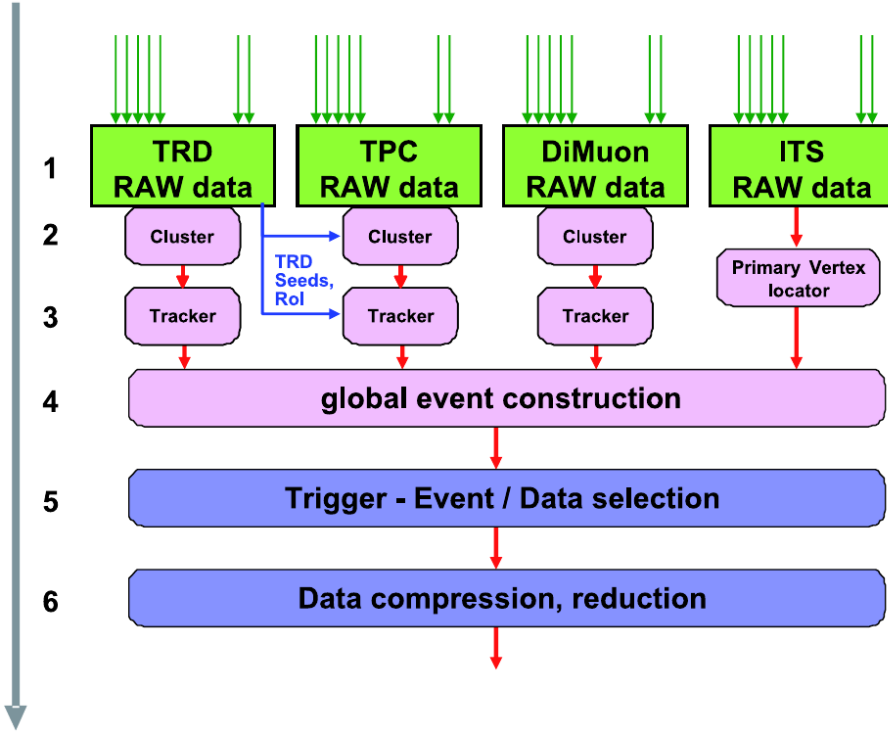


Figure 6.1: The six layers of online processing of the High Level Trigger (HLT) [13].

### 6.1.1 Trigger system and online data processing

The ALICE Central Trigger Processor (CTP) [13, 27] is designed to select events with a variety of counting rates. It is optimized to operate with different running modes: Ion–ion, proton–ion and proton–proton collisions. There are three different trigger levels: Fast Level 0 (L0) signal with a latency of  $1.2\ \mu\text{s}$ ; Level 1 (L1), which reaches the detectors at  $6.5\ \mu\text{s}$ . To protect the detector from recording events which have an overlap with other interactions before or after the one selected by the trigger, a past-future protection system has been implemented and a final Level 2 (L2) level of the trigger waits for the this past-future protection at  $88\ \mu\text{s}$  to verify that the event can be taken. The CTP outputs go to the Local Trigger Units (LTU) of each sub-detector. The data produced by sub-detectors are sent to the data acquisition (DAQ) system and, in parallel, to the High-Level Trigger system (HLT).

The data rate can exceed the maximum bandwidth of the DAQ archiving rate. Therefore the online High-Level Trigger (HLT) selects relevant events and compress the data without loosing their physics content. The HLT processing hierarchy is the following: The raw data are received, calibrated and hits and clusters are extracted. In the next step the event is reconstructed for each detector separately. After that the processed and calibrated information of all detectors is combined and the whole event is reconstructed and finally the selected data is compressed. See these architecture layers in Fig. 6.1.

### 6.1.2 Offline computing

The amount of data produced by the ALICE detector cannot be concentrated in a single computing center but many computing centers are distributed around the world. The infrastructure is coordinated by the Worldwide LHC Computing Grid (WLCG) project and it is hierarchical.

The data processing is a bit different for proton-proton and nucleus-nucleus mode. I mention the model of the second type. The raw data are written by the DAQ on a disk buffer at the CERN computing center, called Tier-0. The raw data are registered in CASTOR, partial exported to the Tier-1 (large regional computing centers, for examination of the data locally), partial first pass processing at the Tier-0 and fast processing of the data, mainly calibration, alignment, reconstruction and analysis on the CAF<sup>1</sup>.

After the data taking period, the data are read back from tapes and are fully processed. During the first pass reconstruction the first set of Event Summary Data (ESD) and Analysis Object Data (AOD) are produced. These data are ready to be analyzed. A pass reconstruction can be repeated several times. For example, the data used for analysis presented below correspond to the pass 3, which means that the calibration and reconstruction procedures have been substantially improved three times.

To optimize the use of the resources the first step of the analyses are preformed using the so-called trains. These are special jobs with high-priority that execute at the same time several different analyses (described in so-called wagons) to read only once the data. These trains are processed in the Tier-1 computing centers.

Further analysis starts from AODs produced in trains on local system with limited amount of data or the data is submitted as a job to the AliEn system, which execute on Tier-2 and Tier1 systems. For the analysis, an object-oriented offline framework AliRoot is used. It is complemented by the AliEn system that has access to the computing Grid. The AliRoot framework is also used for simulation of data. In Fig. 6.2 is shown a sketch of the reconstruction of real data and Monte Carlo simulation.

## 6.2 Data sample used in the analysis

The analysis reported in this chapter is based on data collected in year 2018 during Run 2 at the center-of-mass energy  $\sqrt{s_{NN}} = 5.02$  TeV by the ALICE experiment. In 2018 two run periods were taken and labeled LHC18q and LHC18r, where the run period LHC18q corresponds to a setup of solenoid with positive polarity and LHC18r period corresponds to a solenoid settingwith negative polarity. The data are available in:

- /alice/data/2018/LHC18q/000296510/muon\_calo\_pass3/AOD225/PWGUD/UD\_PbPb\_AOD/501\_20190723-1440
- /alice/data/2018/LHC18r/000297481/muon\_calo\_pass3/AOD225/PWGUD/UD\_PbPb\_AOD/502\_20190723-1441

The integrated luminosity for the 2018 data is  $538 \mu\text{b}^{-1}$ .

## 6.3 The triggers

For this analysis of  $J/\psi$  vector meson a trigger called CMUP6-B-NOPF-MUFAST was used. This trigger was active for all runs in the data taking periods LHC18q and

---

<sup>1</sup>CERN Analysis Facility (CAF) allows physicists to do needed analysis very quickly.

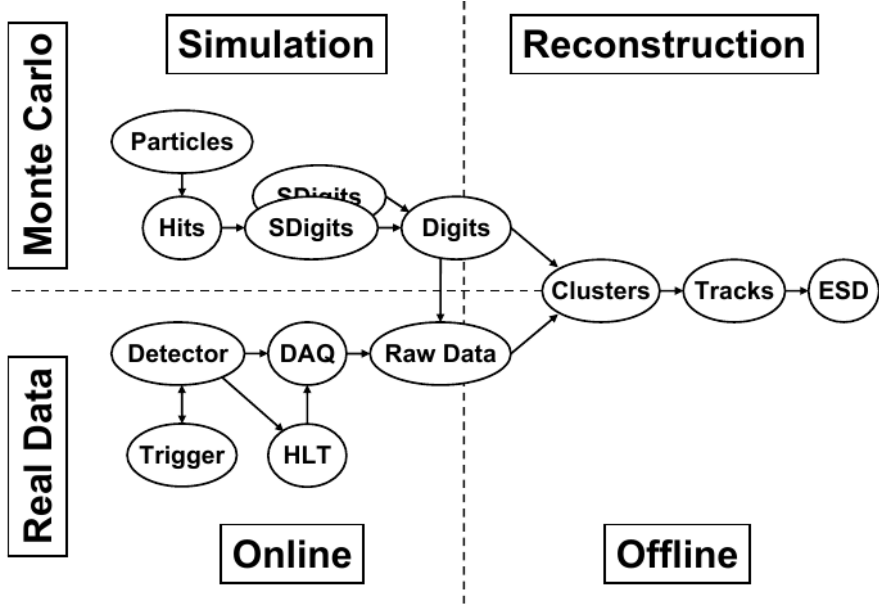


Figure 6.2: Real data processing and Monte Carlo simulation [13].

LHC18r. This trigger is defined as follows:

- CMUP6-B-NOPF-MUFAST = !0VBA&0MUL

The meaning of the trigger components are explained below:

- !0VBA: no signal in V0A with beam-beam timing
- 0MUL: low- $p_T$  unlike sign dimuon trigger
- B: bunches are expected in both beams (there are also -A,-C and -E classes, corresponding to only bunches in A beam, only in C beam or no colliding bunches expected)
- NOPF: no past-future protection applied
- MUFAST: only fast detectors related to the measurement of muons are in the readout cluster, to reduced the dead-time

The trigger fires if two unlike sign muons overcoming the low- $p_T$  threshold are detected in the muon spectrometer within a beam-beam timing. The events that fire the V0A online trigger are rejected. The low- $p_T$  trigger threshold was set to 1 GeV/c.

For the determination of the correction introduced in the next chapter I use CTRUE and C1ZED triggers:

- CTRUE-B-NOPF-CENTNOTRD = unbiased events triggered in the time window of an expected bunch crossing (BC).
- C1ZED-B-NOPF-UFAST = events triggered if at least one ZN detector fired in the time window of the expected bunch crossing.

## 6.4 Selection of events

In this section the conditions of selecting exactly two unlike sign muons in ultra-peripheral collisions are summarized.

### 6.4.1 Event preselection

The class AliAnalysisTask preselects events that fulfill the following criteria

- The event is triggered with at least one active trigger.
- Exactly one positive and one negative track is detected in the muon spectrometer.
- Information from the ZDC, V0 and AD detectors is present.

### 6.4.2 Track selection

Several requirements on each muon track are applied:

- The pseudorapidity of each track is in the range  $-4.0 < \eta_\mu < -2.5$ , so the muon can be detected by the muon spectrometer full stop.
- The radial position of each track at the entrance to the absorber is between  $17.5 < R_{abs} < 89.5$  cm to ensure that the track passes through the absorber's homogeneous region.
- Each muon detected by the muon tracking chamber is matched with the muon detected in the muon trigger chamber.
- A selection applied on the momentum multiplied by the distance of closest approach of each track to the interaction point,  $p \times DCA$  to reduce beam-induced background.

### 6.4.3 Dimuon selection

In the flowing the selection condition on each pair of muons are summarized:

- Exactly two oppositely charged muons are required.
- The dimuon rapidity should be in the interval  $-4.0 < y_{\mu\mu} < -2.5$  so that is in the spectrometer rapidity acceptance.
- The transverse momentum of the dimuon is  $p_T < 250$  MeV/c to obtain a coherent enriched sample of J/ $\psi$  candidates.
- The invariant mass of the dimuon pair is in the range  $2.85 < M_{\mu\mu} < 3.35$  GeV/c<sup>2</sup>.

After this selection we are left with the sample of J/ $\psi$  vector meson candidates.

| Cut   | Number of survivors |
|---|---------------------|
| AOD events  | 91025772            |
| Triggered events                                    | 40805581            |
| At least one track                                  | 18292740            |
| Two good muon tracks                                | 85122               |
| Good runs   | 84184               |
| CMUP6 trigger                                       | 84184               |
| Rapidity $-4.0 < y_{\mu\mu} < -2.5$                 | 84184               |
| Mass cut $2.85 < M_{\mu\mu} < 3.35 \text{ GeV}/c^2$ | 48234               |
| Cut $p_T > 0.25 \text{ GeV}/c$                      | 25662               |

Table 6.1: Table of events that survived each cut in the preselection and selection of the data used for the analysis.

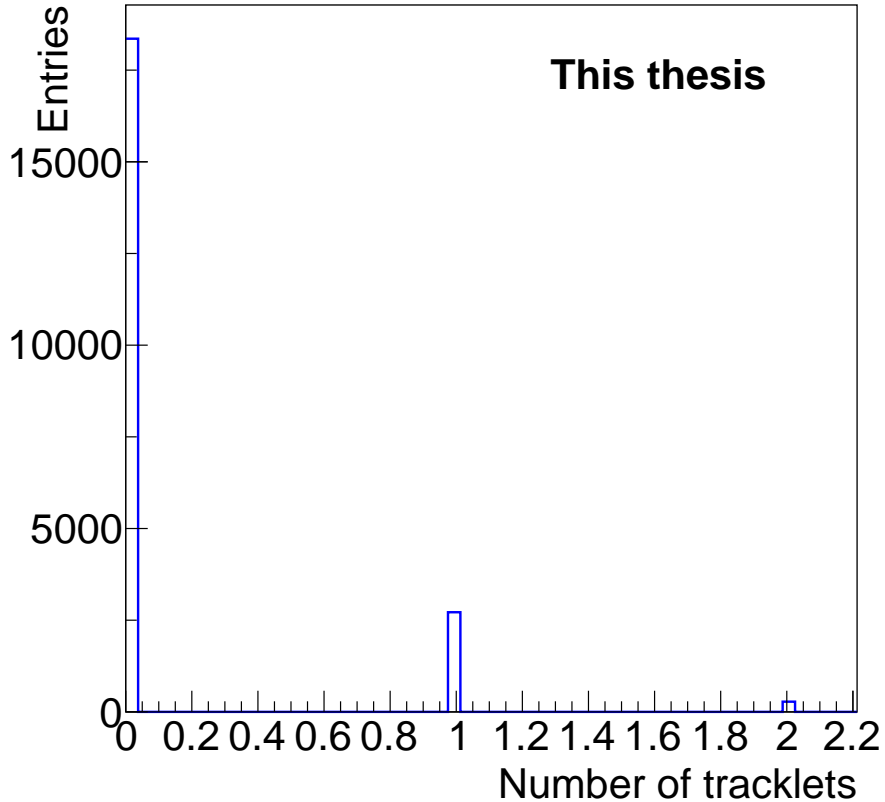


Figure 6.3: The number of tracklets after all cuts applied.

#### 6.4.4 Selection and control plots

The number of AOD events recorded in good runs in the data taking periods LHC18q and LHC18r is 91025772. The number of events after each one of the selection criteria

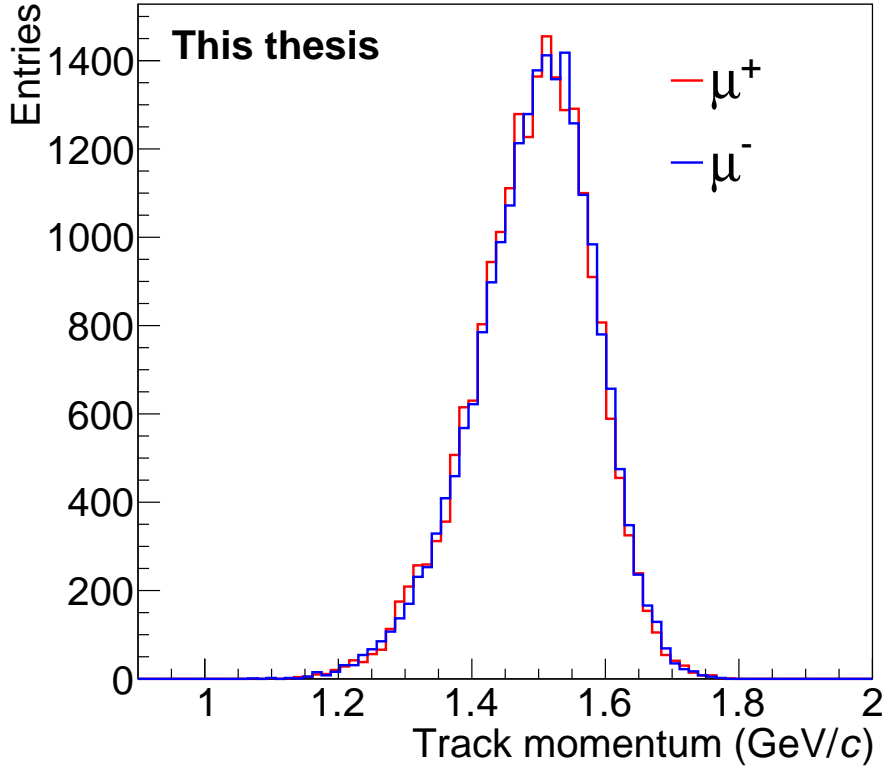


Figure 6.4: Momentum of  $\mu_+$  and  $\mu_-$  tracks after all cuts applied.

is shown in Tab. 6.1. The final number of events after all selection criteria is 25662.

The number of tracklets found in the sample after the  $J/\psi$  selection was applied is shown in Fig. 6.3. Most of the events have zero tracklets. In next two figures I show control plots of muon tracks momentum and azimuth angle distributions. The transverse momentum of each track was required to be above  $1 \text{ GeV}/c$  threshold, in Fig. 6.4 the momentum distributions of oppositely charged muons are shown and Fig. 6.5 shows the azimuth angle distributions.

## 6.5 ZDC neutron classes

This thesis is focused on the  $J/\psi$  photoproduction with an additional neutron emission, therefore, the selected data sample is divided into four ZDC classes. These classes are classified in dependence on emission of neutron(s) caused by an independent EMD process occurring right after the photoproduction of the vector meson  $J/\psi$  with the same nuclei. The produced neutrons are boosted in beam direction and its detection is provided by ZNA and ZNC calorimeters, described in the Chapter 3. Using the time information we can estimate very precisely if there is at least one neutron detected in the ZNA or ZNC. The selection criteria on ZN time is that the time has to be within

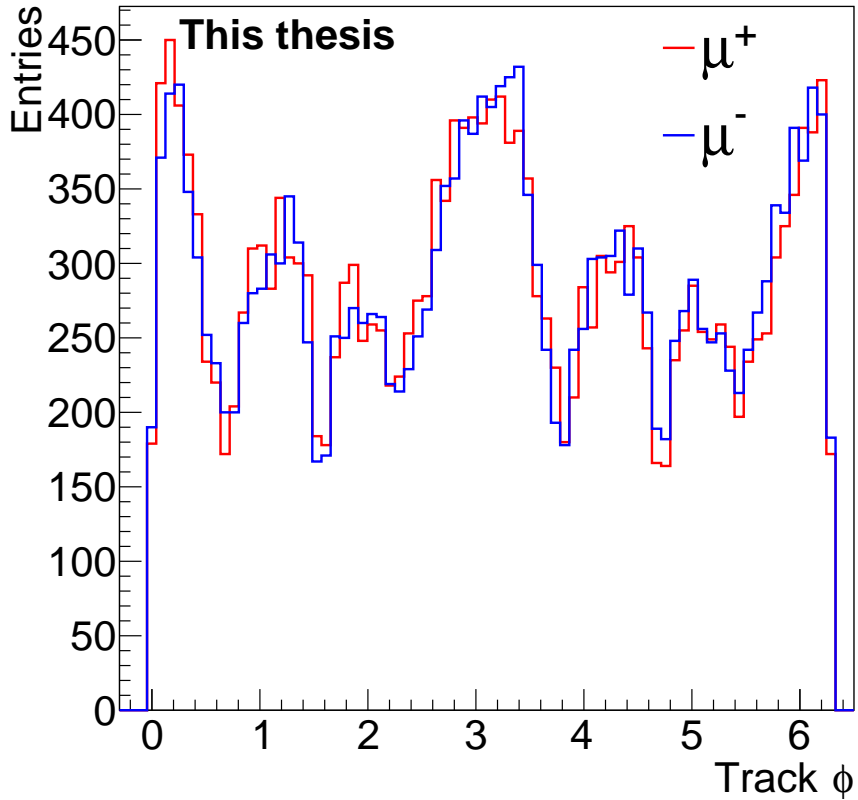
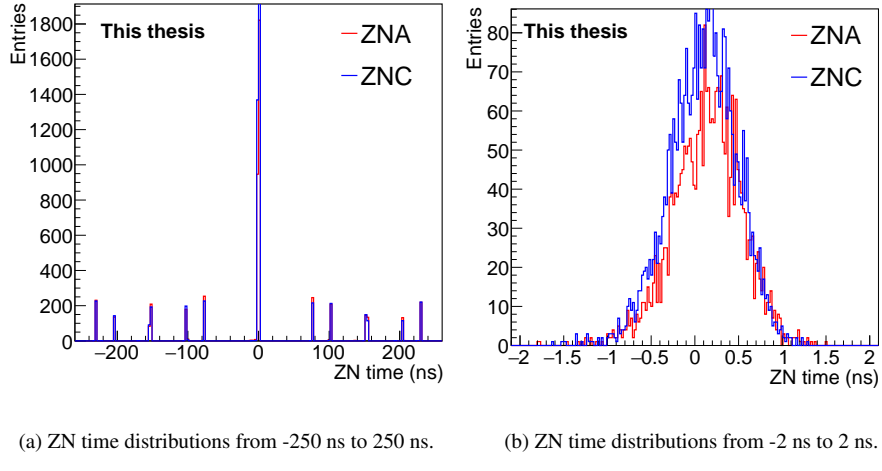


Figure 6.5: Azimuth angle distribution of  $\mu_+$  and  $\mu_-$  tracks after all tracks applied.

$\pm 2$  ns window to ensure that the neutron(s) is produced in the appropriate collision. Figure 6.6a shows the time of ZNA and ZNC detectors in range from -250 ns to 250 ns to see the other bunch crossings. In Fig. 6.6b the ZNA and ZNC time within 2 ns is shown.

Characterization of each ZDC class is listed below:

- (0n0n) - events without any additional EMD interaction: ZNA and ZNC detectors are empty.
- (XnXn) - events when both interacting nuclei undergo EMD: one or more neutrons detected in both sides of ZDC detector.
- (0nXn) - events with single nucleus EMD: empty ZNA and at least one neutron in ZNC.
- (Xn0n) - events with single nucleus EMD: at least one neutron in ZNA and none in ZNC.



(a) ZN time distributions from  $-250 \text{ ns}$  to  $250 \text{ ns}$ .

(b) ZN time distributions from  $-2 \text{ ns}$  to  $2 \text{ ns}$ .

Figure 6.6: ZNA (red line) and ZNC (blue line) time distributions of events after all cuts applied in two different ranges. The left one ranges  $-250 < t < 250 \text{ ns}$  to see the other bunch crossings and the right shows the focused time on  $-2.0 < t < 2.0 \text{ ns}$ .

### 6.5.1 Energy deposit in ZNA and ZNC detectors

Using the ZNA and ZNC TowerEnergy the deposit of energy in ZNA and ZNC calorimeters is obtained. The energy deposition in ZDC detector for events after all selections described above is shown in Fig. 6.76.8 for both sides of the ZDC. The data are fitted by Gaussian function and the mean value of the peaks is extracted. The first two peaks correspond to emission of one and two neutrons and the peak values are consistent with our expectations.

## 6.6 The invariant mass distribution

The raw invariant mass spectrum of the selected  $J/\psi$  candidates can be seen in Fig. 6.9. The yield of coherent  $J/\psi$  candidates dominates for the transverse momentum  $p_T < 0.25 \text{ GeV}/c$ , therefore this value is used as the  $p_T$  cut. The  $J/\psi$  and  $\Psi'$  peaks were fitted with a Crystal Ball function and the background with an exponential function.

In the fit, the mass parameter for the  $J/\psi$  was left free but the mass of the  $\Psi'$  was fixed to the  $J/\psi$  mass as  $m_{\Psi'} = m_{\psi} + 3.686097 - 3.096900$  where last two values are the  $\Psi'$  and  $J/\psi$  masses, respectively, taken from PDG [28]. The  $J/\psi$  background continuum is fitted using a template made from reconstructed STARlight events corresponding to the  $\gamma\gamma \rightarrow \mu^+\mu^-$  process. It is described with a polynomial of a fourth order turning into an exponential tail at large invariant masses.

The raw  $J/\psi$  yields used in the analysis were extracted from the mass fits of invariant mass distributions of each ZDC class. The corresponding fits with the  $J/\psi$  yields are shown in Fig. 6.10. I point out that into the extracted  $J/\psi$  yields contribute both coherent and incoherent productions as well as a feed-down contribution. The feed-down and incoherent contribution is described in next sections.

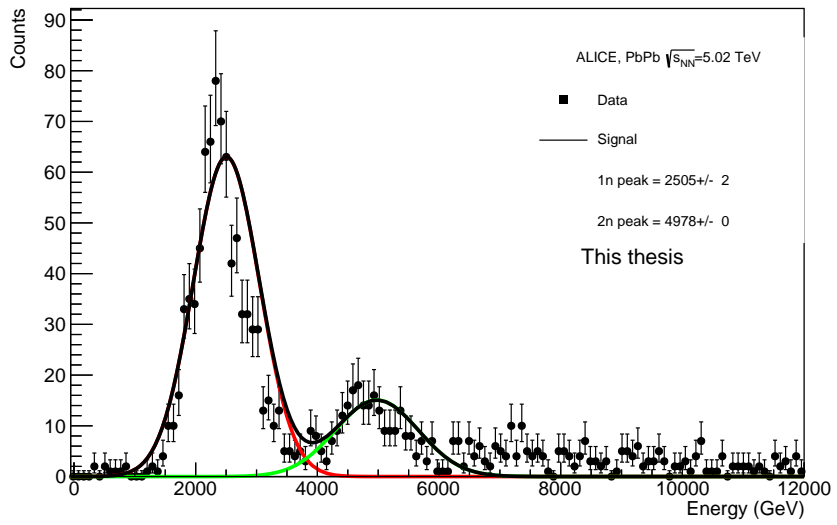


Figure 6.7: ZNA energy deposit distribution of selected events. The first two peaks are fitted by the Gaussian function. The extracted mean values are in good agreement with our expectations.

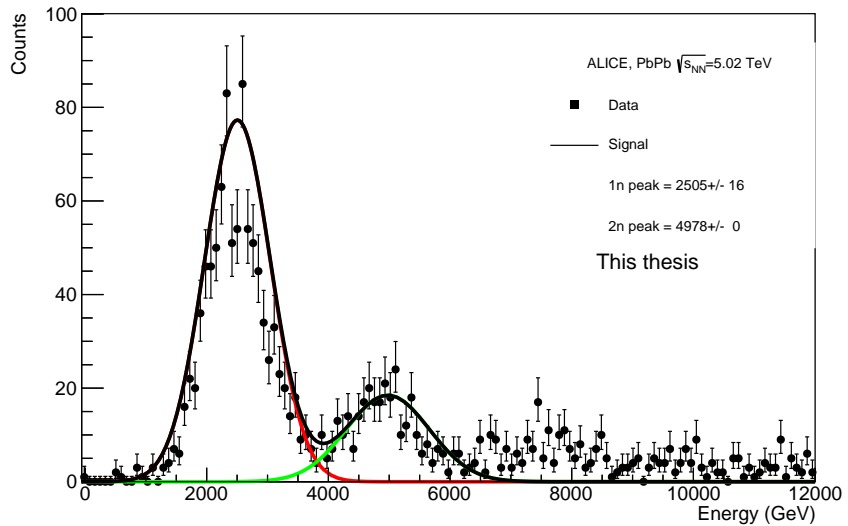


Figure 6.8: ZNC energy deposit distribution of selected events. The first two peaks are fitted by the Gaussian function. The extracted mean values are in good agreement with our expectations.

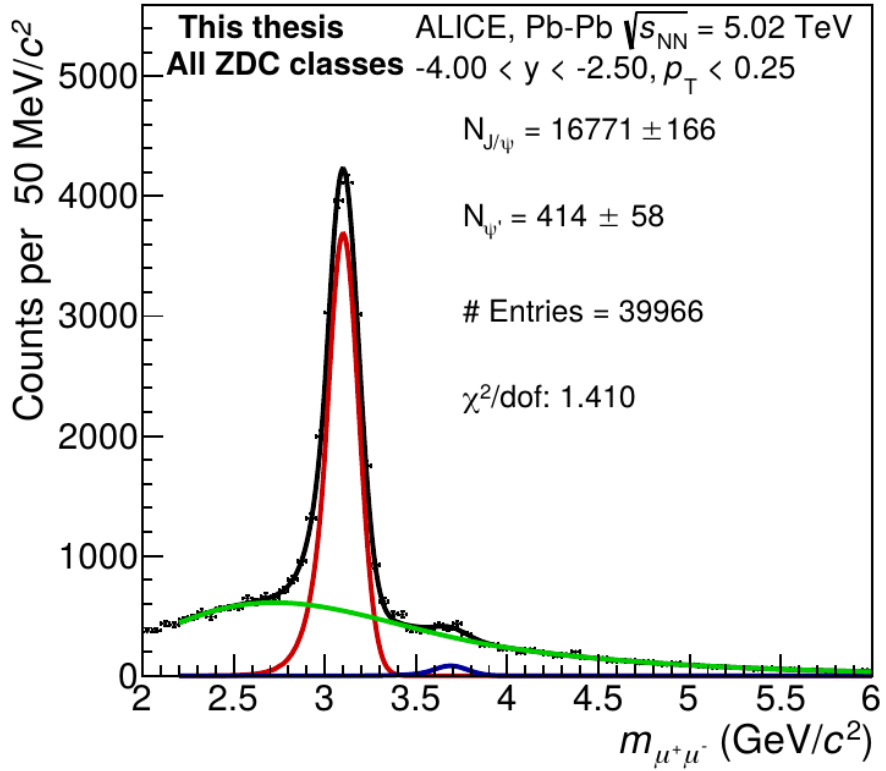


Figure 6.9: Invariant mass distribution of dimuon pairs in the full rapidity range  $-4 < y_{2.5}$  satisfying all cuts described above. The green line represents the background. The red and blue line corresponds to Crystal Ball functions representing  $J/\psi$  and  $\Psi'$  signals, respectively.

### 6.6.1 Feed-down contribution

To the raw  $J/\psi$  yield contributes process  $\Psi' \rightarrow J/\psi + \text{anything}$ . The ratio of feed-down and primary  $J/\psi$  is computed as

$$f_D = \frac{N(\text{feed-down } J/\psi)}{N(\text{primary } J/\psi)} = R \frac{\epsilon(\Psi' \rightarrow J/\psi) BR(\Psi' \rightarrow J/\psi)}{\epsilon(J/\psi)}, \quad (6.1)$$

where  $\epsilon(\Psi' \rightarrow J/\psi) = 7.2\%$ ,  $BR(\Psi' \rightarrow J/\psi) = 0.8 \pm 0.06\%$ ,  $\epsilon(J/\psi) = 12.0\%$  and  $R = 0.15 \pm 0.02$  is the ratio of the  $\Psi'$  and  $J/\psi$  cross sections. All the values used for the feed-down calculation are taken from [3]. Feed-down parameter obtained from Eq. 6.1 is  $f_D = 5.5 \pm 0.7\%$ .

## 6.7 Transverse momentum distribution

The transverse momentum spectrum was described by data simulated with STARlight. The MC generator produced events from different processes: coherent and incoherent

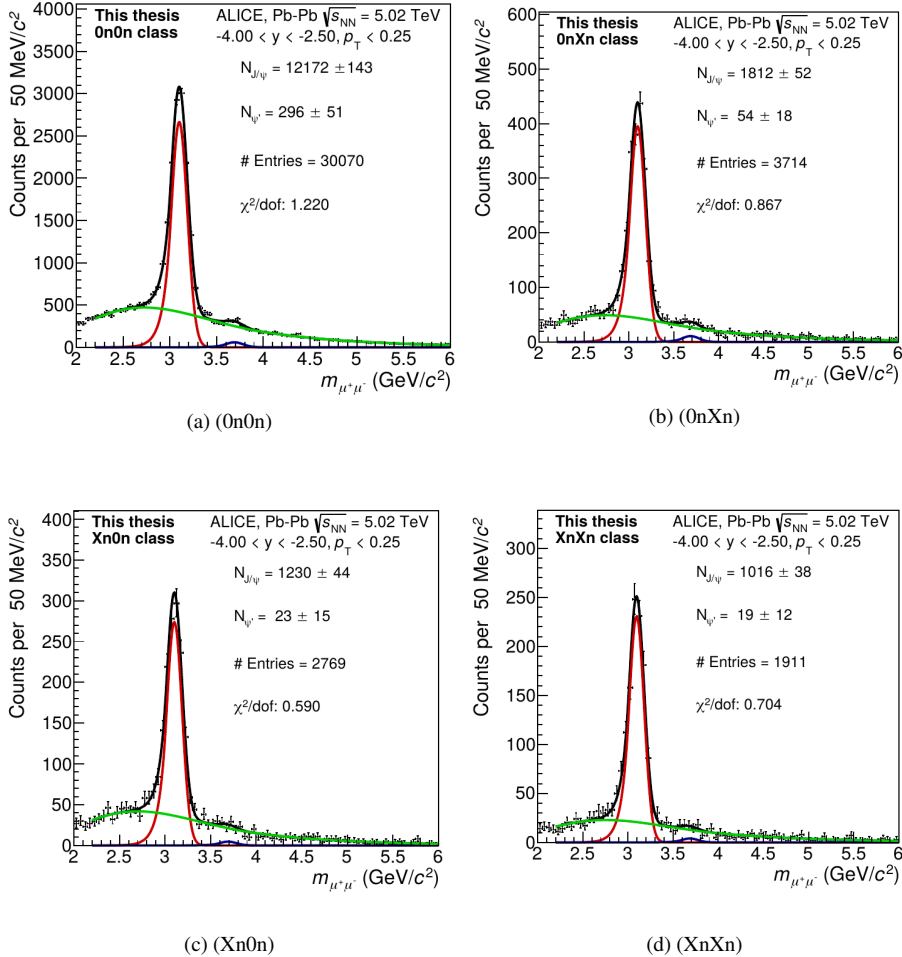


Figure 6.10: Invariant mass distributions fitted with the Crystal Ball function for selected  $J/\psi$  events with  $p_T < 0.25$  GeV/ $c$  in different ZDC classes.

$J/\psi$  photoproduction, coherent and incoherent feed-down  $\Psi' \rightarrow J/\psi$  and  $\gamma\gamma \rightarrow \mu\mu$  process. Also incoherent  $J/\psi$  production with nucleon dissociation contributes, however cannot be modeled with the STARlight, therefore a parameterization from the H1 collaboration as in the discussed paper [3] was used to describe it.

Studying of the contributing processes is important for obtaining of amount of incoherent contribution in the data sample and Fig. 6.11 shows the  $p_T$  spectrum that is fitted a model consisting of a sum of MC templates described above. The different contributions are also shown in the figure.

Transverse momentum spectra in different ZDC classes are shown in Fig. 6.12.

### 6.7.1 Incoherent contribution

The number of  $J/\psi$  events extracted from the mass fit. However within the  $J/\psi$   $p_T$  range there is also a contribution of  $J/\psi$  candidates which have been produced inco-

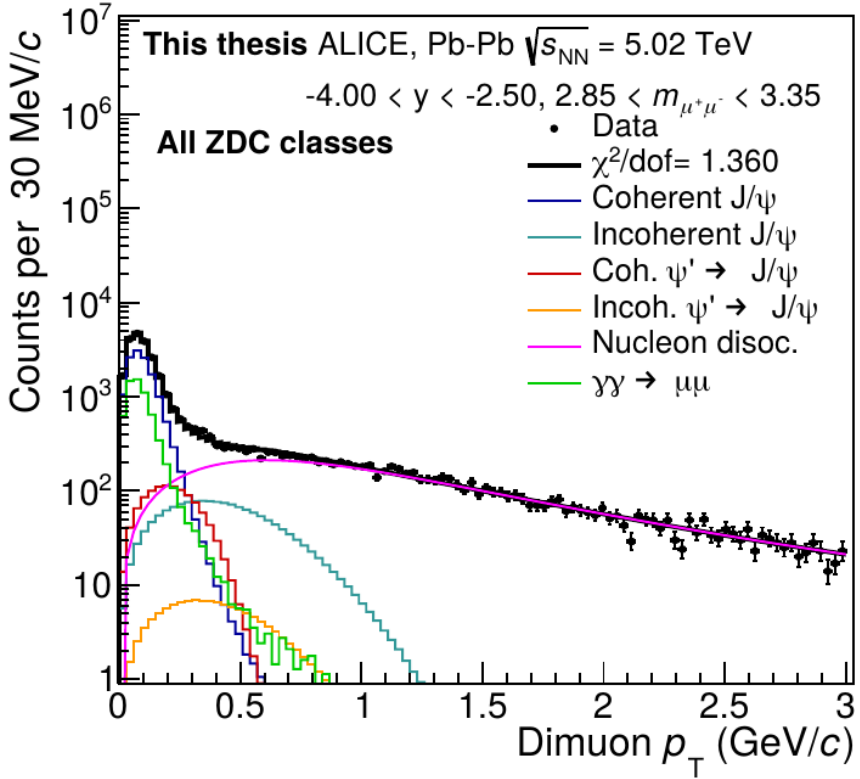


Figure 6.11: Transverse momentum distribution of events satisfying all cuts described above and fitted with a model consisting of a sum of the templates based on MC data set described in the text. Each process contributing to the final model is also shown in the figure.

herently. The incoherent events are not studied in this analysis, therefore they had to be subtracted.

Studying the  $p_T$  distributions and fitting them with Monte Carlo templates serves us to extract the ratio of incoherent and coherent events as

$$f_I = \frac{J/\psi_{\text{incoh}} + \text{feed down } J/\psi_{\text{incoh}} + \text{dissociative } J/\psi_{\text{incoh}}}{J/\psi_{\text{coh}} + \text{feed down } J/\psi_{\text{coh}}}, \quad (6.2)$$

for events satisfying  $p_T < 0.25 \text{ GeV}/c$ .

The fits presented in the section above are very preliminary since it was not the main aim of this thesis. I compared obtained  $f_I$  values with Ing. Tomáš Herman, a PHD student, who has worked on these fits very intensively recently<sup>2</sup>, and the difference of values was included in the systematic error. It can be noticed that the systematic error in (0nXn) ZDC class is very large, it is due to a big difference in my and Ing. Herman value. The  $p_T$  fit needs to be study in more detail to get consistent values. Nevertheless, the obtained values are used for a calculation of  $J/\psi$  photoproduction cross section, so a large systematic error for the (0nXn) is expected.

<sup>2</sup>His recent talk on this topic can be found here [29].

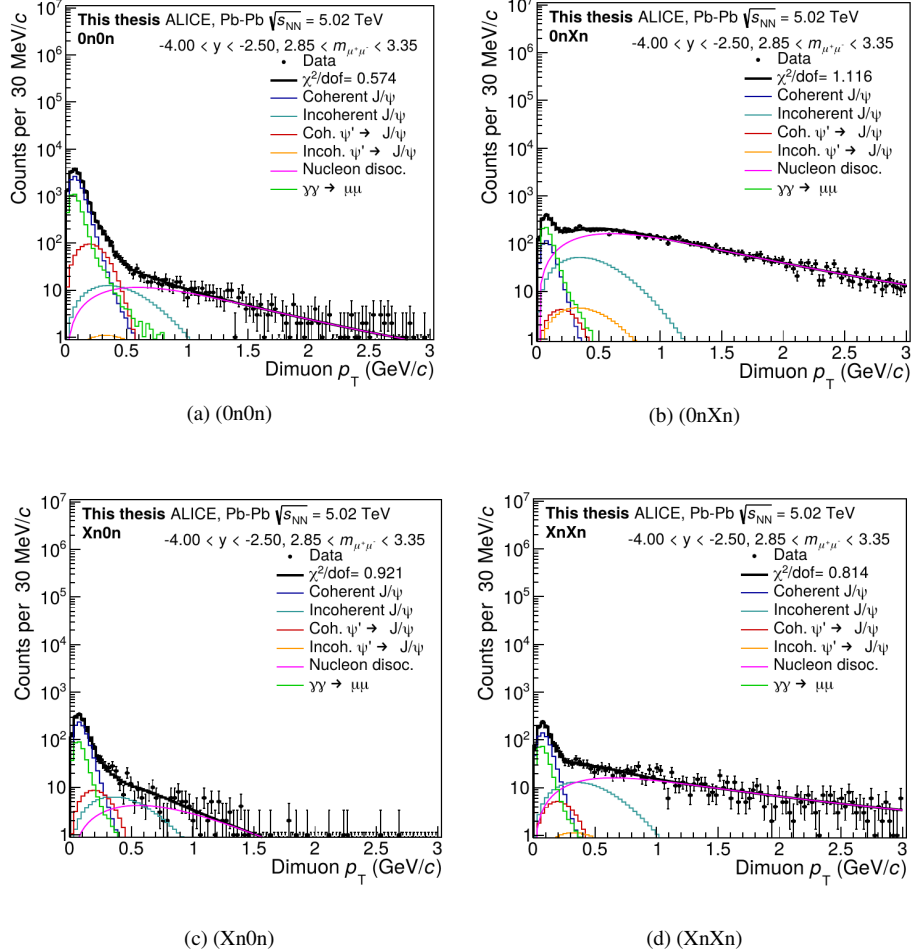


Figure 6.12: Transverse momentum distributions in different ZDC classes fitted with a model consisting of a sum of the templates based on MC data set described in the text.

| ZDC class   | $f_1$   |
|-------------|---|
| All classes | $0.063 \pm 0.001$ (stat.) $\pm 0.8\%$ (syst.) |
| (0n0n)      | $0.008 \pm 0.001$ (stat.) $\pm 0.6\%$ (syst.) |
| (0nXn)      | $1.407 \pm 0.149$ (stat.) $\pm 83\%$ (syst.)  |
| (Xn0n)      | $0.041 \pm 0.006$ (stat.) $\pm 1.6\%$ (syst.) |
| (XnXn)      | $0.173 \pm 0.015$ (stat.) $\pm 7.4\%$ (syst.) |

Table 6.2:  $f_1$  fractions for different ZDC classes calculated with 6.2 from  $p_T$  fits.

# Chapter 7

## Corrections

This chapter is dedicated to studying and measuring possible corrections that should be used when a cross section of forward  $J/\psi$  photoproduction in UPC is measured with ALICE detector.

Now, I would like to go back a little bit and remind here where the need for a correction comes from and why the correction is so important. In the published analysis discussed in section 5.2 the main used trigger included vetoes implemented with ADA, ADC and V0A triggers and more than that, additional offline vetoes were applied. In case of an event with a subsequent EMD process with production of charged particles, the event is uncompromisingly lost. During the data taking periods was no control trigger available that would allow the correction for the lost events.

To deal with this issue, another trigger, that was active in 2018 data taking, could be used for the analysis; CMUP6. With this trigger and separation of the selected data sample into ZDC classes, see Chap. 6, a solution was found. Because implemented veto is only on the A-side of the detector, ZDC classes (0n0n) and (0nXn) don't need any correction because there are not expected possible particles triggering the veto. Only ZDC classes (Xn0n) and (XnXn) need a correction and its determination is described in this chapter.

The veto implemented with the V0A trigger causes a chance that some events will be lost. There are two reasons why it is so.

- An interaction of pair of bunches different from the pair that creates the  $J/\psi$  vector meson can cause a signal in the V0A. This process is called pile-up.
- The pair of nuclei that produced the  $J/\psi$  vector meson can undergo an independent electromagnetic interaction. One of the nuclei can be excited with enough energy to produce charge particles which may leave a signal in the V0A. Such interaction is called electromagnetic dissociation (EMD).

Fig. 7.1 shows the coherent data sample in ZDC class (Xn0n), demonstrating a situation of the detected and lost events due to the V0A veto. Signal recorded in offline V0A decision (green circle) is contaminated with pile-up events and these events need to be subtracted. The gray ellipse demonstrates the events that were vetoed with the online trigger.

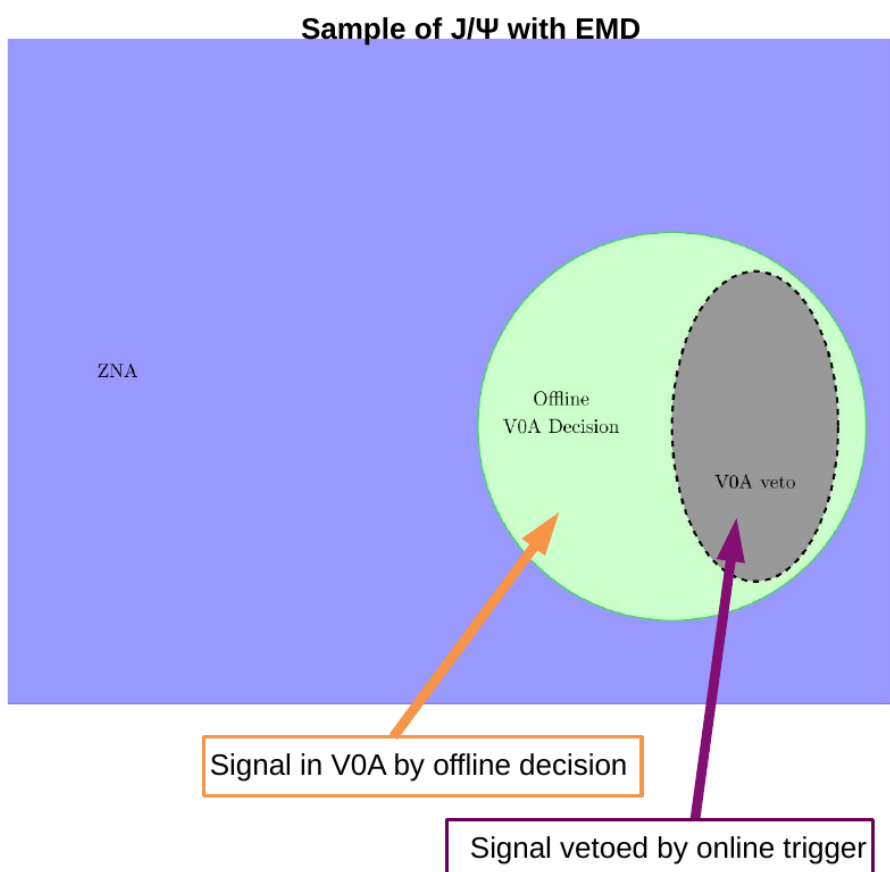


Figure 7.1: Coherent data sample in ZDC class (Xn0n), blue shows signal in ZNA, green shows signal in the offline V0ADecision and gray ellipse represents vents lost due to V0A veto.

## 7.1 Determination of pile-up events

The amount of events caused by pile-up is determined using the CTRUE events. These events are triggered on the timing of bunch crossings, unbiased with respect to the possible interaction.

There are two available information from the V0A detector. One is a signal obtained from online trigger 0VBA. If one requires no signal at the trigger level, the condition used is !0VBA. The second available information about the activity in V0A detector is the offline decision, called V0ADecision. The meaning of the decisions is the following:

- V0ADecision is kEmpty: the detector is empty.
- V0ADecision is kB: the detector has a signal in the beam-beam time window.

The V0A trigger has not 100% efficiency which means that there were events that the V0A trigger "missed" and they had the V0ADecision kB. And this V0A offline signal can be contaminated with pile-up events. Coherent J/ $\psi$  photoproduction it is expected to detect only the vector meson and nothing else, thereby one computes the probability of having a V0ADecision kB and no 0VBA as ratio:

$$P = \frac{\text{V0ADecision is kB \&& empty detector}}{\text{empty detector}}. \quad (7.1)$$

The definition of empty detector varies for different ZDC classes and the requirements are listed below:

- No activity in ZNA, neither ZNC detector.
- No V0C decision signal on offline level.
- No signals in ADA and ADC decisions.
- No tracklets.
- No signal in 0VBA.

The fraction is plotted in dependence on the average number of inelastic interaction for bunch crossing  $\mu$ , run by run. To obtain the systematic uncertainty I varied the requirements on empty detector. To variate the conditions on empty detector, first I did not consider the requirement on no signal in the ADA and ADC detector and secondly I did not implement condition on having no tracklets. The corresponding ratios are shown in Fig. 7.2. A value of  $\epsilon_{PU}$  is obtained as one minus the weighted average of the plotted points in the figure.

The resulting value is taken to be a mean of values obtained from varying conditions of "empty detector". The largest spread of the values was used as an systematic error.

$$\epsilon_{PU} = 97.65 + 0.05 - 0.07\%$$

This value is used in the section 7.3 to determine how many events in V0A are caused by pile-up.

| Neutron class | $\varepsilon_1$    | $\varepsilon_2$     | $\varepsilon_3$    |
|---------------|--------------------|---------------------|--------------------|
| (Xn0n)        | $51.94 \pm 0.29\%$ | $44.45 \pm 0.26\%$  | $49.41 \pm 0.26\%$ |
| (XnXn)        | $48.46 \pm 0.10\%$ | $0.4015 \pm 0.84\%$ | $37.75 \pm 0.78\%$ |

Table 7.1: Table of variations of empty event definition in determination of inefficiency of V0A trigger obtained from Eq. 7.2 using C1ZED data sample.

## 7.2 Determination of correction for events lost due to EMD processes

The pair of nuclei that produced the  $J/\psi$  vector meson can interact via EMD. One of the nuclei can be excited with enough energy to produce charge particles which leave signal in V0 and AD detectors. Due to the veto implemented with V0A trigger some of such events are vetoed. As mentioned above, this trigger was not 100% efficient. This gave us the possibility of computing the fraction of good events rejected by the V0A veto at the trigger level in similar way as in determination of pile-up.

The efficiency of the V0A trigger is determined using the C1ZED events which is triggered by a signal in the ZNA or ZNC detectors in bunch crossing time window. Ratios, using the Eg. 7.2, were formed.

$$P = \frac{\text{V0ADecision is kBB \&& !VBA \&& Empty detector}}{\text{V0ADecision is kBB \&& Empty detector}} \quad (7.2)$$

with definition of empty detector explained below:

### (Xn0n)

- Signal in ZNA.
- No signal in ZNC.
- No signals in the ADC and V0C decisions.
- No activity in ADA decision.
- No tracklets.

### (XnXn)

- Signal in ZNA and ZNC.
- No signal in ADA and ADC decisions.
- No tracklets.

The requirements on empty detector were varied, such as there is no requirements on signal in AD detectors ( $\varepsilon_2$ ) or no condition on tracklets ( $\varepsilon_3$ ) was applied. The corresponding ratios are shown in Fig. 7.3 and Fig. 7.4. The results are summarized in the Tab. 7.1 and the mean of the values was taken as a result and the largest spread as the systematic uncertainty.

$$\varepsilon(Xn0n) = 48.6 + 3.6 - 4.4\%,$$

$$\varepsilon(XnXn) = 42.1 + 7.4 - 5.1\%.$$

To correct for the EMD events that are lost due to V0A trigger inefficiency we multiply the number of events with V0A decision kBB by factor  $\frac{1}{\varepsilon}$ .

### 7.3 Procedure of the correction factors calculation

In this section I present the procedure of the calculations of the correction factor for classes (Xn0n) and (XnXn), the correction of pile-up and V0A veto is computed using the values determined in two previous sections.

In general the correction factor is defined as

$$F = \frac{N_{J/\psi}^{\text{corrected}}}{N_{J/\psi}}, \quad (7.3)$$

where  $N_{J/\psi}^{\text{corrected}}$  is the number of events of  $J/\psi$  candidates after the correction for the events caused by pile-up and the events lost due to the veto implemented with the V0A trigger,  $N_{J/\psi}$  is the number of events before the correction. Since the correction includes two steps, pile-up and V0A veto corrections, I divide the data sample into two parts. One part consists of events with V0A decision kEmpty ( $N_{\text{noV0A}}$ ) and this part is corrected only for pile-up. The second part are events with V0A decision kBB ( $N_{\text{V0A}}$ ). These events are corrected for the pile-up and then corrected for the events lost due to the veto. The number of corrected events is written as

$$N_{J/\psi}^{\text{corrected}} = N_{\text{noV0A}}^{\text{PUcorrected}} + N_{\text{V0A}}^{\text{PU+vetcorrected}}, \quad (7.4)$$

where  $N_{\text{noV0A}}^{\text{PUcorrected}}$  is the number of  $J/\psi$  mesons with V0A decision kEmpty corrected for the pile-up and  $N_{\text{V0A}}^{\text{PU+vetcorrected}}$  is the number of produced  $J/\psi$  with V0A decision kBB corrected for the pile-up and for the events lost due to the V0A veto described above.

Since the correction factor is a fraction, I use number of events including the incoherent contribution and background for the calculations. In next two sections I describe the pile-up and veto efficiency corrections for two ZDC classes, (Xn0n) and (XnXn).

In the section 7.4 of this chapter I summarize the results of obtained correction factors for considering ZDC classes. I also show a table referring to each step of the correction procedure. In the very last section of this chapter I present a computation of a cross section of the  $J/\psi$  photoproduction in different ZDC classes using calculated correction factors  $F$ .

#### 7.3.1 Pile-up correction

The amount of pile-up events is determined and then subtracted from the sample, using the correction factors presented in section 7.1, such as:

$$N_{\text{PU}} = N_{J/\psi} \cdot (1 - \varepsilon_{\text{PU}}). \quad (7.5)$$

Correction for the pile-up needs to be done for both parts described above. Firstly, the number of the pile-up events is computed with the Eq. 7.5. Then the amount of pile-up is subtracted from the sample of  $J/\psi$  candidates. See the computation below for both (Xn0n) and (XnXn) classes.

### (Xn0n)

- Determination of events caused by pile-up:

$$N_{\text{noV0A}}^{\text{PU}} = 1429 * (1 - 0.97653) = 33.5386,$$

$$N_{\text{V0A}}^{\text{PU}} = 128 * (1 - 0.97653) = 3.00416$$

- Subtracting the pile-up events:

$$N_{\text{noV0A}}^{\text{PUcorrected}} = 1429 - 33.5386 = 1395.46,$$

$$N_{\text{V0A}}^{\text{PUcorrected}} = 128 - 3.00416 = 124.996$$

### (XnXn)

- Determination of events caused by pile-up:

$$N_{\text{noV0A}}^{\text{PU}} = 1029 * (1 - 0.97653) = 24.1506,$$

$$N_{\text{V0A}}^{\text{PU}} = 176 * (1 - 0.97653) = 4.13072$$

- Subtracting the pile-up events:

$$N_{\text{noV0A}}^{\text{PUcorrected}} = 1029 - 24.1506 = 1004.85,$$

$$N_{\text{V0A}}^{\text{PUcorrected}} = 176 - 4.13072 = 171.869$$

These number of events refers to number of  $J/\psi$  candidates after subtraction of events caused by pile-up.

### 7.3.2 Correction for V0A trigger veto

Thereafter, the number of events corrected from pile-up and having V0A decision kBB ( $N_{\text{V0A}}^{\text{PUcorrected}}$ ) needs to be corrected for events vetoed with V0A veto trigger. The correction is computed as

$$N_{\text{V0A}}^{\text{PU+vetcorrected}} = N_{\text{V0A}}^{\text{PUcorrected}} \cdot \frac{1}{\varepsilon}, \quad (7.6)$$

where  $\varepsilon$  is the correction factor determined in section 7.2. The computation is shown below.

### (Xn0n)

- Correction of events lost due to the V0A veto:

$$N_{\text{V0A}}^{\text{PU+vetcorrected}} = 124.996 / (0.486) = 257.193$$

### (XnXn)

- Correction of events lost due to the V0A veto:

$$N_{\text{V0A}}^{\text{PU+vetcorrected}} = 171.869 / (0.4212) = 408.047$$

| Step of correction                          | (Xn0n)                    | (XnXn)                    | all                       |
|---|---------------------------|---------------------------|---------------------------|
| $N_{\text{noV0A}}$                          | 1429                      | 1029                      |                           |
| $N_{\text{V0A}}$                            | 128                       | 176                       |                           |
| $N_{\text{noV0A}}^{\text{PUcorrected}}$     | 1395.46                   | 1004.85                   |                           |
| $N_{\text{V0A}}^{\text{PUcorrected}}$       | 124.996                   | 171.869                   |                           |
| $N_{\text{V0A}}^{\text{PU+veto corrected}}$ | 257.193                   | 408.047                   |                           |
| $N_{\text{J}/\psi}^{\text{corrected}}$      | 1652.65                   | 1412.9                    |                           |
| $F$   | $1.061^{+1.6\%}_{-2.2\%}$ | $1.182^{+1.4\%}_{-1.6\%}$ | $1.015^{+0.2\%}_{-0.2\%}$ |

Table 7.2: Table of number of events after each step of correction described in the text. First for pile-up, secondly for V0A veto losses. The correction factors computed for ZDC classes (Xn0n) and (XnXn) are presented with its statistic and systematic uncertainties.

## 7.4 Results

Once all corrections of number of events are done, corrected number of events is obtained from Eq. 7.4 and the correction factors for ZDC classes are computed using the Eq. 7.3. Results obtained from each step of the correction are summarized in the Tab. 7.2. The procedure was repeated for systematic errors from pile-up and V0A veto sources described above.

- Correction factor:

$$F_{(\text{Xn0n})} = \frac{N_{\text{J}/\psi}^{\text{corrected}}}{N_{\text{J}/\psi}} = \frac{N_{\text{noV0A}}^{\text{PUcorrected}} + N_{\text{V0A}}^{\text{PUcorrected}}}{N_{\text{J}/\psi}} \frac{257.193 + 1395.46}{(1557)} = 1.061,$$

$$F_{(\text{XnXn})} = \frac{408.047 + 1004.85}{(1195)} = 1.182,$$

$$F_{(\text{all})} = \frac{15965 + 2197 + 1652.65 + 1412.9}{(15965 + 2197 + 1557 + 1195)} = 1.015.$$

Finally, the differential cross section for coherent  $\text{J}/\psi$  photoproduction can be computed as

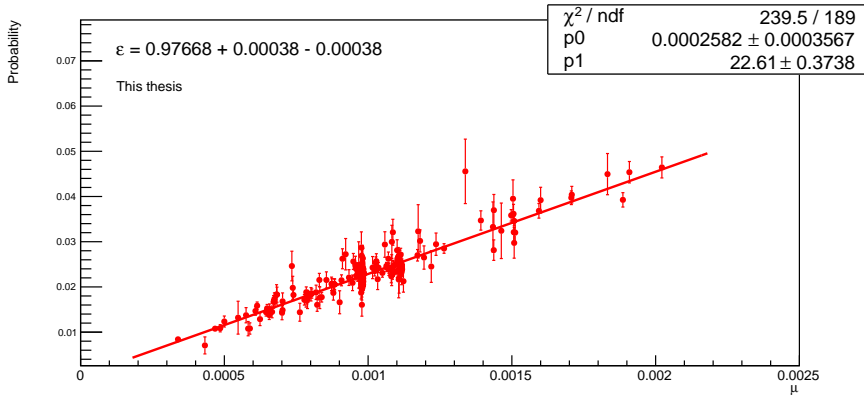
$$\frac{d\sigma_{\text{J}/\psi}^{\text{coh}}(\text{ZDC class})}{dy} = \frac{F_{\text{ZDC class}} \cdot N_{\text{J}/\psi}(\text{ZDC class})}{(1 + f_1 + f_D)(\epsilon_{\text{J}/\psi}) \text{BR}(\text{J}/\psi \rightarrow \mu\mu) \epsilon_{\text{veto}} L_{\text{int}} \Delta y}, \quad (7.7)$$

where  $F_{\text{ZDC class}}$  is the correction factor in referring ZDC class (for classes (0n0n) and (0nXn) is  $F_{(0n0n), (0nXn)} = 1$ ),  $N_{\text{J}/\psi}(\text{ZDC class})$  is the number of  $\text{J}/\psi$  events extracted from the invariant mass fit in each ZDC class,  $(1 + f_1 + f_D)$  corrects for incoherent and feed-down contribution in the sample computed in Sec. 6.7 and 6.6,  $\epsilon_{\text{J}/\psi} = 0.1176$  is the acceptance and efficiency of the detector,  $\epsilon_{\text{veto}} = 97.7\%$  is the V0A veto inefficiency determined with unbiased CTRUE events in section 7.1,  $L_{\text{int}} = 532 \mu\text{b}^{-1} \pm 5\%$  the integrated luminosity and  $\Delta y$  is the size of the rapidity interval. The branching ratio  $\text{BR}(\text{J}/\psi \rightarrow \mu\mu) = 0.05961$  is taken from the Particle Data Group [28].

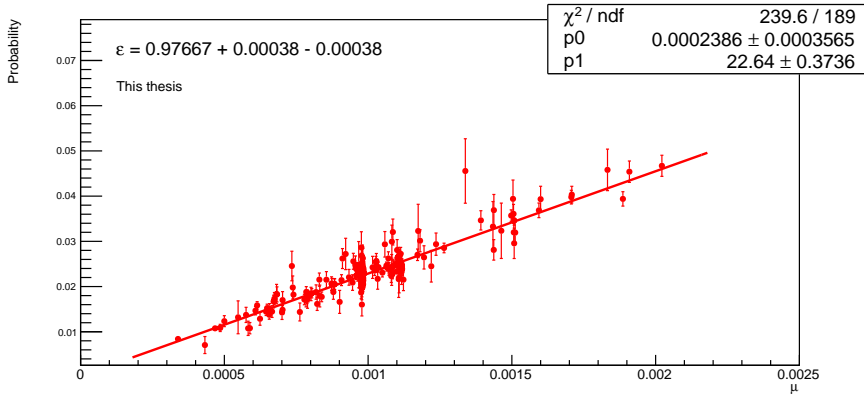
The systematic error includes uncertainties of the correction factor, luminosity normalization,  $f_D$  factor and  $f_1$  systematic uncertainty which was taken to be a difference of obtained values by me and values computed by Ing. Tomáš Herman, who has worked on the  $p_T$  fits in depth recently. One can notice, that systematic error for (0nXn) class is huge and it is so due to large difference in  $f_1$  parameter. The cross section computed for all events is in agreement with the value published in paper [3] within an error.

| ZDC class | $N_{J/\psi}$    | $F$   | $f_1$             | $d\sigma_{J/\psi}^{\text{coh}}/dy(\mu\text{b})$ |
|-----------|-----------------|-------|-------------------|---|
| All       | $16771 \pm 166$ | 1.015 | $0.063 \pm 0.001$ | $2785 \pm 28$ stat. $\pm 144$ syst.             |
| (0n0n)    | $12172 \pm 143$ | -     | $0.008 \pm 0.001$ | $2095 \pm 25 \pm 108$                           |
| (0nXn)    | $1812 \pm 52$   | -     | $1.407 \pm 0.149$ | $135 \pm 4 \pm 112$                             |
| (Xn0n)    | $1230 \pm 44$   | 1.061 | $0.041 \pm 0.006$ | $218 \pm 8^{+12}_{-13}$                         |
| (XnXn)    | $1016 \pm 38$   | 1.182 | $0.173 \pm 0.015$ | $179 \pm 7 \pm 16$                              |

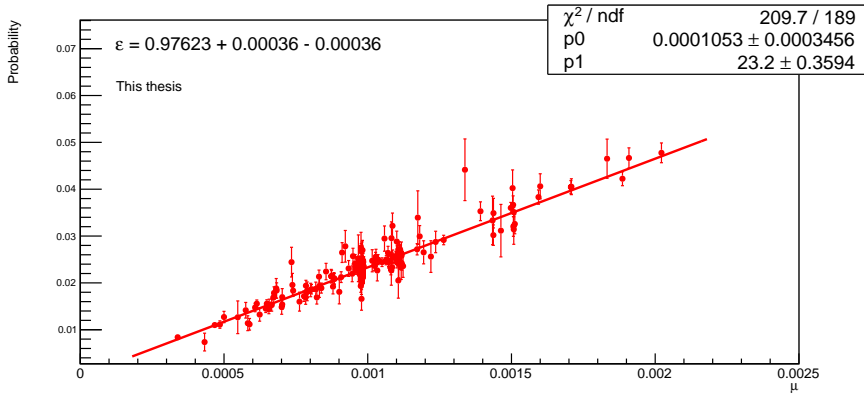
Table 7.3: Table of  $J/\psi$  yield, correction factors,  $f_1$  parameters and coherent  $J/\psi$  cross sections computed for different ZDC classes.



(a)  $\epsilon_{\text{PU}1}$  - No signal in ADA and ADC detector and no tracklets requirements on "empty detector".

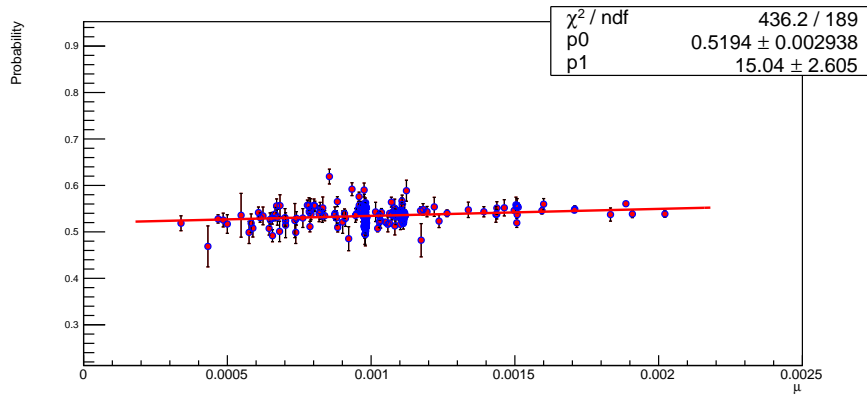


(b)  $\epsilon_{\text{PU}2}$  - The condition on no signal in ADA and ADC detectors is not considered.

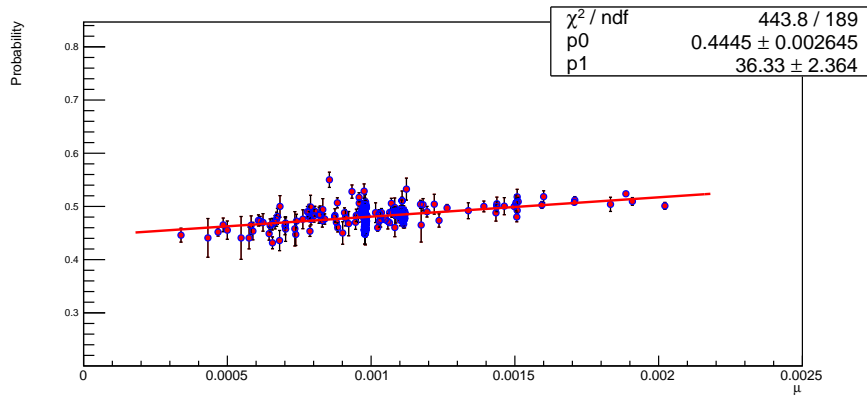


(c)  $\epsilon_{\text{PU}3}$  - The condition on no tracklets is not considered.

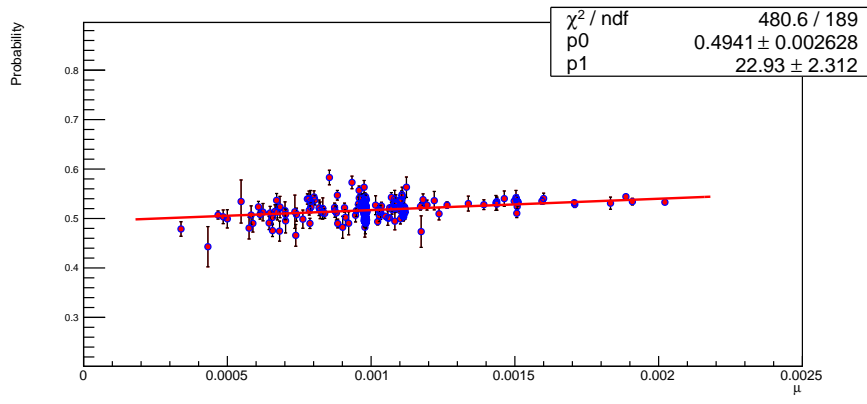
Figure 7.2: Pile-up determination using the CTRUE events for V0A detector.



(a)  $\varepsilon_1$  - No signal in ADA detector, no tracklets.

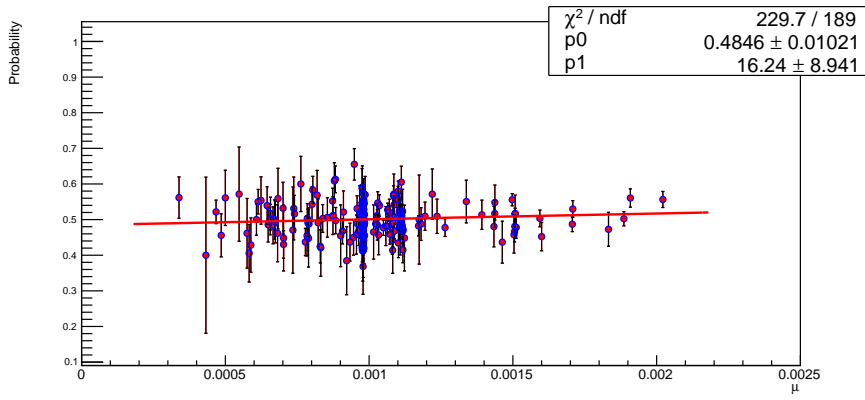


(b)  $\varepsilon_2$  - The condition on no signal in ADC detector is not considered.

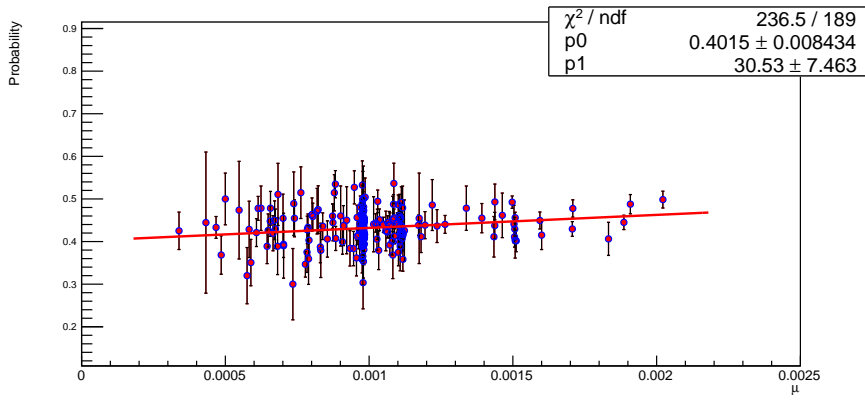


(c)  $\varepsilon_3$  - The condition on no tracklets is not considered.

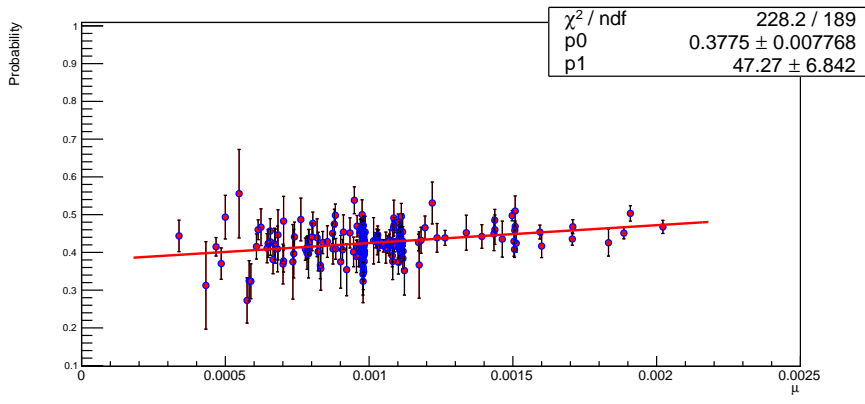
Figure 7.3: EMD events lost due to the V0A veto for (Xn0n) neutron class.



(a)  $\varepsilon_1$  - No signal in ADA, neither ADC detector, no tracklets.



(b)  $\varepsilon_2$  - The condition on no signal in ADA or ADC detector is not considered.



(c)  $\varepsilon_3$  - The condition on no tracklets is not considered.

Figure 7.4: EMD events lost due to the V0A veto for (XnXn) neutron class.

# Chapter 8

## Summary

The topic of interest is the investigation of low- $x$  gluon densities inside a nuclei. One possible way to study it is measuring of the cross section of exclusive  $J/\psi$  photoproduction in ultraperipheral collisions. This is so, because the cross section is sensitive to the gluon distribution function:  $\sigma \sim xG^2(x, Q)$ . In UPC either one nucleus can behave as a target or the emitter of photon, thus the low and high energy photons contribute to the cross section. The energy of photon directly corresponds with the  $x$  variable. Decoupling these two contributions could give us a tool to learn more about low- $x$  region. In an additional EMD process within one interaction of nuclei can neutrons and charged particles can be emitted. Measuring the cross section in different neutron classes is the way how to separate the contributions.

In this thesis the exclusive photoproduction and EMD was briefly described. The Muon Spectrometer and Zero Degree Calorimeter (ZDC), subdetectors of ALICE, were introduced. One chapter was devoted to new neutron generator program **n<sub>0</sub>n**. The recent published paper of  $J/\psi$  photoproduction was discussed and previous results of the cross section were presented.

In the analysis part the  $J/\psi$  candidates were selected from data sample of LHC18r and LHC18q periods using the CMUP6 trigger. The invariant mass was fitted with the Crystal Ball function and  $p_t$  distribution was shown with contributions from different processes using the MC data templates. The data sample was divided into four ZDC classes classified by neutron signal in ZDC calorimeters as follows: (0n0n) no neutrons in either side, (0nXn) and (Xn0n) at least one neutron detected in C and A side, respectively. And finally (XnXn) class, where more than one neutron was detected in both sides of ZDC. The energy deposit in ZNA and ZNC detector was presented with peaks of one or two neutrons detected clearly visible. The number of events was extracted from the invariant mass fits in each neutron class. The contributions from feed-down and incoherent  $J/\psi$  production were computed to clear the raw  $J/\psi$  yield from their contamination.

Used CMUP6 trigger has veto implemented with the V0A trigger. However, the V0A veto trigger is not hundred percent efficient. In this thesis I have presented the procedure of the V0A inefficiency calculation. To determine the inefficiency C1ZED triggered data was used. The computed results were  $\epsilon(Xn0n) = 48.6 + 3.6 - 4.4\%$  and  $\epsilon(XnXn) = 42.1 + 7.4 - 5.1\%$ . The values are consistent with the expectations.

Also a pile-up in V0A was determined, using unbiased data triggered per bunch crossing. The obtained value is  $\epsilon_{PU} = 97.65 + 0.05 - 0.07\%$ . The numbers represents the probability of having no pile-up effect, thus pile-up corresponds to  $(1 - \epsilon_{PU})$ . The

pile-up events were subtracted from the data sample.

The final correction factors for all data and for ZDC classes ( $Xn0n$ ), ( $XnXn$ ) were calculated to be  $F_{(all)} = 1.015^{+0.2\%}_{-0.2\%}$ ,  $F_{(Xn0n)} = 1.061^{+1.6\%}_{-2.2\%}$  and  $F_{(XnXn)} = 1.182^{+1.4\%}_{-1.6\%}$ , respectively.

Lastly, the  $J/\psi$  photoproduction cross section was computed for all ZDC classes. The measured cross section is in an agreement with published results within an error. Measured cross section in different ZDC classes still need some correction, such as ZDC migration but the first steps to be able to disentangle high and low photon energy contributions in the UPC cross section was done and the possibility of probing the gluon behavior in very low- $x$  region gets closer.

# Bibliography

- [1] **ALICE** Collaboration, B. Abelev et al., *Coherent J/ $\psi$  photoproduction in ultra-peripheral Pb-Pb collisions at  $\sqrt{s_{NN}} = 2.76$  TeV*, *Phys. Lett.* **B718** (2013) 1273–1283, [[arXiv:1209.3715](https://arxiv.org/abs/1209.3715)].
- [2] **CMS** Collaboration, V. Khachatryan et al., *Coherent J/ $\psi$  photoproduction in ultra-peripheral PbPb collisions at  $\sqrt{s_{NN}} = 2.76$  TeV with the CMS experiment*, *Phys. Lett.* **B772** (2017) 489–511, [[arXiv:1605.0696](https://arxiv.org/abs/1605.0696)].
- [3] **ALICE** Collaboration, S. Acharya et al., *Coherent J/ $\psi$  photoproduction at forward rapidity in ultra-peripheral Pb-Pb collisions at  $\sqrt{s_{NN}} = 5.02$  TeV*, [arXiv:1904.0627](https://arxiv.org/abs/1904.0627).
- [4] I. Pshenichnov, “Forward neutrons and protons from ultraperipheral Pb-Pb collisions: a quest of nuclear fragmentation at the LHC.” [https://indico.cern.ch/event/757761/contributions/3177980/attachments/1740154/2815527/I\\_Pshenichnov\\_PW\\_25\\_10\\_18.pdf](https://indico.cern.ch/event/757761/contributions/3177980/attachments/1740154/2815527/I_Pshenichnov_PW_25_10_18.pdf). Accessed: 2020-16-08.
- [5] J. G. Contreras, *Gluon shadowing at small x from coherent J/ $\psi$  photoproduction data at energies available at the CERN Large Hadron Collider*, *Phys. Rev.* **C96** (2017), no. 1 015203, [[arXiv:1610.0335](https://arxiv.org/abs/1610.0335)].
- [6] **ALICE** Collaboration, G. Martinez, *The Muon spectrometer of the ALICE experiment*, *Nucl. Phys.* **A749** (2005) 313–319, [[hep-ex/0410061](https://arxiv.org/abs/hep-ex/0410061)].
- [7] D. Stocco, *Development of the ALICE Muon Spectrometer: Preparation for data taking and heavy flavor measurement*. PhD thesis, Turin U., 2008.
- [8] R. Arnaldi, E. Chiavassa, C. Cicali, P. Cortese, A. Falco, G. Dellacasa, N. Marco, A. Ferretti, M. Gallio, P. Macciotta, A. Masoni, A. Musso, C. Oppedisano, A. Piccotti, G. Puddu, E. Scalas, E. Scomparin, S. Serci, E. Siddi, C. Soave, G. Usai, and E. Vercellin, *Performances of zero degree calorimeters for the ALICE experiment*, *Nuclear Instruments and Methods in Physics Research Section A: Accelerators, Spectrometers, Detectors and Associated Equipment* **456** (2001), no. 3 248 – 258.
- [9] **ALICE** Collaboration, E. Abbas et al., *Performance of the ALICE VZERO system*, *JINST* **8** (2013) P10016, [[arXiv:1306.3130](https://arxiv.org/abs/1306.3130)].
- [10] G. Herrera Corral, *Diffractive Physics with ALICE at the LHC: the control of quantum collisions*, *J. Phys. Conf. Ser.* **624** (2015), no. 1 012008.

- [11] M. Broz, J. G. Contreras, and J. D. Tapia Takaki, *A generator of forward neutrons for ultra-peripheral collisions:  $n_0^0 n$* , arXiv:1908.0826.
- [12] I. Pshenichnov, *Electromagnetic excitation and fragmentation of ultrarelativistic nuclei*, *Physics of Particles and Nuclei* **42** (03, 2011) 215–250.
- [13] The ALICE Collaboration and K Aamodt and A Abrahantes Quintana and R Achenbach and S Acounis and D Adamová, *The ALICE experiment at the CERN LHC*, *Journal of Instrumentation* **3** (aug, 2008) S08002–S08002.
- [14] **H1, ZEUS** Collaboration, H. Abramowicz et al., *Combination of measurements of inclusive deep inelastic  $e^\pm p$  scattering cross sections and QCD analysis of HERA data*, *Eur. Phys. J. C* **75** (2015), no. 12 580, [arXiv:1506.0604].
- [15] J.-P. Blaizot, *High gluon densities in heavy ion collisions*, *Rept. Prog. Phys.* **80** (2017), no. 3 032301, [arXiv:1607.0444].
- [16] M. G. Ryskin, *Diffractive  $J/\psi$  electroproduction in LLA QCD*, *Z. Phys. C* **57** (1993) 89–92.
- [17] V. Fílová, “Coherent photoproduction of  $J/\Psi$  in Pb–Pb collisions with emission of forward neutrons.” [http://physics.fjfi.cvut.cz/publications/ejcf/VU\\_Vendulka\\_Filova.pdf](http://physics.fjfi.cvut.cz/publications/ejcf/VU_Vendulka_Filova.pdf), 2019. Accessed: 2020-15-08.
- [18] A. J. Baltz, *The Physics of Ultraperipheral Collisions at the LHC*, *Phys. Rept.* **458** (2008) 1–171, [arXiv:0706.3356].
- [19] J. G. Contreras and J. D. Tapia Takaki, *Ultra-peripheral heavy-ion collisions at the lhc*, *International Journal of Modern Physics A* **30** (2015), no. 08 1542012, [<https://doi.org/10.1142/S0217751X15420129>].
- [20] I. Pshenichnov, “On forward protons emitted in PbPb collisions at the LHC.” [https://indico.cern.ch/event/564466/contributions/2302384/attachments/1335577/2325036/Pshenichnov\\_UPC\\_20\\_Sept\\_16.pdf](https://indico.cern.ch/event/564466/contributions/2302384/attachments/1335577/2325036/Pshenichnov_UPC_20_Sept_16.pdf). Accessed: 2020-16-11.
- [21] V. Guzey, E. Kryshen, and M. Zhalov, *Coherent photoproduction of vector mesons in ultraperipheral heavy ion collisions: Update for run 2 at the CERN Large Hadron Collider*, *Phys. Rev. C* **93** (2016), no. 5 055206, [arXiv:1602.0145].
- [22] V. Guzey and M. Zhalov, *Exclusive  $J/\psi$  production in ultraperipheral collisions at the LHC: constrains on the gluon distributions in the proton and nuclei*, *JHEP* **10** (2013) 207, [arXiv:1307.4526].
- [23] V. Fílová, “Coherent production  $J/\Psi \rightarrow p\bar{p}$  in Pb–Pb ultra-peripheral collisions.” [http://physics.fjfi.cvut.cz/publications/ejcf/bp\\_ejcf\\_16\\_filova.pdf](http://physics.fjfi.cvut.cz/publications/ejcf/bp_ejcf_16_filova.pdf), 2016. Accessed: 2020-16-08.
- [24] **ALICE** Collaboration, P. Cortese et al., *ALICE technical design report on forward detectors: FMD, T0 and V0*.

- [25] M. Broz, J. C. C. Noris, E. C. Villar, C. D. Galvan, E. Endress, L. G. E. Beltran, A. F. Tellez, D. Finogeev, A. M. Gago, G. H. Corral, T. Kim, A. Kurepin, A. B. Kurepin, N. Kurepin, I. L. Monzon, M. I. M. Hernandez, C. Mayer, M. M. Mieskolainen, R. Orava, L. A. P. Moreno, J. P. Revol, M. R. Cahuantzi, S. R. Torres, D. Serebryakov, A. Shabanov, E. Usenko, and A. V. Tello, *Performance of alice ad modules in the cern ps test beam*, 2020.
- [26] E. Abbas, B. Abelev, J. Adam, D. Adamov, A. M. Adare, M. M. Aggarwal, G. Aglieri Rinella, M. Agnello, A. G. Agocs, and et al., *Charmonium and  $e + e$  pair photoproduction at mid-rapidity in ultra-peripheral pbpb collisions at  $\sqrt{s_{NN}} = 2.76 \text{ TeV}$* , *The European Physical Journal C* **73** (Nov, 2013).
- [27] T. A. Collaboration, *Performance of the alice experiment at the cern lhc*, *International Journal of Modern Physics A* **29** (2014), no. 24 1430044, [<https://doi.org/10.1142/S0217751X14300440>].
- [28] P. D. Group, <https://pdg.lbl.gov/2018/listings/rpp2018-list-J-psi-1S.pdf>. Accessed: 2021-10-01.
- [29] F. J. analysis in ZDC classes. <https://indico.cern.ch/event/911924/contributions/4177488/attachments/2169881/3663287/JPsi%20analysis.pdf>. Accessed: 2021-15-01.